Use of Dynamic Contrast Enhanced Magnetic Resonance Imaging (DCE-MRI) on Head and Neck Cancer

LEE, Kar Ho Francis

A Thesis Submitted in Partial Fulfilment

of the Requirements for the Degree of

Doctor of Philosophy

in

Medical Imaging

The Chinese University of Hong Kong

August 2011

ProQuest LLC.
789 East Eisenhower Parkway
P.O. Box 1346
Ann Arbor, MI 48106 - 1346

ABSTRACT

Abstract of thesis entitled: Use of Dynamic Contrast Enhanced Magnetic Resonance Imaging (DCE-MRI) on Head and Neck Cancer

Submitted by LEE Kar ho, Francis for the Doctoral Degree of Philosophy in Medical Imaging at The Chinese University of Hong Kong in May 2011

INTRODUCTION

Dynamic contrast enhanced magnetic resonance imaging (DCE-MRI) uses fast imaging to capture the dynamics of image enhancement after the injection of a contrast agent. With appropriate analysis methods, useful information can be extracted to reflect the micro-vascular structure of body tissues. Physiological information provided by DCE-MRI has already shown potential for use in cancer management for tumor characterization, assessment of treatment response and evaluation of treatment induced complications. However, this technique is difficult to perform in the head and neck and there is insufficient evidence to support its widespread clinical use at this time. The aim of the thesis is to firstly evaluate technical issues influencing DCE-MRI and secondly use the optimized technique in pilot clinical studies in patients with head and neck cancer.

METHOD

The technical issues examined in the thesis were related to flip angle acquisition, optimization of the pharmacokinetic model and measurement of arterial input function (AIF). The pilot clinical studies in head and neck cancer patients examined in the thesis were related to the differentiation of different types of head and neck cancers, early prediction of tumor therapy local control, and assessment of radiation injury to the salivary glands.

RESULTS

Technical evaluation of DCE-MRI:

(1) With nominal T1 values and contrast influx for head and neck lesions, flip angle of 10 – 20 degrees was found to induce maximum image enhancement and robustness of signal.

(2) The original Tofts model was modified in this thesis to include the mathematical term for contribution from the plasma volume v_p and the rationale were supported by simulation data in the thesis. With typical contrast enhancement in head and neck lesions, error of up to 53% for k_{trans} and 17% for v_e may result if the plasma contribution was ignored.

(3) AIF extracted from the left and right carotid arteries were compared in 21 head and neck cancer patients. Results showed no significant difference between the AIF

extracted from either side. DCE-MRI parameters obtained from repeated scans in individual patients were more reproducible when the AIF was measured individually instead of using a population-based AIF.

Clinical pilot studies:

(1) DCE-MRI on cancers in 63 patients were examined with histogram analysis. k_{trans}, area under the curve (AUC60 and AUC90) showed significant differences between undifferentiated carcinoma (UD)/squamous cell carcinoma (SCC) and UD/lymphoma. The mean AUC90 demonstrated the highest accuracy of 78% for distinguishing UD/SCC, and the 75% percentile AUC90 provided the highest accuracy of 97% for distinguishing UD/lymphoma.

(2) DCE-MRI was conducted in 17 patients with SCC before and at 2 weeks after start of therapy. Changes in the 25% percentile and the mean k_{trans} after two weeks of treatment showed a significant correlation with local failure.

(3) Irradiated parotid glands of 20 patients with nasopharyngeal carcinoma were scanned with the DCE-MRI protocol before and after completion of radiotherapy. Baseline v_e, v_p and the post-treatment rise in v_e correlated significantly with parotid gland atrophy.

CONCLUSIONS

The results of this thesis showed that DCE-MRI is a feasible technique to perform in the head and neck and results from pilot clinical studies showed a potential role for DCE-MRI in tumour characterization, predication of cancer treatment response and radiation injury.

摘要

引言

動態對比增強磁共振（DCE-MRI）是一種功能成像的技術。這技術可以在對人體注射顯影劑後，利用快速成像的方法獲取圖像訊號強度的變化。透過適當的分析工具，DCE-MRI 能提供關於血管結構的有用資料。DCE-MRI 所提供的資料，已被證實在腫瘤診治上的功用。它在腫瘤特徵描述、治療效果及治療引起的副作用評估上，都有一定的作用。但是，DCE-MRI 在頭頸部的應用上有一定的技術困難。現時的經驗及證據仍未足以支持 DCE-MRI 在頭頸癌上作廣泛的應用。這份論文的目的就是首先研究 DCE-MRI 的技術問題。其優化後的技術則用於數個頭頸癌的臨床試驗上。

方法

這份論文所研究的技術問題包括射頻激發偏折角的選擇，藥物動力模型的優化及動脈輸入函數（AIF）的拮取。另外，這論文亦包括了三個 DCE-MRI 用於頭頸癌的臨床試驗：包括 DCE-MRI 用於不同種類頭頸癌的區分，DCE-MRI 用於腫瘤局部控制的早期預測，及 DCE-MRI 用於放療對腮腺影響的評估。

結果

對 DCE-MRI 技術的研究：

(1) 對於一般頭頸部腫瘤的 T1 值及顯影劑流入量，利用 10-20 度的射頻激發偏折角可產生最高的訊號強度變化及最好的訊號穩固度。

(2) 這份論文所用的 Tofts 藥物動態模型，加入了計算血漿容積 v_p 的項數。論文內的模擬數據顯示，在一般的頭頸腫瘤，若 v_p 不被計算在內，DCE-MRI 參數 k_{trans} 將可有高達 53% 的估算誤差，v_e 將可有高達 17% 的誤差。

(3) 論文中比較了 21 個頭頸癌病人中，由其左邊及右邊頸動脈拮取的 AIF。結果顯示兩邊拮取的 AIF 沒有明顯的差別。而每次成像拮取 AIF，比起利用群體平均 AIF 所得的 DCE-MRI 參數具有更高的重現性。

臨床試驗：

(1) 利用直方圖分析，DCE-MRI 用於 63 個頭頸癌的病人上。未分化癌與鱗狀上皮細胞癌，及未分化癌與淋巴癌的 k_{trans}、首 60 秒及 90 秒的曲線下面積（AUC60, AUC90）均顯示明顯的分別。平均 AUC90 在區分未分化癌與鱗狀上皮細胞癌顯示最高的精確度 (78%)。而 75%百分位數 AUC90 在區分未分化癌與淋巴癌則顯示最高的精確度 (97%)。

(2) 利用 DCE-MRI 技術於 17 個頭頸癌病人上，在病人接受治療前及治療開始後兩星期進行素描。結果顯示 25%百分位數及平均 k_{trans} 於兩次素描的變化，在局部控制有效與無效的病人之間有明顯的分別。

(3) 利用 DCE-MRI 對 20 個鼻咽癌的腮腺，在放療前及放療完成後進行素描。結果顯示放療前 v_e, v_p 及放療完成後 v_e 的增加均與腮腺萎縮有明顯的關係。

結論

論文結果顯示 DCE-MRI 用於頭頸癌的可行性。初步的臨床試驗顯示 DCE-MRI 於頭頸癌腫瘤特徵描述、治療效果及治療引起的副作用評估上有潛在的效用。

ACKNOWLEDGEMENTS

I wish to thank my supervisor: Dr. A.D. King and Dr. D.K.W. Yeung of their guidance, encouragement and advice throughout this entire project. Without their continuous support, this work would not have been possible.

My thanks also go to Dr. D.L. Buckley from the University of Manchester for his advice in the analysis of the data; Dr. B.B.Y. Ma and Dr. M.K.M. Kam from the Department of Clinical Oncology of the Chinese University of Hong Kong for their participation, support and assistance in the projects.

I also want to thank the staff members of the Department of Imaging and Interventional Radiology in the Chinese University of Hong Kong for all their assistance in this work.

This work was supported by departmental funding from the Department of Imaging and Interventional Radiology in the Chinese University of Hong Kong.

Above all, I am indebted to my family for their unfailing support, understanding and encouragement; to them this work is gratefully dedicated.

List of Tables

List of Figures

List of Abbreviations

AIF	Arterial input function
AUC	Area under curve
DCE-MRI	Dynamic contrast enhanced magnetic resonance imaging
DWI	Diffusion weighted imaging
EES	Extravascular extracellular space
F	Blood flow
FOV	Field of view
Gd	Gadolinium
Hct	Haematocrit proportion
HNSCC	Head and neck squamous cell carcinomas
IDL	Interactive data language
LC	Local control
LF	Local failure
LT-AIF	Left arterial input function
MRI	Magnetic resonance imaging
MRS	Magnetic resonance spectroscopy
NCI	National Cancer Institute
NFD	Nephrogenic fibrosing dermopathy
NMR	Nuclear magnetic resonance
NSA	Number of acquisitions
NSF	Nephrogenic systemic fibrosis
PS	Permeability surface area product
ROC	Receiver Operator Characteristics
ROI	Region of Interest
RT-AIF	Right arterial input function
SNR	Signal to noise ratio
TE	Echo time
TR	Repetition time
USPIO	Ultra small particulate iron oxide
VEGF	Vascular endothelial growth factor

CONTENTS

Chapter 1 — Introduction to the Use of Dynamic Contrast Enhanced Magnetic Resonance Imaging (DCE-MRI) in Head and Neck Cancer

1.1 Introduction

Magnetic resonance imaging (MRI) is a non-invasive and non-ionizing medical imaging modality. It provides three-dimensional images of the human body with excellent image contrast for soft tissues and bones. MRI is capable of acquiring images with different image contrast by adjusting the repetition time (TR) and echo time (TE) in the pulse sequence. Different pulse sequences may also be devised to generate images with different temporal and spatial resolution, by means of adjusting parameters such as the order and timing of gradients, radiofrequency excitation pulses and data acquisition. MRI is thus a highly flexible imaging modality and offers a wide spectrum of image information.

Conventional MRI offers morphological information on the patient's anatomy, and is the basis of clinical MRI examinations. The development of functional MRI has provided another potential area of MRI usage. Functional MRI is a special type of MR acquisition technique that, with appropriate analysis methodology, can extract information pertaining to physiological or biological activities in human or animals. Magnetic Resonance Spectroscopy (MRS), Diffusion-Weighted Imaging (DWI) and

Dynamic Contrast Enhanced (DCE-MRI) imaging are examples of functional MRI. With the advent of new MRI technologies, such as fast acquisition sequences and phase array coils, images of adequate quality can be acquired at a larger volume and at a faster speed. These will benefit dynamic functional MR imaging which needs high spatial and temporal resolution. New technologies have increased the potential clinical application of functional MRI.

Dynamic Contrast Enhanced MRI (DCE-MRI) is the study of the dynamics of contrast agent after it has been injected into the human body. In general, contrast agent enhances MR image intensity, and the level of enhancement is higher in tissues with accumulated concentration of contrast agent. Tissues with high vessel density, permeability and leakage space usually demonstrate a rapid and high level of enhancement. These can be shown by images acquired with high spatial and temporal resolution before, during and after contrast injection. With appropriate DCE-MRI analysis, information can be generated from these images to reflect vascular and cellular structure of the tissue.

One major application of DCE-MRI is in oncology. Tumor growth is known to be associated with increase in the number of blood vessels and a change in vessel structure (Carmeliet and Jain, 2000). The degree of change in the vascular properties may indicate tumor aggressiveness, and this may have clinical implications. DCE-MRI has shown potential in tumor characterization, treatment outcome

prediction and treatment response monitoring. Studies on therapeutic anti-angiogenic drugs may also use DCE-MRI as a tool to monitor treatment efficacy.

Studies with different clinical applications have been published on the use of DCE-MRI in different types of cancer, especially in the breast (Turnbull, 2009; Tuncbilek N., Tokatli F Altaner S, et al., 2011; Loiselle C.R., Eby P.R., Peacock S., et al., 2011) and prostate (Franiel T., Hamm B., Hricak H., 2011; Isebaert S., De Keyzer F., Haustermans K., et al., 2011; Bonekamp and Macura, 2008). Comparatively, DCE-MRI of head and neck cancers was less extensively examined. The DCE-MRI technique itself is also undergoing a process of migration towards quantitative analysis and pharmacokinetic modeling to replace qualitative assessment of images or enhancement curves. Therefore, a substantial amount of work is necessary to realize the DCE-MRI for head and neck cancer. Technical issues related to the processing and analysis of DCE-MRI, which may be unique for the application in the head and neck region, have to be addressed. The ultimate objective is to establish a standardized and practical protocol which is simple and reliable to implement. The protocol can then be used to generate reliable data to support a wider clinical use of the emerging technique.

In this thesis, a number of major technical issues on DCE-MRI in head and neck cancers are identified, and results of studies on these issues are presented. Important aspects examined include: (1) the optimization of acquisition protocol, with emphasis

on the choice of flip angles in the spoiled gradient echo sequences for data acquisition during contrast enhancement, the effect of signal-to-noise ratio and acquisition duration on the estimation of DCE-MRI parameters; (2) the effect of arterial input function (AIF) on the analysis outcome; (3) the use of different analysis techniques, which is comprised of area under concentration curve (AUC), pharmacokinetic models proposed by Tofts and Kermode (1991), and by Brix (1991); and the reproducibility of these DCE-MRI parameters.

Results from the abovementioned issues were applied to devise an optimal DCE-MRI technique in the head and neck region. The optimized DCE-MRI technique was then implemented to study the usefulness of DCE-MRI in: (1) characterization of head and neck cancers; (2) early prediction of tumor therapy local control and (3) assessment of radiation complications in the parotid glands.

1.2 Physics and Development of MRI

The clinical application of MRI began in the 1970's. However, the scientific foundation was established well before this. Early in the century, Sir Joseph Larmour discovered the relationship between angular frequency of atom precession and magnetic field strength. Furthermore, it was shown that the energy of the rotating atom could be increased through resonant absorption of radio waves at the same frequency. In this way, atoms could be excited to a higher energy level. After

excitation, the atomic nuclei returned to the original energy level by the process of relaxation, and radio waves at the precession frequency were emitted. In 1946, Felix Bloch and Edward Mills Purcell exploited this phenomenon, and developed instruments to measure the emitted radio waves for detection of magnetic resonance in liquids and solids (Bloch, Hansen and Packard, 1946; Purcell, 1946). This laid the foundation of nuclear magnetic resonance (NMR) spectroscopy, which has proven its usefulness in the area of chemistry and physics until now. For such invention, they shared the Nobel Prize in physics in 1952.

In 1971, Raymond Damadian showed that nuclear magnetic relaxation times of protons in tissues and tumors were different (Damadian, 1971). Protons are abundant in human body since water and fat contribute a large proportion of body volume. This initiated the study of magnetic resonance on cancer disease. In 1973, Paul Lauterbur designed a new imaging technique that utilized magnetic gradients to produce a two-dimensional image by back-projection. The technique was based on the Larmour precession principle that the frequency of the proton, and thus the emitted radio waves after proton excitation, was proportional to the magnetic field. The magnetic field varied at different physical location due to the presence of the magnetic gradient. Radio waves emitted by excited protons were collected by receiving coils. By frequency spectrum analysis, the origin of the radio waves could be determined, and thus generated an image that represented the density of atomic

nuclei in the anatomy. Sir Peter Mansfield further developed the gradient system and the mathematical analysis of the received radio signals to improve the imaging technique. Paul Lauterbur and Sir Peter Mansfield were awarded the 2003 Nobel Prize in Medicine. Their work formed the basis of clinical MRI nowadays.

1.3 Physics and Development of DCE-MRI

With the advancement of MRI technologies, three-dimensional MR images could be acquired in seconds with acceptable spatial resolution. This was achieved by the invention of phase array coil that increased acquisition speed, and also fast imaging pulse sequences such as spoiled gradient echo, echo planar imaging, etc. MRI with high temporal resolution has provided the right conditions for dynamic image acquisition. Dynamic acquisition in resolution of seconds enabled examination of fast changes by the use of MRI. The examination of the dynamic distribution of contrast agent was one application which has been realized and attracted increasing academic and clinical interest.

The development of DCE-MRI was stemmed from the wide spread clinical use of MRI contrast agent to enhance image contrast. Gadolinium-based agent is the most commonly used, and has been widely employed in clinical practice for over 20 years. Gadolinium ions (Gd3+) are formed into molecule complexes after attachment to other ligands. Complexes of gadolinium ion are paramagnetic and cause

shortening in proton relaxation times after intravenous injection into the human body, thus causing the enhancement in images. There are a number of attributes of Gadolinium contrast agents that made them safe and practical for use: they are stable in aqueous solution at physiological pH such that no free Gd3+ ions are present; they are manufactured to bear at least one free site for coordination of water molecules, and fast exchange of water molecules enable relaxation of extensive number of protons in the vicinity of the contrast molecule; chelation is conducted during the production process to detoxify the agent. The contrast agent used in this thesis, called Gd-DOTA (gadolinium 1,4,7,10-tetraazacyclododecane-1,4,7,10-tetraacetic acid), is a simple ligand and is relatively small in size (~500 Da). The agent crosses the endothelial walls of blood vessels, especially the leaky vessels of tumor.

The action of the contrast agent is manifested by water proton T1 and T2 shortening. In general, due to the fast inflow and accumulation of contrast agent in tumor, affected tissues show a faster and higher image intensity enhancement than most normal tissues in T1-weighted images, while a reduction of signal is shown in T2-weighted images. The latter is caused by susceptibility-based T2 shortening effect of the contrast agent. With this effect, the contrast molecule alters the local magnetic environment in its vicinity, and causes additional signal dephasing in nearby protons. Susceptibility-based effect is relatively long ranged and may extend for a few millimeters depending on the sensitivity of the acquisition sequence. T2-weighted

imaging is usually used to study cerebral blood volume: contrast agent confined in blood vessels due to blood brain barrier induces a substantial and observable signal reduction which could be used to deduce blood volume.

The relaxivity-based effect by T1 shortening of contrast agent results in image enhancement in T1-weighted images. The effect is short ranged and affects only protons in the immediate vicinity of the contrast agent. The induced signal change is therefore more localized, and areas of high contrast con tration could be identified with better spatial resolution. The magnitude of enhancement is much more pronounced than that induced by T2 shortening effect when there is leakage of contrast agent into extravascular extracellular space (EES). T1-weighted DCE-MRI is thus more widely used in cancer imaging, where the presence of high vessel density and extravascular leakage of contrast agent in malignant tissues give a substantial image enhancement at regions of the tumor. T1-weighted and T2-weighted DCE-MRI require different acquisition and processing techniques, and their analysis outcome bear different physiological implications. Studies in this thesis were focused on the T1-weighted DCE-MRI method for head and neck cancers.

Cancer development is closely related to its vascular blood supply. In the early stage of cancer, malignant lesions are usually avascular. Oxygen and nutrition necessary for the growth of the tumor is supplied by diffusion. As the tumor grows bigger in size, typically above 200 μm in diameter, oxygen and nutrients supplied by

diffusion is no longer adequate to meet the demand of the tumor. Neovasculature is required in the tumor by extended growth from existing vessels. This process of new vessel development is induced by the release of angiogenic factor, namely the vascular endothelial growth factor (VEGF), by tumor cells. These tumor capillaries are usually highly heterogeneous in morphology, and extremely coarse in structure. These vessels are also irregularly constricted, dilated and distorted with twisting and sharp bends, which causes them to be leaky. Aggressive tumors such as glioblastoma tend to bear leaky and irregular vessels, and vessels in slow growing benign tumors tend to be more regular. Also, cells in tumors are usually irregularly arranged and thus less compact than that of normal tissues, which then leads to a larger EES. Both of these properties in tumor tissues allow a more rapid and larger influx of contrast agent into tumors after contrast injection, and also a faster outflux of contrast at the washout phase. These are manifested in the contrast enhancement profiles. With appropriate analysis, DCE-MRI can provide information pertaining to the vascular and cellular properties of tumor, which could infer tumor characteristics and be useful clinically.

The analysis of DCE-MRI has evolved. At present, a variety of analysis methods are available, ranging from simple qualitative assessment of DCE-MRI images or pattern of enhancement, to elaborate compartmental models with transfer constants between compartments to represent the dynamics of contrast agents. Most early

DCE-MRI studies adopted the qualitative approach. For example, contrast enhancement time curve pattern were analyzed to differentiate between malignant and benign tumors. With this approach, the demand on the processing software is minimal, and the capability to display the enhancement-time curves on pixels or within the region of interest (ROI) is sufficient for the analysis. The advantages of this method are the simplicity and robustness. Yet it is not quantitative and may be subjective in interpretation. Accuracy of such methods is thus expected to be limited.

A semi-quantitative method to yield parameters that described the shape of contrast enhancement curve has also been employed in a number of studies. Time to peak, enhancement slope, signal enhancement ratio and washout rate are the parameters generated from the analysis. Semi-quantitative method is more objective, and it is relatively simple to implement. However, these parameters may be susceptible to differences in scanner configurations, calibration, signal gain, T1 of tissues, etc. Therefore the method may not always provide reproducible results when the same subject is scanned with different scanners or at different times. Inter-subject and inter-center comparisons are thus more difficult. Moreover, the generated parameters bear no biophysical meaning. A better way to perform quantitative assessment is to deduce the contrast concentration from the signal intensity, and obtain the quantitative DCE-MRI parameters on the contrast concentration time curve. This will eliminate the difference between scanners and tissue T1 values, and

the area under concentration curve (AUC) becomes one of the popular DCE-MRI parameters. However, an accurate determination of T1 is necessary, and extra data must be acquired to achieve this.

In the 1990's, several research groups proposed pharmacokinetic models that described the dynamics of injected contrast agent in human tissues. These researchers proposed models with identified contrast-accessible compartments, and devised mathematical formulae to describe the rate of exchange between the compartments. From these models, contrast concentration curves obtained from patients could be fitted into the models and physiologically relevant parameters could be deduced to reflect the compartment size, transfer constant and the clearance rate of the contrast agent. Several major pharmacokinetic models for DCE-MRI were proposed by Tofts & Kermode (1991), Brix (1991) and St. Lawrence and Lee (1998). These models differed in the compartmental design, underlying assumptions and complexity, and there was increased interest to compare these models for DCE-MRI in oncology. Due to the complexity in the analysis and processing procedures, technical issues such as the extraction of arterial input function (AIF) and the optimal scan parameters are essential to optimize the technique. This is also one of the major areas of research pursued by many groups aimed at improving DCE-MRI in recent years.

Despite of the lack of a standardized analysis method, certain guidelines on the

use of DCE-MRI in cancer were proposed. The National Cancer Institute (NCI) of the United States has issued recommendations on the acquisitions for DCE-MRI image in oncology. The recommendations were based on the discussion in two consensus workshops, namely the 'Dynamic Contrast Enhanced Magnetic Resonance Imaging Workshop' in 1999 and the 'Future Technical Needs in Contrast Enhanced MRI of Cancer Workshop' in 2000. A number of recommendations were proposed on data acquisition and processing of DCE-MRI, with the aim of improving the reproducibility and reliability of the technique.

In 2005, the Pharmacodynamic/Pharmacokinetic Technologies Advisory Committee, Drug Development Office, Cancer Research in the United Kingdom made further suggestions on the processing of DCE-MRI, by inclusion of arterial input to cater for inter- and intra- patient differences due to cardiac dynamics (Leach, Brindle and Evelhoch, 2005).

1.4 Background of Head and Neck Cancer

Head and neck cancers originate from the upper aero-digestive tract, including the lip, oral cavity, nasal cavity, paranasal sinuses, pharynx, and larynx. About 90% of head and neck cancers are squamous cell carcinomas (HNSCC), which originates from the mucosal lining of these regions. According to the statistics from the Hong Kong cancer registry (2007), head and neck cancer accounted for about 12% of all

cancers in the territory. Mortality was about 15 per 100,000 populations. Head and neck cancers often spread to the lymph nodes of the neck, and this is a common manifestation of the disease at the time of diagnosis. Head and neck cancer is strongly associated with certain environmental and lifestyle risk factors, including tobacco smoking, alcohol consumption, occupational exposure, and certain strains of viruses. Head and neck cancers are usually aggressive in biological behavior (Ridge J.A., Glisson B.S., Lango M.N., et al., 2011).

Patients who present symptoms suspicious of a cancer in the head and neck region are usually referred to a doctor for a full medical history, physical exam, blood tests, endoscopy and direct clinical examination. Imaging then follows to further confirm the disease and to determine the extent of the tumor for disease staging. Biopsy is a more definite confirmation of the malignancy, and is usually done either by endoscopic biopsy or fine needle aspiration.

Head and neck cancer is highly curable if detected early. However, tumors presented at a late stage often have poor prognosis. Treatment methods include surgery, chemotherapy, radiation therapy or a combination of these. Strategy of disease management is decided upon the information available from radiological, clinical and pathological tests. An optimal strategy will result in good tumor control and survival, as well as reduced side effect. After treatment, follow up of patients at regular intervals ensures control of disease, and helps to devise further treatment

actions if the primary treatment does not resolve the disease completely. Follow up is usually conducted by physical examination, endoscopy or imaging. In HNSCC, the rate of tumor recurrence is about one-third, and an early prediction of recurrence or residual tumor will enable oncologists to devise alternative and more effective treatment to increase the treatment efficacy (Koch, Brennan, Zahurak, et al., 1996).

In this respect, DCE-MRI shares a role in head and neck cancer for detection, characterization of tumor, and early prediction of recurrent and residual tumor. The technique may also be useful in the evaluation of treatment side effect for nearby normal organs, which is usually affected during treatment due to the proximity of the organ to the tumor. New drugs acting against angiogenesis of tumor have also been introduced in the treatment of head and neck cancers. DCE-MRI may be useful in the evaluation of action path and efficacy of these drugs, although this is not the focus of this thesis. A number of technical issues were addressed to facilitate the use of DCE-MRI in head and neck cancers: optimization of acquisition parameters, selection of reliable arterial input function and evaluation of the analysis method.

1.5 Literature Search on Application of DCE-MRI

A literature review was conducted on the use of DCE-MRI on human studies of cancer. The keywords 'Dynamic contrast MRI' were used for searching in PUBMED. Only studies involving T1-weighted DCE-MRI on the study with human patient were

included, and a total of 542 publications were identified. As shown in Figure 1.1, a growing number of publications were released on the topic.

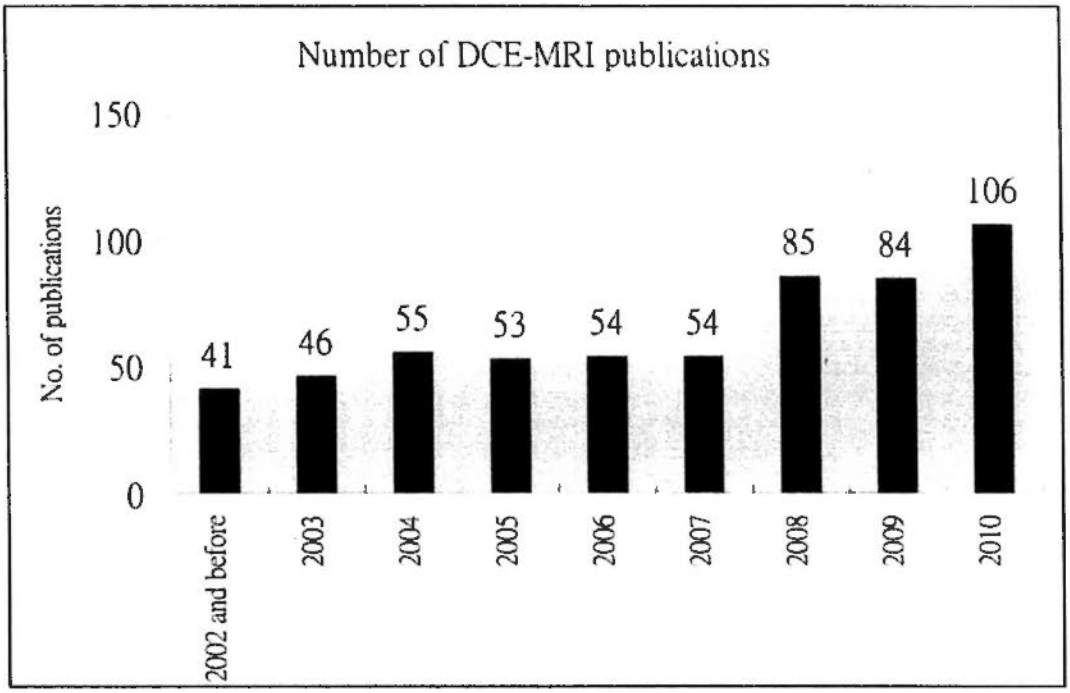

Figure 1.1: Number of DCE-MRI publications over the decade.

By classification according to disease sites, it is shown that the majority of the DCE-MRI publications were studies on breast and prostate cancers. Publications on these two disease sites accounted for almost half of the total number. Studies in the head and neck region also gained increased interest, but only contributed to less than 10% of the overall publications.

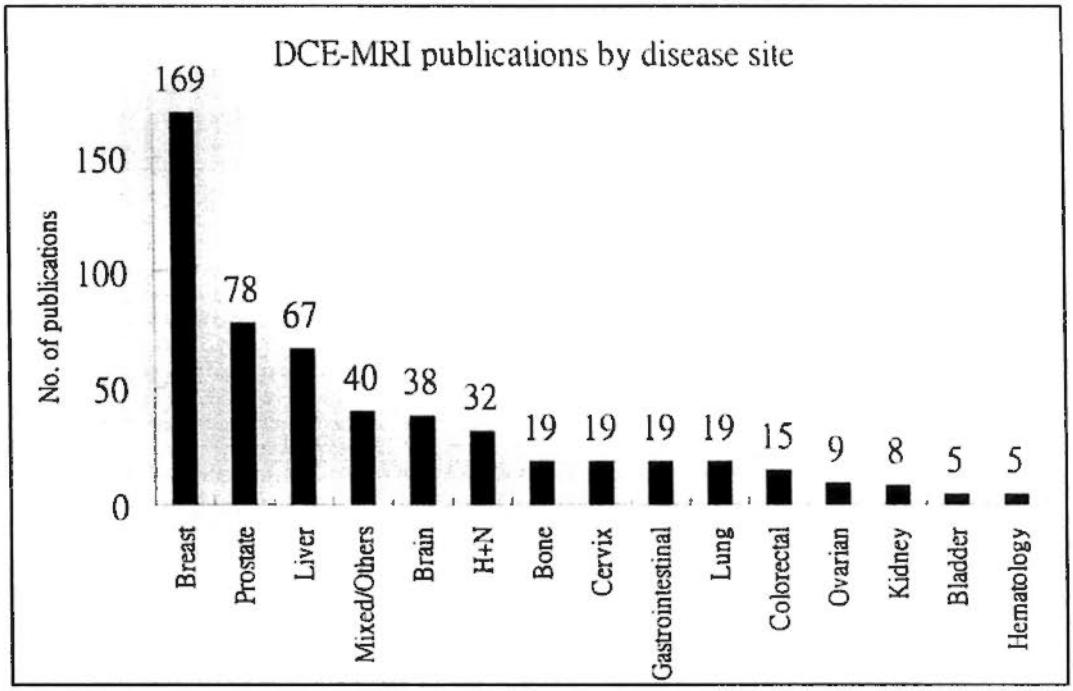

Figure 1.2: Number of publications according to disease sites.

Publications on DCE-MRI of the head and neck region have focused on tumor characterization (Jansen, Schöder, Lee, et al., 2010; Newbold, Castellano, Charles-Edwards, et al., 2009; Asaumi, Yanagi, Konouchi, et al., 2004; Asaumi, Yanagi, Hisatomi, et al., 2003; Chang, Li, Jerosch-Herold, et al., 2008; Fischbein, Noworolski, Henry, et al., 2003; Unetsubo, Konouchi, Yanagi, et al., 2009; Van Cann, Rijpkema, Heerschap, et al., 2008; Konouchi, Asaumi, Yanagi, et al., 2003; Yang, Wang, Xian, et al., 2009; Oberholzer, Pohlmann, Schreiber, et al., 2008; Hisatomi, Asaumi, Yanagi, et al., 2007; Tezelman, Giles, Tunca, et al., 2007; Asaumi, Hisatomi, Yanagi, et al., 2005), treatment response evaluation or prediction (Machiels, Henry, Zanetta, et al., 2010; Kim, Loevner, Quon, et al., 2010; Hoskin, Saunders, Goodchild, et al., 1999), technical issues (Shukla-Dave, Lee, Stambuk, et

al., 2009; Kim, Quon, Loevner, et al., 2007), evaluation of treatment complications (Juan, Chen, Jen, et al., 2009) and correlation with other functional imaging techniques (Bisdas, Seitz, Middendorp, et al., 2010; Bisdas, Baghi, Wagenblast, et al., 2009; Tunca, Giles, Salmasliogiu, et al., 2007). It is also noted that the more recent published studies on head and neck region used pharmacokinetic models, showing progressive acceptance of quantitative analysis method for DCE-MRI data.

1.6 Summary

DCE-MRI in head and neck is a challenging research area. Until now, there is very limited clinical evidence in support of DCE-MRI in the characterization, prediction of treatment response and assessment of treatment complications for cancers of this region. Technical issues have to be addressed to enable reliable DCE-MRI in this particular part of body. It is the objective of this thesis to provide further scientific and clinical evidence to facilitate its application.

Chapter 2 - Overview of DCE-MRI Processing and Technical Challenges

2.1 Introduction

This chapter provides an overview on the various technical aspects of DCE-MRI acquisition and processing. The types and properties of MR contrast agent, which forms the physical basis for image enhancement dynamics, is first discussed. The two pharmacokinetic models which were used in the studies of this thesis, and outline of the processing steps are described. Subsequent section then describes the international effort to standardize the DCE-MRI techniques. Finally the major technical challenges for the application of DCE-MRI in the head and neck region are discussed. This also summarizes the technical issues that will be addressed in the studies of this thesis.

2.2 Contrast Agents

Delineation of normal anatomy and lesions may sometimes be difficult in MR images from patients due to the limited intrinsic image contrast. MR contrast agents have been used to enable a better visualization of these structures. These agents are injected into the vein of the patient, and they are known to accumulate in regions of high vessel density. Generally, contrast agents alter the relaxation of nearby

molecules or local magnetic field homogeneity, and manifest their effect as changes in the signal intensity of images. Contrast agents can be classified according to their magnetic properties and biophysical distribution. The most commonly used agents, which are gadolinium(Gd)-based, are paramagnetic and enhance spin-lattice and spin-spin relaxation of molecules. Additionally, a high concentration of contrast agent, which usually occurs in highly vascular tissues, reduces local magnetic field homogeneity. Thus the presence of contrast agent shortens the T1, T2 and T2* of the nearby tissues. The effect can be visualized as positive enhancement in T1- or negative enhancement in T2- or T2*-weighted MR images. Gd-based contrast agents are available with a range of molecular sizes, and this determines the biophysical distribution of the agent: small-size agents can readily cross the endothelium and enters into the extravascular space, while large-size agents are confined to the blood pool.

Several other types of MR contrast agents were being developed, such as the Ultra Small Particulate Iron Oxide (USPIO). This agent causes T2* shortening and is readily taken up by macrophages. The agent is specific to lymphatic tissues and thus may be valuable in the identification of metastatic lymph nodes (Oghabian, Gharehaghaji, Amirmohseni, et al., 2010). Other agents such as micro-bubbles, manganese-based contrast agents, etc were investigated in an attempt to improve specificity and sensitivity of disease detection.

Despite the variety of contrast agents available in clinical or experimental setting, clinical safety is the common concern of these agents. Most contrast agents, including the popular Gd-based contrast agents, are toxic. A process called chelation is necessary during production to enable the formation of large stable organic complex around the gadolinium molecule. This reduces the toxicity that could result from direct exposure to gadolinium. Also, accumulation of such chemicals in the body is hazardous and agent molecules are eliminated from the body by excretion through the kidney. Therefore, patients with compromised kidney function are usually contraindicated for the agent. The Food and Drug Authority of the United States has issued information regarding the risk of Nephrogenic Systemic Fibrosis (NSF) or Nephrogenic Fibrosing Dermopathy (NFD) for patients who received Gd-based contrast agents (FDA Public Health Advisory 2006).

The contrast agent, gadolinium 1,4,7,10 – tetraazacyclododecane - 1,4,7,10 - tetraacetic acid, abbreviated as Gd-DOTA (Dotarem, Guerbet, Paris, France) used in the studies of this thesis is a common type of Gd-based MRI contrast agent. It has been validated to be safe in human, and has been released in Europe for human use since 1989.

Gd-DOTA is a small molecular size contrast agent (~500 Da). After intravenous injection into human, it induces short-ranged relaxivity effect due to dipole-dipole interaction between the large magnetic moment of paramagnetic ions in the contrast

agent and the tissue water protons. Assuming a fast exchange of water molecules in the extracellular and intracellular space, relaxation process in different water compartments within a single image voxel of human tissue can be described by a single T1 value. Therefore, presence of contrast agent in the vascular and extracellular compartment of human tissue simply shortens the tissue T1, and causes an enhancement in T1-weighted image intensity. The magnitude of enhancement is related to the concentration of contrast agent. The presence of contrast agent also shortens the T2 and T2*, which can be shown as negative enhancement in images. However, since relaxivity-based enhancement imaging is the focus of this thesis, such effect will be ignored in the T1-weighted images obtained in the studies.

The small Gd-DOTA molecules can cross the endothelium of the blood vessels and enters into the EES. However, it is blocked by blood brain barrier and cell wall of tissue cells.

2.3 Dynamic Contrast Enhanced (DCE)-MRI and Pharmacokinetic Models

Contrast agent in MRI enhances vascular lesions at the region of interest, and it has been widely used clinically for the detection of cancer. The process of enhancement, after appropriate analysis, yields further information related to the vascular structure of the tumor. In cancerous tissues, uncontrolled increase in microvascular density usually occurs due to excessive need of oxygen and nutrients

for tumor growth, and such process is called angiogenesis. Tumor growth depends heavily on vascular supply, the density and characteristics of these tumor vessels are different from that in normal tissues (Folkman, 1995). Rapid growing tumor blood vessels are structurally irregular and leaky. Therefore, contrast agents such as Gd-DOTA, diffuse rapidly through the endothelium into the EES. By inspecting the image enhancement-time curve, a significant difference in contrast agent dynamics can be shown as compared to normal tissues. Figure 2.1 shows typical enhancement time curves for lesions and normal muscular tissues. Theoretically, the dynamics of contrast agent can be mathematically analyzed by biophysical compartment models for quantitative DCE-MRI data analysis.

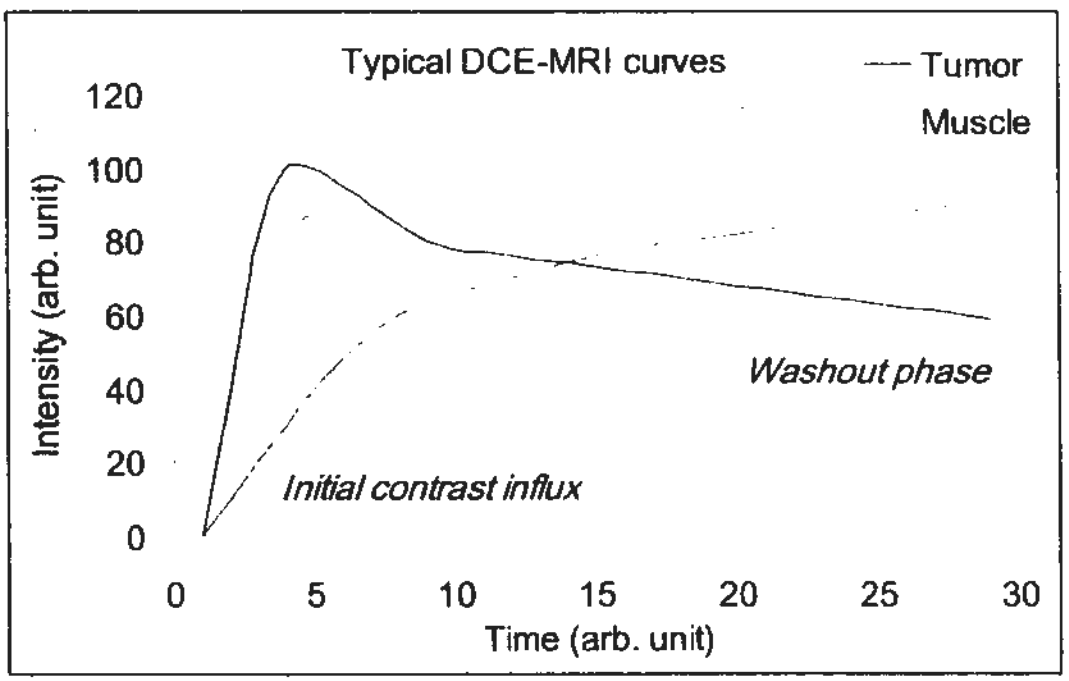

Figure 2.1: Typical contrast enhancement time curves for tumor and normal muscular tissue.

DCE-MRI generally yields information related to the blood volume, blood flow, endothelial permeability, vessel density and extravascular space of tumors. Cancer biology theories have suggested that increased tumor vessel permeability may reflect increased level of angiogenesis, and may also contribute to tumor cell spread in distant metastasis (Knopp, Weiss, Sinn, et al., 1999). On the other hand, cancer therapies such as radiotherapy and anti-angiogenic drugs induce damage of tumor vasculature, and this subsequently results in tumor cell death and shrinkage of tumor. In view of these, DCE-MRI provides early indication of tumor aggressiveness and therapy response. This may be a valuable adjunct to morphological images in the management of cancer.

Currently, the DCE-MRI analysis methods that are available are presented with varying degree of complexity. Qualitative analysis is the simplest method and involves visual inspection and classification of image enhancement pattern. Patterns of image enhancement curves can be classified for diagnostic purpose. An example of such method is an early study for differentiating the types of breast tumors: slow initial enhancement and wash-out represented benign lesions, and rapid initial enhancement and wash-out represented malignancies (Daniel, Yen, Glover, et al., 1998).

Semi-quantitative analysis has been developed to improve consistency and comparability of results. Simple parameters to describe the course of image

enhancement, such as enhancement slope, maximum enhancement, time to peak, wash out rate, etc are derived by simple measurements or curve fitting method. DCE-MRI studies have been conducted with this method of analysis, with positive results for characterization (Asaumi, Yanagi, Konouchi, et al., 2004) and prediction of treatment outcome for head and neck cancers (Hoskin, Saunders, Goodchild, et al., 1999). Despite these encouraging results, there are a number of shortcomings with this method. Firstly, the semi-quantitative parameters carry no biophysical meaning. Interpretation is thus empirical and the change in these parameters may not be easily explained or correlated with biological findings. Secondly, variations in the parameters due to scanner calibration, contrast injection rate and patient cardiac output are not catered for and this may contaminate the data and hinder inter-patient and inter-center comparability. A more elaborated and practical analysis method is needed.

In the 1990's, a number of pharmacokinetic models were proposed by researchers for the modeling of contrast dynamics in the tumors. These pharmacokinetic models hypothesized tissues as a number of compartmental spaces: the extracellular space, the vascular space and intracellular space. MRI contrast agents cannot enter intracellular space because of their size and inertness, a two compartment model, with the necessary transfer rate equations describing the diffusion of contrast agent between the compartments, serves to describe the

exchange dynamics. Buckley (2002) compared three commonly used DCE-MRI models: St. Lawrence and Lee's model (St Lawrence and Lee, 1998), Tofts and Kermode model (Tofts and Kermode, 1991; Tofts, Brix, Buckley, et al., 1999) and Brix model (Brix, Semmler, Port, et al., 1991) in terms of the processing outcome. The latter two models were chosen to be studied in this thesis because of model stability and practical acquisition time.

2.3.1 Area Under Curve

As shown in Figure 2.1, the contrast concentration time curves are distinctively different in tumors and in normal tissues. The rapid initial build up of contrast concentration in tumors results in substantially larger area under curve. The area under curve (AUC) at this initial period of contrast enhancement, which is usually chosen to be within about 100 seconds after contrast injection, has been employed clinically as a simple and robust DCE-MRI parameter (Evelhoch J., 1999). The parameters AUC60 and AUC90 used in this thesis are the area under curve for the lesion or the organ of interest at the initial 60 and 90 seconds. These are normalized by the AUC of the contrast concentration curve extracted from the artery supply. By doing this, the variations at different acquisitions, due to difference in cardiac output, injection timing, scanner receiver gain, etc, can be removed.

2.3.2 Tofts and Kermode Model

The two-compartment model represents the dynamic transfer of contrast agent between the compartments of plasma and the extracellular-extravascular space (EES). The model is graphically represented in Figure 2.2.

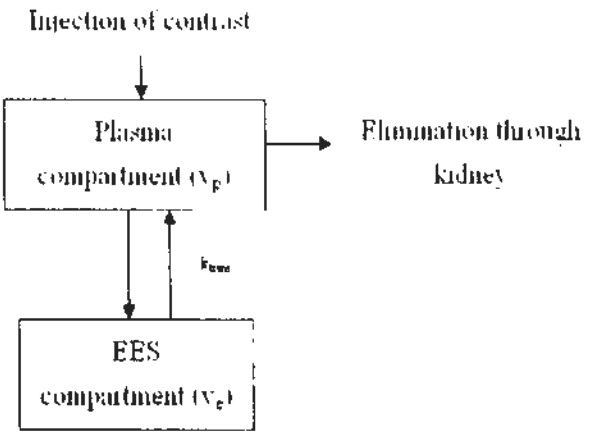

Figure 2.2: The compartmental model proposed by Tofts and Kermode.

The model expressions that describes the dynamic distribution of contrast agents are,

$$\frac{dC_e}{dt} = k_{trans}(C_e - C_p) \qquad [2.1]$$

$$C_t = C_e v_e + C_p v_p \qquad [2.2]$$

$$C_t(t) = K_{trans}\int_0^t C_p(t')e^{-\frac{K_{trans}(t-t')}{v_e}}dt' + v_p C_p(t) \qquad [2.3]$$

where C_t, C_e and C_p are the contrast concentration of the total volume of tissue, EES and plasma, respectively. The input of the system is given by the contrast concentration measured at the feeding artery of the tissue of interest, which forms the

basis of the arterial input function (AIF) to be discussed later in this thesis. By fitting the measured contrast concentration curve into the mathematical model, the unknown parameters can be estimated. Table 2.1 tabulates the 3 major parameters estimated from the curve fitting and their physiological meanings.

Parameter	Physiological meaning
k_{trans}	Blood plasma flow per unit volume of tissue. In situation of high blood flow, k_{trans} is the permeability surface area product per unit volume of tissue.
v_e	EES volume per unit volume of tissue.
v_p	Blood plasma volume per unit volume of tissue.

Table 2.1: Physiological meaning of the DCE-MRI parameters in the Tofts and Kermode model.

There are several major assumptions in the model:

1. Perfect mixing of contrast agent in the compartment: capillary flow is sufficient to replenish loss of contrast agent into the lesion.
2. The only pathway of depletion of contrast agent from lesion is via the capillaries. Active transport of the contrast agent is not involved. Only diffusion, which is proportional to concentration difference, is involved. At equilibrium, plasma contrast concentration is equal to that in the EES. Diffusion from neighboring

voxels is also ignored.

3. Parameters to be determined are constant during the time of acquisition.

4. Fast exchange of all mobile protons so that tissues relax with a single T1 value, and that Gd-DOTA has a constant relaxivity. T2 effect of contrast agent is neglected.

5. Extraction fraction of the EES is sufficiently low to avoid flow-limited situation. Otherwise the estimation is a mixed effect from permeability and blood flow. In the case where flux across the endothelium is flow limited,

6. $k_{trans} = F\rho(1 - Hct)$ $(PS >> F)$ [2.4]

7. And otherwise in the permeability limited situation:

8. $k_{trans} = PS\rho$ $(PS << F)$ [2.5]

9. where F is the blood flow, PS is the permeability surface area product, ρ is the tissue density, Hct is the haematocrit proportion.

2.3.3 Brix Model

The model is composed of two compartments (central and peripheral compartment) and it is graphically represented in Figure 2.3.

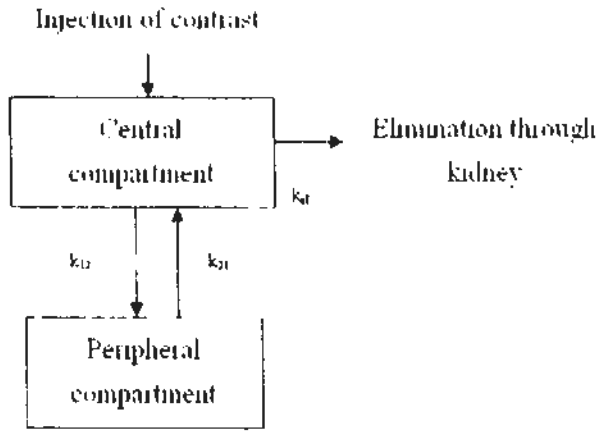

Figure 2.3: The compartmental model proposed by Brix.

Input to the system is assumed to be a continuous injection of contrast agent at a constant rate within a known period of time. In the original model, the curve fitting is carried out directly on the signal intensity-time curve, instead of the derived contrast concentration time curve. The advantage is simplicity in data acquisition and processing with the omission of T1 estimation. However, the drawback is the inaccuracy involved in DCE-MRI parameter estimation. For low baseline T1, and also for a high contrast concentration, the relationship between contrast concentration and signal intensity is not linear. Contrast concentration-time curve was used instead in the studies of this thesis for the parameter estimation of the Brix model so as to give a better representation of the dynamic especially for high contrast concentration. The mathematical representation of the contrast dynamic is represented in the following equations.

$$C_t(t) = A\{v[e^{k_{el}t} - 1]e^{-k_{el}t} - u[e^{k_{21}t} - 1]e^{-k_{21}t}\} \quad [2.6]$$

$$u = \frac{1}{[k_{21}(k_{21} - k_{el})]} \qquad [2.7]$$

$$v = \frac{1}{[k_{el}(k_{21} - k_{el})]} \qquad [2.8]$$

The parameters to be estimated in Brix model, as well as their physiological meaning, are shown in Table 2.2.

Parameter	Physiological meaning
A	Parameter related to the tissue type, infusion rate and a combination of other constants
k_{21}	First order transfer rate constant of contrast agent from the central compartment to the peripheral compartment
k_{el}	First order rate constant of the elimination of contrast agent from the central compartment

Table 2.2: Physiological meaning of the DCE-MRI parameters for the Brix model.

In addition to the assumptions 1-4 listed in the previous section for Tofts' model, the following assumptions are also considered in the Brix model:

1. Zeroth order input of contrast agent into plasma (equal to the infusion rate) is assumed. A first order elimination rate of contrast agent is also used.

2. Transfer rate in and out of the peripheral compartment is the same.

3. Signal enhancement contribution by plasma compartment in the pixel is neglected.

2.4 Overview on DCE-MRI Processing

DCE-MRI involves a number of processing steps after data acquisition to generate the parameters for clinical application. The steps generally include image preparation, contouring, T1 calculation, contrast concentration curve derivation and parameters extraction. Details of the steps are discussed below.

2.4.1 Visual Inspection of Images

The images used in the DCE-MRI processing should be free from artifact in order to generate reliable results. In the first place, the pulse sequence should not be susceptible to artifact. Echo planar imaging which creates substantial artifact in air-tissue interface should be avoided. Other common artifacts that may still contaminate the images are motion artifact and pulsation artifact. This may be partially avoided by appropriate selection of phase encoding direction. However, artifact should still be censored. Visual inspection is a simple and reliable means to identify image artifacts. Images with significant artifact at the area of interest should be discarded.

2.4.2 Image Alignment

Multiple images acquired in DCE-MRI are processed. Misalignment amongst these images may be present due to patient movement, and this will affect accuracy of the DCE-MRI result. Images are aligned manually or automatically by image registration software. Ideally, this should be able to correct for misalignment in 6 dimensions: transformation in the x, y and z direction, together with the rotations (roll, yaw and pitch). Moreover, deformable registration may be necessary if the patient anatomy is deformed. Anatomy deformation in the head and neck region may be contributed by swallowing, changes in neck flexion angle, mandible movement, etc. These may affect areas around the laryngeal region or airway that renders significant misalignment for nearby tumors or organs of interest. Deformable registration is attempted by research groups and software vendors (Tokuda J., Mamata H., Gill R.R., et al., 2011; Fallone B.G., Rivest D.R., Riauka T.A., et al, 2010). Despite the attempt, reliable and accurate non-rigid registration software is still not available. Therefore, if the misalignment is critical and uncorrectable, the images should be discarded.

2.4.3 Contouring

The whole of the tumor and organ of interest should be contoured, as well as the arterial blood supply to the area of interest. The carotid arteries are important source

of oxygenated blood for head and neck tumors (Bailey, Johnson, Newlands, 2006), and should be able to represent the influx of contrast into the tumor. The contoured artery is used to generate the arterial input function (AIF) for subsequent DCE-MRI processing. AIF is important to cater for the variation in contrast enhancement due to cardiac variations, and other machine specific variants. The issue of AIF is further explained in subsequent chapter.

2.4.4 T1 Map Generation

T1 should be estimated to facilitate derivation of contrast concentration from signal intensity. A number of methods exist for T1 estimation, including inversion recovery prepared imaging (Bluml S., Schad L.R., Stepanow B., et al., 1993) and variable saturation technique (Fram E.K., Herfkens R.J., Johnson G.A., et al., 1987). Different methods differ in terms of acquisition pulse sequence, acquisition time and processing algorithm, and their relative merits and demerits are discussed in more detail in chapter 3. Nonetheless, the outcome should be the same. An example of the T1 map derived in the studies of this thesis is shown in Figure 2.4.

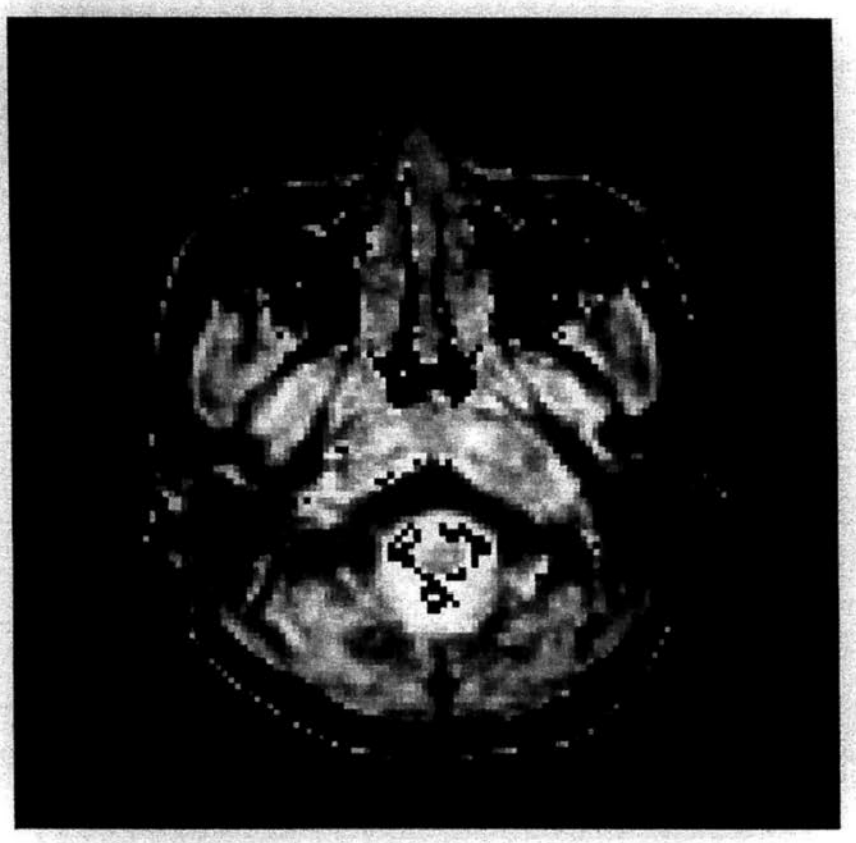

Figure 2.4: A sample T1 map.

2.4.5 Contrast Concentration Curve Derivation

Contrast agents are known to alter the spin-spin relaxation rates of tissues, and thus induce a change in T1. The non-linear relationship between contrast concentration and signal intensity is described by the Bloch formula [2.10]. Using the derived T1, the signal intensity-time curve for each pixel is transformed into contrast concentration-time curve, which is then used in subsequent pharmacokinetic models.

$$C = \frac{T_{10} - T_1}{R_{el} T_{10} T_1} \qquad [2.10]$$

The relaxivity constant is termed R_{el}. C is the contrast concentration, T1 is the tissue T1 value at the presence of contrast, $T1_0$ is the baseline tissue T1.

The relationship between contrast concentration and relative signal increase is plotted in Figure 2.5 for different baseline values of T1. As shown in the figure, the relationship is approximately linear at small concentration of contrast or large T1. This approximation has been exploited in an effort to omit the estimation of T1 in DCE-MRI processing (Judd, Atalay, Rottman, et al., 1995), thus simplifying the data analysis and eliminate variation in outcome due to uncertainty in T1 estimation. Indeed, the Brix model made this approximation in the original article that proposed the model. However, the range of contrast concentration and T1 encountered in different regions of interest may not meet the requirement of this assumption. The baseline T1 for head and neck lesions and parotid glands are about 900 ms and 500 ms respectively, according to data suggested in this thesis. Moreover, tumor contrast concentration at peak enhancement exceeds 1mM, resulting in shortened T1 of approximately 100ms. As shown in the plot of Figure 3.1, the relationship of signal intensity and contrast concentration over this range is curvilinear. Quantitatively, an error of up to 3% in the derived contrast concentration may occur by assuming a linear relationship between contrast concentration and signal intensity with baseline T1 equal to 900ms. The error increases to over 7% with baseline T1 equal to 500ms. Derivation of T1 for individual patient is therefore a necessary procedure in the DCE-MRI of the head and neck region.

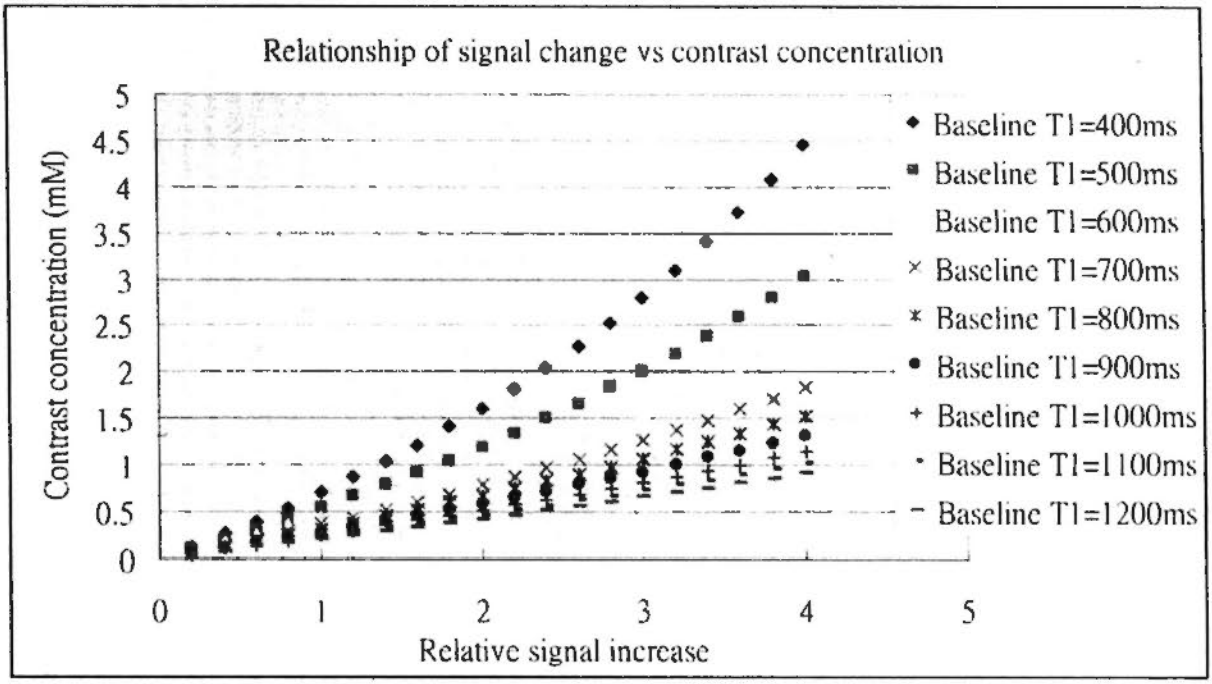

Figure 2.5: Plot of contrast concentration versus relative signal increase.

2.4.6 DCE-MRI Parameter Estimation

The derived contrast concentration curves are fitted into the model equations to estimate the DCE-MRI parameters. Method of mathematical fitting includes nonlinear least square method (Murase K., 2004), simulated annealing (Marsh R.E., Riauka T.A., McQuarrie S.A., 2007) and other novel curve fitting algorithm (Sansone M., Fusco R., Petrillo A., et al, 2011).

An example for the parameter maps of a particular image slice of a patient, taken from the results in the studies of this thesis, is shown in figure 2.6. The parameters from the Tofts and Kermode model, Brix model and the AUC are included.

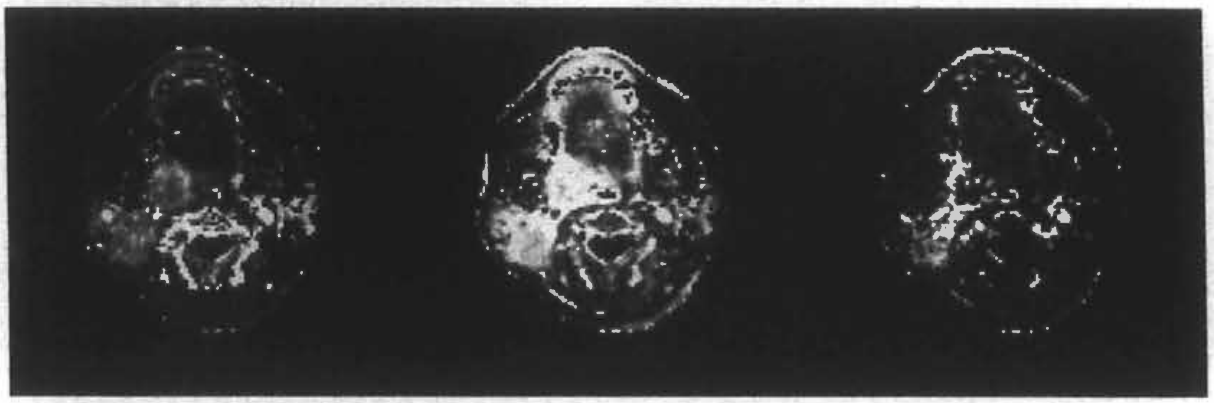

(a) (b) (c)

(d) (e) (f)

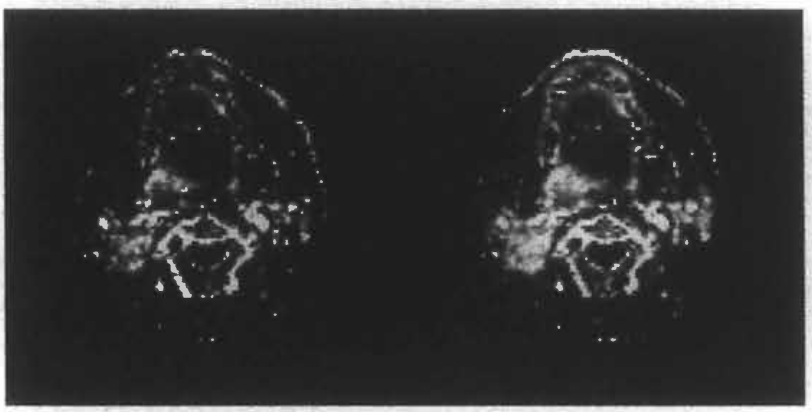

(g) (h)

Figure 2.6: Parameter maps of (a) k_{trans}, (b) v_e, (c) v_p, (d) A, (e) k_{21}, (f) k_{el}, (g) AUC60, (h) AUC90.

2.5 General Requirement of DCE-MRI and Effort of Standardization

Since the development of quantitative DCE-MRI in the early 1990's, different protocols have been used to perform DCE-MRI data analysis. Protocols differed in data acquisition, processing and analysis method, thus making published data difficult to compare and apply across different centers. Also, quality of data could not be guaranteed with non-standardized protocol. Therefore at the beginning of this century, a number of clinical institutions attempted to provide guidelines to standardize DCE-MRI. The recommendations issued by the National Cancer Institute (NCI) of the United States outlined proper data acquisition protocol for DCE-MRI in oncology (Evelhoch, Garwood, Vigneron, et al., 2005). The two fundamental guidelines, namely the 'Dynamic Contrast Enhanced Magnetic Resonance Imaging Workshop' in 1999 and the 'Future Technical Needs in Contrast Enhanced MRI of Cancer Workshop' in 2000, recommended:

1. 3-dimensional DCE-MRI images should be acquired to cover the entire tumor.
2. Data with a minimum temporal resolution of 30 seconds, for a period of at least 90-150 seconds after contrast injection should be acquired. Spatial resolution should be optimized with sufficient resolution for heterogeneity analysis and adequate signal to enable voxel-wise processing of DCE-MRI data.
3. Power injector should be used to inject contrast agent, with saline flush after the injection.

4. Acquisition pulse sequence should not be susceptible to artifact.

5. Data and processed results should be highly reproducible. T1 should be measured with the same spatial resolution as the DCE-MRI data. Processed DCE-MRI results should be independent of scanner system and contrast dose. A quantitative analysis method that takes into account the variation of these attributes should be adopted.

In 2005, the Pharmacodynamic/Pharmacokinetic Technologies Advisory Committee, Drug Development Office, Cancer Research in the United Kingdom suggested the inclusion of cardiac output measurement or arterial input function (AIF) to cater for inter- and intra- patient differences due to cardiac dynamics (Leach, Brindle and Evelhoch, 2005). The scan field of view (FOV) therefore should also include the blood vessels appropriate for derivation of AIF.

It is shown in later chapters, that the acquisition protocol used in this thesis is constructed to conform to these requirements.

2.6 Major Technical Challenges of DCE-MRI

The objective of DCE-MRI is to generate reliable parameters that can reflect vascular properties of the tissue of interest. These results should yield clinical inference or prediction of treatment outcome. To achieve this, standardization of protocol, validation and reproducibility assessment of the data are essential. In the

previous session the international effort to standardize practice of DCE-MRI has been discussed, and the aim of this thesis is to examine an optimal and practical protocol in the head and neck region. In the subsequent chapters the technical problems that are crucial and specific to the application in the head and neck region will be described and investigated.

The acquisition of DCE-MRI data is the first part of the process. Spoiled gradient echo sequences with multiple flip angles are used to determine the T1 of the tissue of interest. Di Giovanni et al (2010) demonstrated a heavy dependence of the accuracy for DCE-MRI parameters on T1 estimation error. Dale et al (2003) stated that the selection of the appropriate flip angles is essential for T1 estimation and during dynamic data acquisition, and that the optimal flip angles depend on the intrinsic T1 of the tissue of interest. This implied that optimization is required for different parts of the body and tissue types. The optimization of flip angles for DCE-MRI in the head and neck region has never been reported, and this is explored in this research project. Details of the study and results are discussed in chapter 3.

Another important factor related to data acquisition is total scan duration of the dynamic acquisition data. Reducing scan duration results in less data processing and therefore improves computational efficiency. However, over-truncation of data in the contrast wash out phase potentially reduces the accuracy of estimated DCE-MRI parameters. Few studies have probed the effect of scan duration on the estimation of

DCE-MRI parameters, except by Yue et al (2010) who showed an increased stability for Tofts' model with increased scan duration. The effect of scan duration on parameter estimation accuracy and precision for typical head and neck lesions, with both the Tofts and Kermode model and Brix model, is studied in chapter 3.

Increased signal-to-noise ratio (SNR) can be achieved by increased field strength and the use of optimal receiver coil. However, assuming that the best equipment on hand is employed, signal can only be increased at the expense of spatial and temporal resolution. This is usually achieved via increased voxel size and number of excitation averages. ROI analysis can be employed in place of pixel-wise analysis to increase the SNR, albeit at the lost of information on parameter heterogeneity. Dale et al (2003) analytically investigated the effect of noise in the data to estimated k_{trans} by propagation of error. In chapter 3 of this thesis, the effect of SNR on other DCE-MRI parameters will be further explored.

AIF is the functional representation of the contrast concentration in the blood supply to the area of interest. It serves as the input function for the contrast dynamic models to generate the DCE-MRI parameters, and is also used to normalize the variation in contrast input to the tissue of interest. These variations are the results of differences in injection timing, injected contrast dose, kidney function and cardiac output of patients. An optimal AIF should be a genuine representation of the contrast concentration from the supplying artery. However, this is difficult in the head and

neck region since the supply artery is usually small, and signal intensity may be contaminated by flow artifact. Besides, temporal resolution needs to be sufficiently high to account for the fast inflow of contrast into the vascular system. Chapter 4 described the effort to obtain an optimal AIF for DCE-MRI processing in head and neck region.

Finally, the DCE-MRI data generated in this thesis are validated by phantom. Reproducibility of the in-vivo data was also evaluated. These are important assessments on the integrity of the data and results. The assessment also provides the technical validation for the clinical utilization of the data.

3.1 Introduction

Data acquisition is important in DCE-MRI, and it affects substantially the quality of the DCE-MRI results. Data acquired for DCE-MRI are used for two major processing steps: T1 estimation and DCE-MRI parameter estimation. In this chapter, the technical issues in data acquisition are discussed and investigated. The objective of the investigation is to arrive at an optimal protocol of data acquisition for DCE-MRI in the head and neck region. The choice of flip angles was known to influence substantially the outcome of T1 estimation (Dale B.M., Jesberger J.A., Lewin J.S., et al., 2003), and thus will be investigated. As for DCE-MRI parameter estimation, the quality of the data acquired during dynamic acquisition is essential. Several factors that may influence the data quality are the choice of flip angles, signal-to-noise ratio (SNR) (Dale B.M., Jesberger J.A., Lewin J.S., et al., 2003) and scan duration (Yue C., Li D., Shen Z., et al., 2010). These factors will be investigated in the subsequent sections of this chapter.

3.2 T1 Determination and Validation

3.2.1 Introduction

T1 determination is an essential part of DCE-MRI data processing. The

estimated T1 is used to derive contrast concentration from signal intensity, and this is then used for subsequent pharmacokinetic modeling.

Two major methods for T1 determination are available: inversion recovery prepared imaging and variable saturation technique. The former uses inversion recovery pulse and signal acquisition at different delay times. Difference in net magnetization recovered after different delay times, which depends on the relaxation rate, results in different signal intensities. T1 can therefore be deduced with good accuracy (Bluml S., Schad L.R., Stepanow B., et al., 1993). The disadvantage of this method is the long inversion recovery (delay) time for each signal acquisition, especially for high values of T1. The total time for typical pulse sequences to determine a T1 map of matrix size 128 x 128, with 4 inversion recovery times, exceeds 10 minutes.

The variable saturation technique is a more practical method for T1 determination. With the use of different excitation flip angles, the signal intensity is related to T1 by the Equation [3.1]. Multiple flip angles are used to acquire data for T1 estimation. Spoiled gradient echo sequences with low flip angles are preferable with the short acquisition time, and the practicality of the method is shown by Dale et al (2003). Typical acquisition time with this technique, for a matrix size of 128 x 128 and 4 flip angles is about 1 minute.

In order to yield reliable results, the number and range of flip angles used in the

spoiled gradient echo sequences have to be optimized for tissue T1 and contrast concentration in head and neck tumors and organs of interest (Dale, Jesberger, Lewin, et al., 2003; Evelhoch, 1999; Schabel and Parker, 2008). Images acquired with the use of 2 or more flip angles can be used to determine T1 for each pixel by curve fitting. Theoretically, in the absence of image noise, T1 can be determined with high accuracy at a minimal number of small flip angles. With the presence of image noise, more flip angles have to be used and the optimal range of flip angle has to be determined. Study on this issue by simulation is presented in this chapter. Validation of the derived acquisition protocol was conducted by the use of a T1 phantom and in-vivo data.

3.2.2 Effect of Different Number of Flip Angles on T1 Estimation

3.2.2.1 Method

Monte Carlo simulation was performed by the use of software written in Interactive Data Language (IDL, Boulder, CO, USA). The aim of the simulation is to examine the use of 3, 4, 5 and 6 flip angles in the range of 2-30 degrees to yield gradient echo intensities for T1 estimation. The following elaborated Bloch formula (Haase A., Frahm J., Matthaei D., et al., 1986) was used which denotes the incorporation of random noise in the simulation:

$$S_{ij}(\alpha_i) = \frac{M_o \sin\alpha_i (1 - El_o)}{(1 - El_o \cos\alpha_i)} + R_{ij} \qquad [3.1]$$

with $El_o = e^{-\frac{TR}{T1_0}}$

where $S_{ij}(\alpha_i)$ is the simulated gradient echo intensity,

i = 0 to 2, to simulate estimation of T1 by 3 flip angles, $\alpha_0 = 2^o$, $\alpha_1 = 15^o$, $\alpha_2 = 30^o$

i = 0 to 3 for 4 flip angles, $\alpha_0 = 2^o$, $\alpha_1 = 10^o$, $\alpha_2 = 20^o$, $\alpha_3 = 30^o$

i = 0 to 4 for 5 flip angles, $\alpha_0 = 2^o$, $\alpha_1 = 9^o$, $\alpha_2 = 16^o$, $\alpha_3 = 23^o$, $\alpha_4 = 30^o$

i = 0 to 5 for 6 flip angles, $\alpha_0 = 2^o$, $\alpha_1 = 8^o$, $\alpha_2 = 13^o$, $\alpha_3 = 19^o$, $\alpha_4 = 24^o$, $\alpha_5 = 30^o$

j = 0, 999, depicting 1000 sets of simulated data for each of the above 4 simulation scenarios. R_{ij} is the Gaussian random number assigned to the simulated data, representing the random noise component encountered in gradient echo images. The standard deviation of the random number was chosen such that the signal to noise ratio (SNR) at the peak of enhancement for the sequence with 30 degree flip angle is 20. This is approximately the noise level encountered in the gradient echo images acquired in the present studies.

M_0 is the proton density and was arbitrarily chosen; TR= 2.7ms is the repetition time, and was chosen to be short and practical for implementation in a 1.5T scanner. $T1_0$ is the T1 value to be estimated.

T1 for each simulated data was estimated by multiple starting point Marquardt-Levendag curve fitting (Ahearn, Staff, Redpath, et al., 2005), which was implemented by in-house developed software written with IDL. For each simulation scenario (3, 4, 5 and 6 flip angles), the coefficient of variation (C.V.) for the T1 estimation was obtained by analyzing the statistics of the simulated T1 estimation.

3.2.2.2 Results

The simulation result is plotted in Figure 3.1.

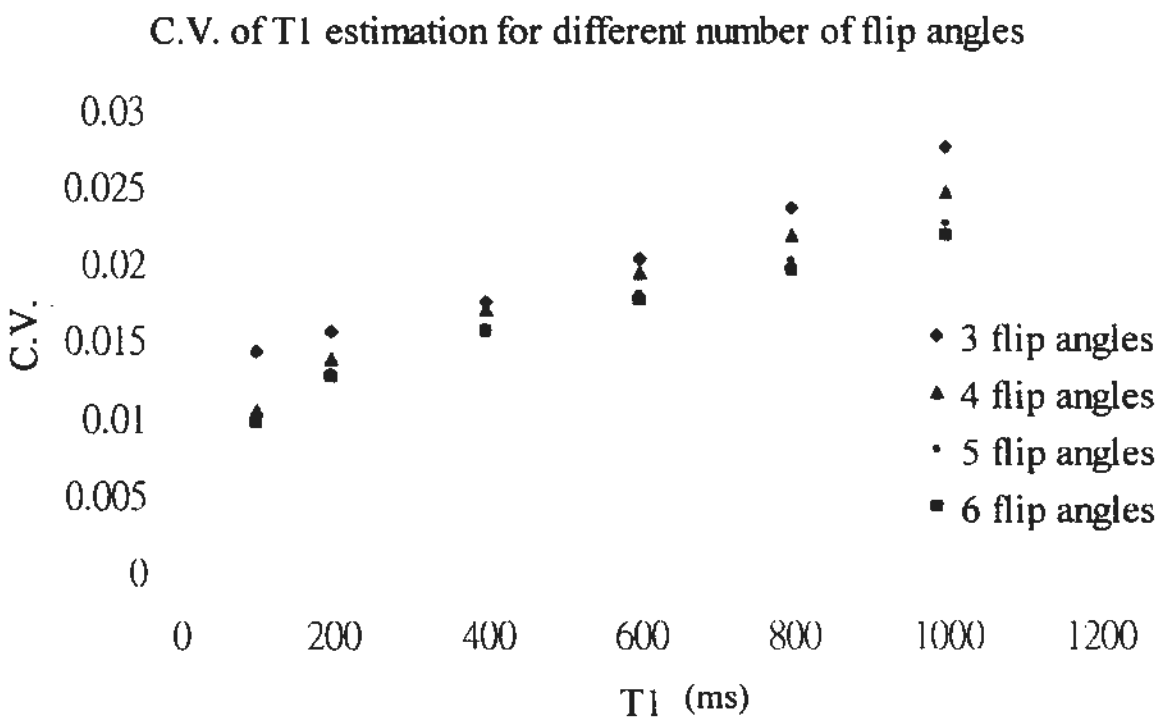

Figure 3.1: Coefficient of variation for T1 estimation with different number of flip angles.

A reduction in C.V., representing a higher precision of T1 estimation, was

achieved with increasing number of flip angles. The use of 5 flip angles provided similar results as compared to the use of 6 flip angles. The use of 4 flip angles provided slightly worse results in terms of precision, but attained similar results to the use of 5 or 6 flip angles at low T1. Further reducing the number of flip angles to 3 gave worse results over the whole range of T1 as compared to the use of 4 flip angles. The use of 4 flip angles was considered optimal.

3.2.3 Effect of Different Range of Flip Angles on T1 Estimation

3.2.3.1 Method

A Monte Carlo simulation similar to section 3.2.2 was performed. Instead of using different number of flip angles, different ranges of flip angles were used. Three scenarios were examined, with flip angles in the range of 2 – 10°, 2 – 30°, 2 – 60° respectively. Four flip angles evenly spaced within the ranges were assigned, thus the indexed flip angles in the elaborated Bloch formula [3.1] became 2, 5, 8 and 10 for the range of 2-10 degrees; 2, 10, 20 and 30 for the range of 2-30 degrees; 2, 20, 40 and 60 for the range of 2-60 degrees. Curve fitting, T1 estimation and data analysis similar to that described in section 3.2.2 was performed.

3.2.3.2 Results

Result of the simulation is shown in Figure 3.2.

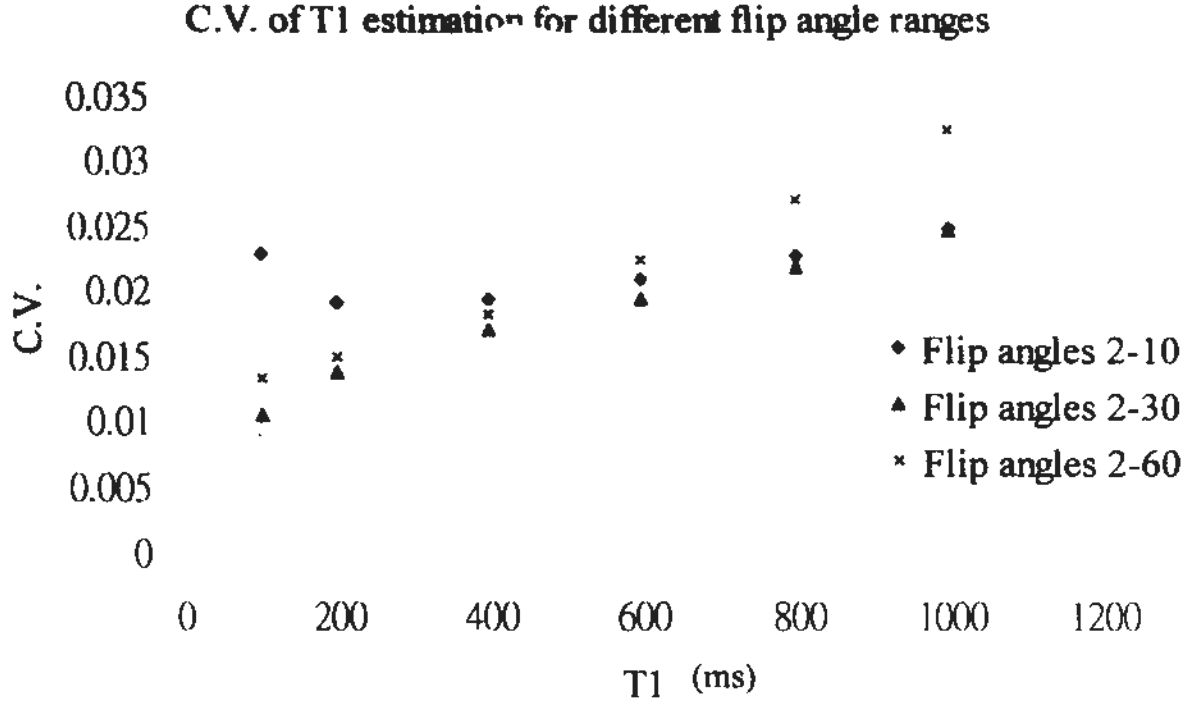

Figure 3.2: Coefficient of variation of T1 estimation for different ranges of flip angles.

It was shown that flip angles in the range of 2 – 30 degrees demonstrated lower C.V., thus higher precision for T1 estimation, than the other two ranges over all values of T1. This is therefore considered the optimal range used in the DCE-MRI acquisition protocol.

3.2.4 Phantom T1 Validation

3.2.4.1 Method

The protocol was used in 1.5T MR scanner (Philips Medical System, Best, the Netherlands) with the head and neck SENSE coil. Optimized flip angles (repetition

time, TR = 2.7 ms; echo time, TE = 0.9 ms; slice thickness, TH = 4 mm; matrix size = 128 x 128; field of view, FOV = 230 mm; number of acquisitions, NSA = 4, 4 flip angles, $\alpha_0 = 2^o$, $\alpha_1 = 10^o$, $\alpha_2 = 20^o$, $\alpha_3 = 30^o$) was validated by the use of Eurospin MRI T1 phantom. The phantom is made of a cylinder with 10 regularly spaced holes designed to allow the insertion of liquid gels containers of different predetermined T1 value.

3.2.4.2 Results

Figure 3.3 showed the estimated T1 map. The standard T1 values at the scanner room temperature, as specified in the manual of the phantom, and the estimated T1 by the acquisition protocol are shown in Table 3.1.

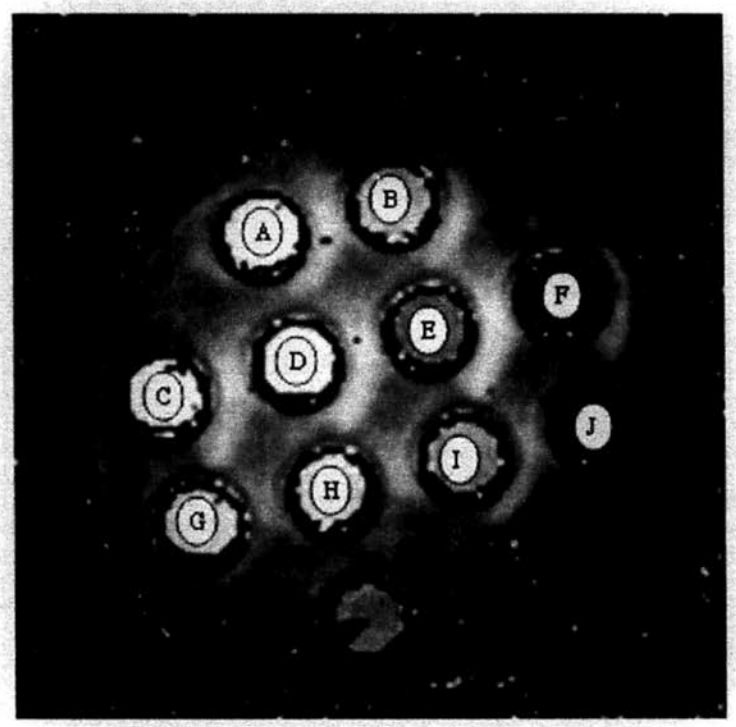

Figure 3.3: Estimated T1 map of the Eurospin MRI T1 phantom.

Test Object	Standard T1 (ms)	Estimated T1 (ms)	Error %
A	1278	1315.5	2.934
B	828	774	-6.522
C	1385	1354	-2.238
D	1068	1028.5	-3.699
E	506	560	10.672
F	329	357	8.511
G	992	921	-7.157
H	822	914.5	11.253
I	664	685	3.163
J	221	228.5	3.394
Mean Error %			2.03 ± 6.78%

Table 3.1: Standard T1 of the test objects (provided by the phantom manufacturer), the estimated T1 and the estimation error.

The mean error of the T1 estimation is about 2%, with a range of -7.2% to 10.7%. This is in accordance to the range of error reported by Chang et al. (2008) that used multiple spoiled gradient echo sequences for T1 estimation.

3.2.5 In-vivo T1 Validation

3.2.5.1 Method

T1 estimation was further validated in human subjects. A total of ten head and neck cancer patients were selected to undergo the DCE-MRI image acquisition. T1 map was obtained after data processing. ROIs of subcutaneous fat and muscles were contoured on these patients.

On the other hand, the reproducibility of T1 estimation was also assessed in these human subjects. The ten patients were scanned once more after 2 weeks, before chemoradiation therapy and after the start of a targeted therapy drug, Cetuximab. The drug is assumed to induce minimal effect on normal tissues and organs. T1 map was again generated and the subcutaneous fat and muscles on each scan were contoured. The region of interest for the subcutaneous fat and muscles were chosen to ensure reproducible location at the two scans. In the study of this thesis, reproducibility is assessed by the two parameters: the within patient coefficient of variance (wCV) and reproducibility. The two attributes indicated the degree of variation of the DCE-MRI parameters that would be expected from a group of patients, and from individual patients respectively. The expressions for the two attributes are:

$$\mathrm{wCV} = \sqrt{\frac{\sum \mathrm{d}^2}{\mathrm{n}}} \frac{1}{\mu\sqrt{2}} \qquad [3.2]$$

$$reproducibility = 2.77 \times \sqrt{\frac{\sum d^2}{n}} \frac{1}{\mu\sqrt{2}} \qquad [3.3]$$

where d is the difference between the two scans, n is the number of lesions in the study. μ is the mean of the parameter. If a significant correlation is observed between d and the average value of the two scans, a logarithmic transformation has to be performed and the two reproducibility parameters become:

$$wCV = 10^{\sqrt{\frac{\sum d^2}{2n}}} - 1 \qquad [3.4]$$

$$reproducibility = \frac{100 \times 10^{\log \mu \pm 2.77 \sqrt{\frac{\sum d^2}{2n}}}}{\mu} \qquad [3.5]$$

3.2.5.2 Results

The mean T1 of the subcutaneous fat and muscles were 270.6 ± 71.6 ms and 880 ± 160 ms respectively, which are in agreement with previously published in-vivo data in 1.5T scanner. Duewell et al. (1995) reported mean T1 of 310 ms for subcutaneous fat and 980 ms for muscle. The resulting reproducibility of the T1 for subcutaneous fat and muscles are, 29.6% and 17.7% respectively, and for the wCV, 10.7% and 6.4% respectively

3.2.6 Discussion

Spoiled gradient echo pulse sequence was used in the acquisition protocol with a reasonable scan time of about 1 minute. The optimal number of flip angles was determined to be 4, and the optimal range is 2-30 degree. The flip angles thus used to

estimate T1 are 2, 10, 20 and 30 degrees. The pulse sequence was validated by the use of a T1 phantom, and the average T1 estimation error was about 2%. In-vivo validation showed that the derived T1 for subcutaneous fat and muscles were similar to published values, and the T1 estimation was reproducible with reproducibility for subcutaneous fat and muscles being 29.6% and 17.7% respectively. The resultant optimal flip angle was in agreement with that suggested in Wang et al (1987) for cases of short acquisition time and short TR.

3.3 Dynamic Data Acquisition

3.3.1 Introduction

Dynamic acquisition pulse sequences are used to acquire high temporal resolution images for DCE-MRI analysis after contrast injection. These images represent the dynamical change in contrast concentration during the period of interest. An optimal dynamic pulse sequence should generate images with: sufficient temporal and spatial resolution, sufficient signal-to-noise ratio; adequate image coverage. The spatial resolution and field of view should be chosen as the same as that in the spoiled gradient echo pulse sequences for T1 estimation.

With the short acquisition time, spoiled gradient echo is used during dynamic acquisition after contrast injection. The optimal flip angle used for the dynamic acquisition pulse sequence was examined. The flip angle was chosen such that for

typical T1 values and contrast concentration in head and neck region, the signal increase was maximized after contrast injection. Moreover, B1-field inhomogeneity exists that causes error in excitation flip angles. The signal change should be relatively constant with flip angles, so that sensitivity to flip angle errors can be reduced (Brookes, Redpath, Gilbert, et al. 1999).

Signal-to-noise ratio (SNR) in dynamic images is usually limited due to the short acquisition time. Assuming that the best equipment on hand is employed, a higher SNR in the images can be obtained by sacrificing the spatial resolution. Contrast concentration curves averaged over the whole ROI can be used instead of pixel-wise analysis, and the averaging will reduce the noise level. The disadvantage of this method is the removal of the heterogeneity information of the derived parameters. In general, better SNR leads to better accuracy and precision of estimated DCE-MRI parameter, and different parameters have different sensitivity to SNR. The following discussed the impact of SNR on parameter estimation.

Another important aspect that influences the data quality is the scan duration. Increased scan duration of dynamic images reduces the efficiency of the data acquisition and processing. However, acquiring data for a longer period of time would increase the amount of information, and the accuracy of the estimated DCE-MRI parameters could be improved. While reducing the scan duration beyond a certain level could result in unstable estimation of the DCE-MRI parameters, a

compromise is required between the scan duration and the quality of the parameter estimation. This issue will also be examined in this chapter.

3.3.2 Optimal Flip Angle for Dynamic Data Acquisition

3.3.2.1 Method

The relationship of flip angles, signal increase and contrast concentration is depicted in equations [3.6] to [3.7].

$$R_1(t) = -\frac{1}{TR}\ln\left(\frac{1-(A+B)}{1-(A+B\cos\alpha)}\right) \qquad [3.6]$$

$$C(t) = \frac{R_1(t) - R_{10}}{R_{el}} \qquad [3.7]$$

where $A = \frac{S(t)-S(0)}{M_0 \sin\alpha}$, $B = \frac{1-El_0}{1-El_0\cos\alpha}$ and $El_o = e^{-\frac{TR}{T1_0}}$

The relaxivity constant R_{el} was taken as 4.39/s/mM, which was reported for in-vitro samples at 37°C and 1.5T magnetic field (Fischbein N.J., Noworoslski S.M., Henry R.G., et al., 2003). C(t) is the contrast concentration at time t. TR = 2.7ms and is the repetition time. $R_{10}=1/T1_0$ where $T1_0$ is the baseline T1. α is the flip angle, M_0 is the proton density and was arbitrarily chosen. S(t) is the signal intensity at time t, which is the signal intensity after contrast enhancement in this simulation. S(0) is the baseline signal intensity. Thus the signal increase is represented by [S(t)-S(0)]/S(0).

Plots of the signal increase with respect to flip angles for different T1 and contrast concentration are generated. The range of T1 was chosen to be 200, 300, 400, 500, 600, 700, 800, 900 and 1000 ms, and the contrast concentration was chosen to be 0.2, 0.5 and 1 mM. These values were selected to represent the typical values encountered in head and neck DCE-MRI. Plots of signal increase versus flip angles are generated at discrete flip angles spaced 2 degrees apart, within the range of 2 to 24 degree, and the range contains the angle that yield the maximum signal increase. The plots are examined for flip angles that give the maximum signal increase, and are used for determination of the optimal flip angle for dynamic data acquisition.

3.3.2.2 Results

Plots of signal increase with respect to flip angles for different T1 and contrast concentration are shown in Figure 3.4 to 3.6.

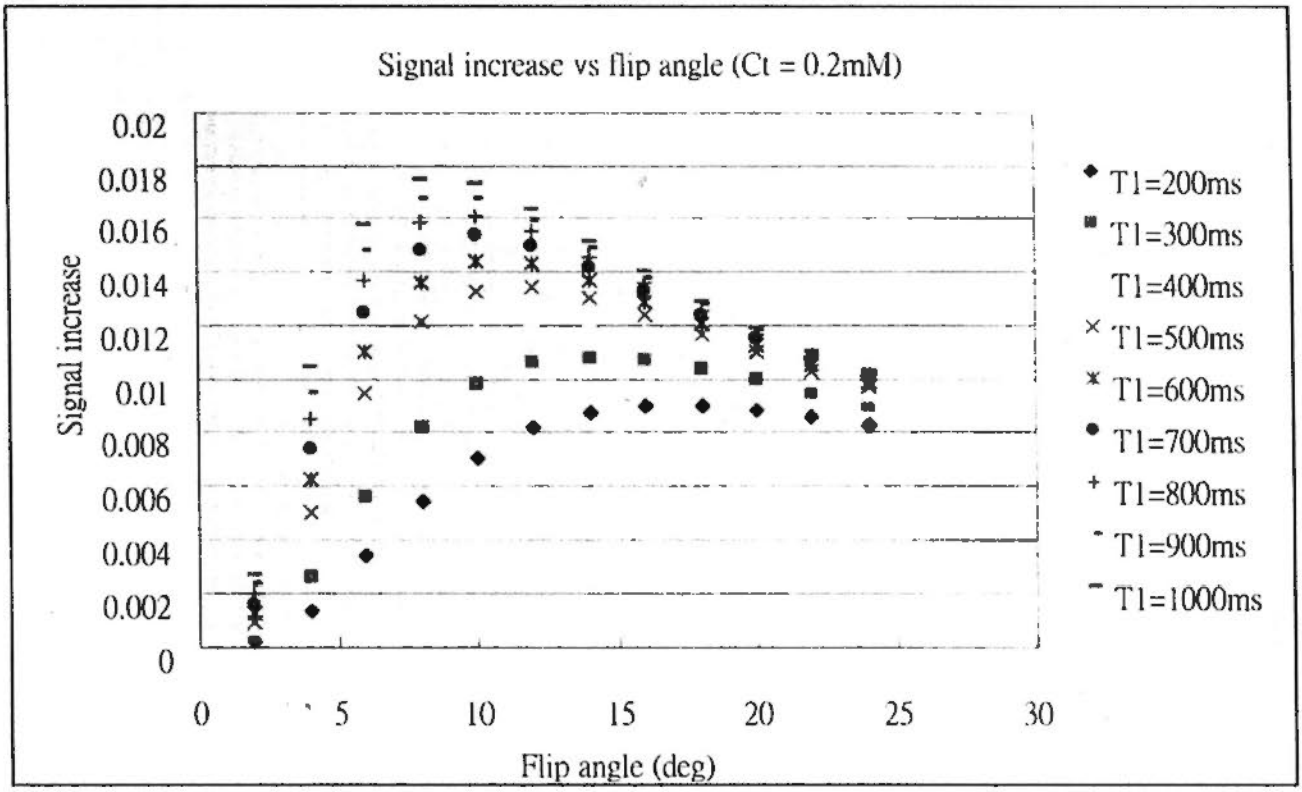

Figure 3.4: Plot of signal increase with respect to flip angles for different T1 with Ct = 0.2mM.

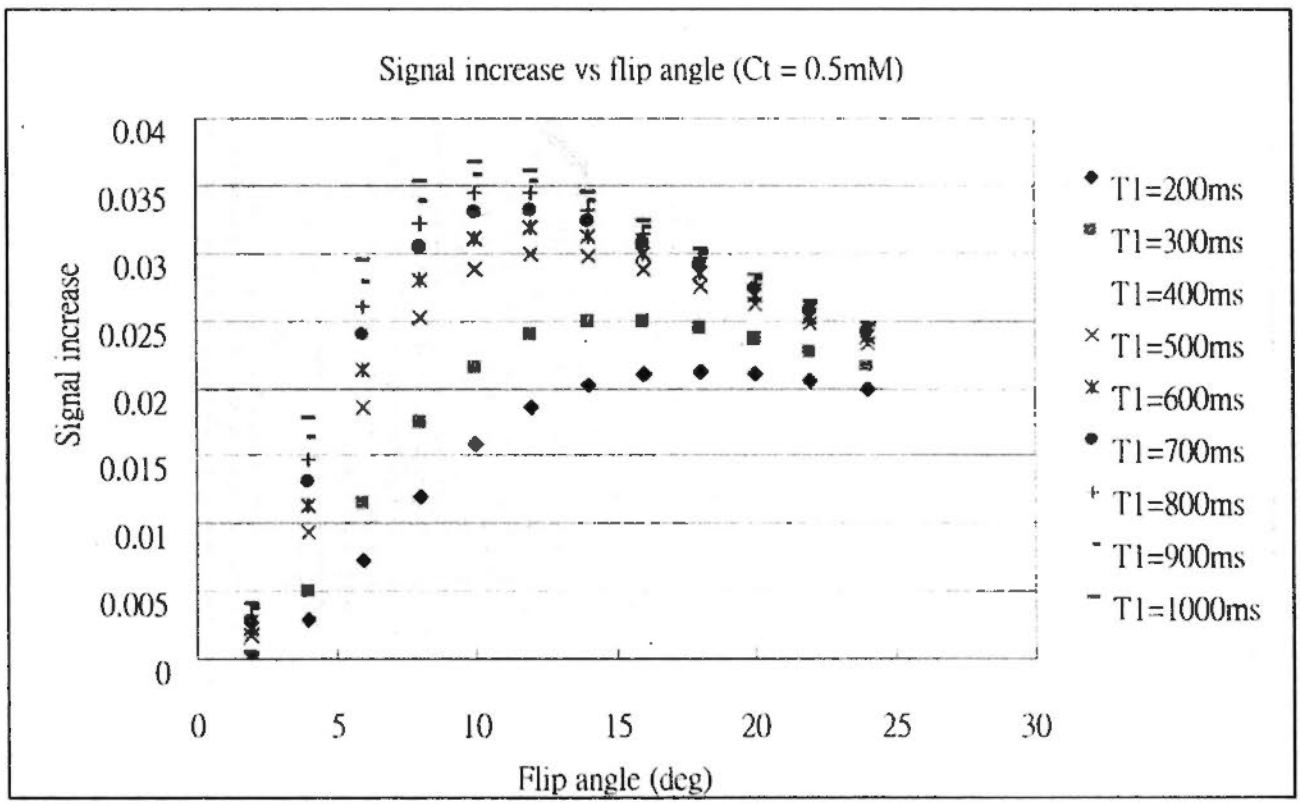

Figure 3.5: Plot of signal increase with respect to flip angles for different T1 with Ct = 0.5mM.

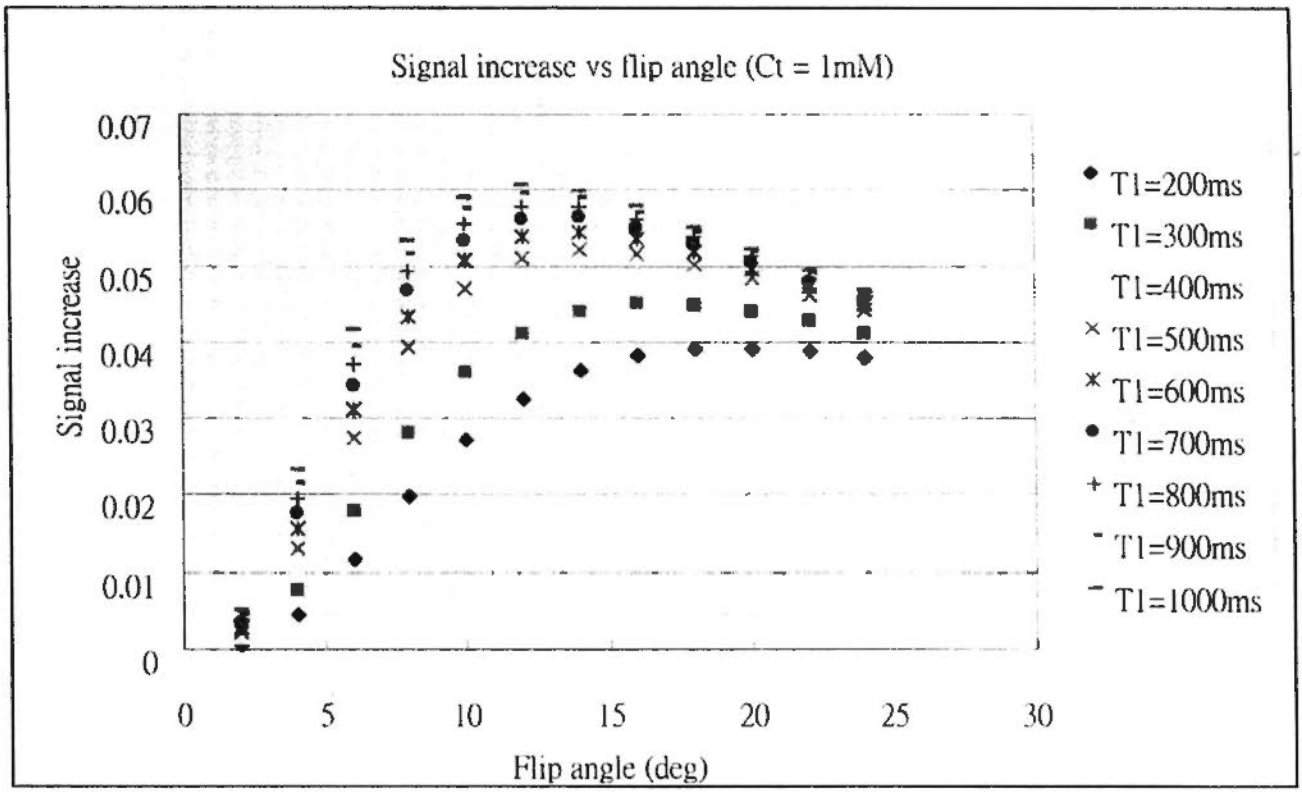

Figure 3.6: Plot of signal increase with respect to flip angles for different T1 with Ct = 1mM.

From the above figures, the flip angle that induces maximum signal increase depends on T1 as well as contrast concentration. The higher the T1 and the contrast concentration, the higher is the flip angle to generate maximum signal increase. For the range of T1 between 200 and 1000 ms and contrast concentration of 0.2 – 1 mM, signal increase is maximized for flip angles of about 8 – 20 degrees. However, at lower flip angles, the signal increase is highly sensitive to change in flip angles. This is shown by the rapid falloff of signal increase when the flip angle is reduced to less than 10 degree. A small error in flip angle may induce a large difference in signal increase, which is not desirable. A flip angle of 20 degree is therefore chosen.

3.3.3 Effect of Signal to Noise Ratio on DCE-MRI Parameter

3.3.3.1 Methods

Monte Carlo simulation using in-house developed software was used to illustrate the effect of noise on parameter estimation. Artificial contrast concentration time curves were generated mathematically using the 2 model equations, from the model proposed by Tofts and Kermode, and from the model by Brix described in chapter 2. Typical values of k_{trans}, v_e and v_p for lesions and normal parotid glands were used in Tofts and Kermode model to construct the curves. Similar contrast dynamic curves were constructed by the Brix model with typical values of A, k_{el} and k_{21} for lesions and parotid glands. Parameters used for lesions were: k_{trans}=1.197 min^{-1}, v_e=0.665, v_p=0.093, A=50, k_{el}=0.004 sec^{-1}, k_{21}=0.022 sec^{-1}. Parameters used for parotid glands were: k_{trans}=0.886 min^{-1}, v_e=0.421, v_p=0.044, A=37.7, k_{el}=0.006 sec^{-1}, k_{21}=0.02 sec^{-1}.

Gaussian distributed random noises, with SNR levels of 3, 6, 12 and 24, were added to the curves. These SNR levels were typically encountered in contrast concentration curves in the images acquired with the established protocol. One thousand contrast concentration curves for each of the 4 SNR levels, were generated for each combination of DCE-MRI parameters. These curves were used for DCE-MRI parameter estimation. The estimated results were used as statistics to calculate the accuracy (mean percentage deviation of estimated value from the

expected value) and the precision (coefficient of variation expressed in percentage) of the DCE-MRI parameters.

3.3.3.2 Results

The results of the simulation data, expressed in: accuracy (precision), are shown in Table 3.2 and Table 3.3.

	SNR = 24	SNR = 12	SNR = 6	SNR = 3
k_{trans}	0.8 (9.1)	0.4 (18)	-2.3 (32)	0.3 (53.9)
v_e	-0.5 (4.3)	-1.2 (7.3)	-2.9 (13.5)	-4.9 (22.7)
v_p	-2.1 (38)	7.2 (37.2)	29.3 (85.8)	60.8 (102.7)
A	13.0 (15.2)	11.3 (15.1)	14.4 (15.1)	14.1 (18.1)
k_{el}	33.7 (0)	33.7 (0)	30.7 (9.9)	25.3 (24.6)
k_{21}	0.1 (7.6)	-1 (8.3)	2.1 (12.9)	5.3 (17.8)

Table 3.2: Results of parameter estimation in simulated parotid glands. Results are expressed as accuracy (precision). Accuracy = [mean % deviation (estimated value - expected value)]. Precision = (% coefficient of variation).

	SNR = 24	SNR = 12	SNR – 6	SNR = 3
k_{trans}	1.2 (8.5)	0.6 (12.1)	1.5 (22.3)	3.9 (37.4)
v_e	-0.1 (3.4)	-0.1 (5.1)	-0.6 (9)	-0.9 (15.9)
v_p	-2.3 (26.1)	-0.2 (34.6)	3.7 (55.7)	10.4 (89.1)
A	0 (0)	0.5 (3.4)	1.9 (6.4)	6.5 (13.5)
k_{el}	-6.4 (8.6)	-5.5 (11.1)	-3.2 (17.4)	-1.9 (25)
k_{21}	3.5 (3.5)	3.4 (5.1)	4.3 (8.1)	8.4 (10.7)

Table 3.3: Results of parameter estimation in simulated tumors. Results are expressed as accuracy (precision). Accuracy = |mean % deviation (estimated value - expected value)|. Precision = (% coefficient of variation).

Results showed a trend of reducing precision with increasing noise for all parameters. Accuracy of parameter estimation, denoted by mean estimation error, improved with reduced noise for all parameters except k_{el}. v_p is the most susceptible to noise, and it demonstrated a large percentage coefficient of variation (>60%) at low SNR. The parameters k_{trans} and v_e demonstrated the highest accuracy at different levels of SNR, achieving less than 5% deviation from the expected value. The parameters k_{21} and A demonstrated the highest degree of robustness (<20% in percentage coefficient of variation) in terms of precision for parameter estimation at different SNR levels. Similar observations are shown in the simulation for tumors

and parotid glands.

3.3.4 Effect of Scan Duration on DCE-MRI Parameter

3.3.4.1 Method

DCE-MRI curves from the ROI of undifferentiated head and neck carcinomas from 13 patients were taken to examine the effect of scan duration on DCE-MRI parameter. Contrast concentration curves of acquisition duration ranging from 231 sec to 371 sec, in discrete spacing of 7 sec, were used for curve fitting to estimate the DCE-MRI parameters. The baseline value for each DCE-MRI parameter was chosen to be the estimated parameter from the contrast concentration curve with scan duration = 371 sec. The estimated parameters from curves with difference scan duration were normalized by this baseline value. The averaged and the standard deviation of the normalized estimated values were obtained. Besides, curve fitting was considered unsuccessful if one of the following criteria was met: (1) Mean fitting absolute error > 0.5 or, (2) Estimated v_e and $v_p < 0$ or > 1 or, (3) k_{trans}, Λ, k_{el} and $k_{21} < 0$. Repeated measures ANOVA tests were performed for each DCE-MRI parameters to identify whether there was any difference in parameters induced by a difference in scan duration.

3.3.4.2 Results

The percentage of unsuccessful curve fitting is shown in Table 3.4. The normalized estimated values for each DCE-MRI parameters are plotted against the scan duration in Figure 3.7. The standard deviations are shown as error bars in the plots.

Scan duration (sec)	340-371	305-340	270-304	231-269
Tofts and Kermode	0	0	0	0
Brix	3.1%	9.2%	9.2%	15.4%

Table 3.4: Proportion of DCE-MRI curves that failed curve fitting.

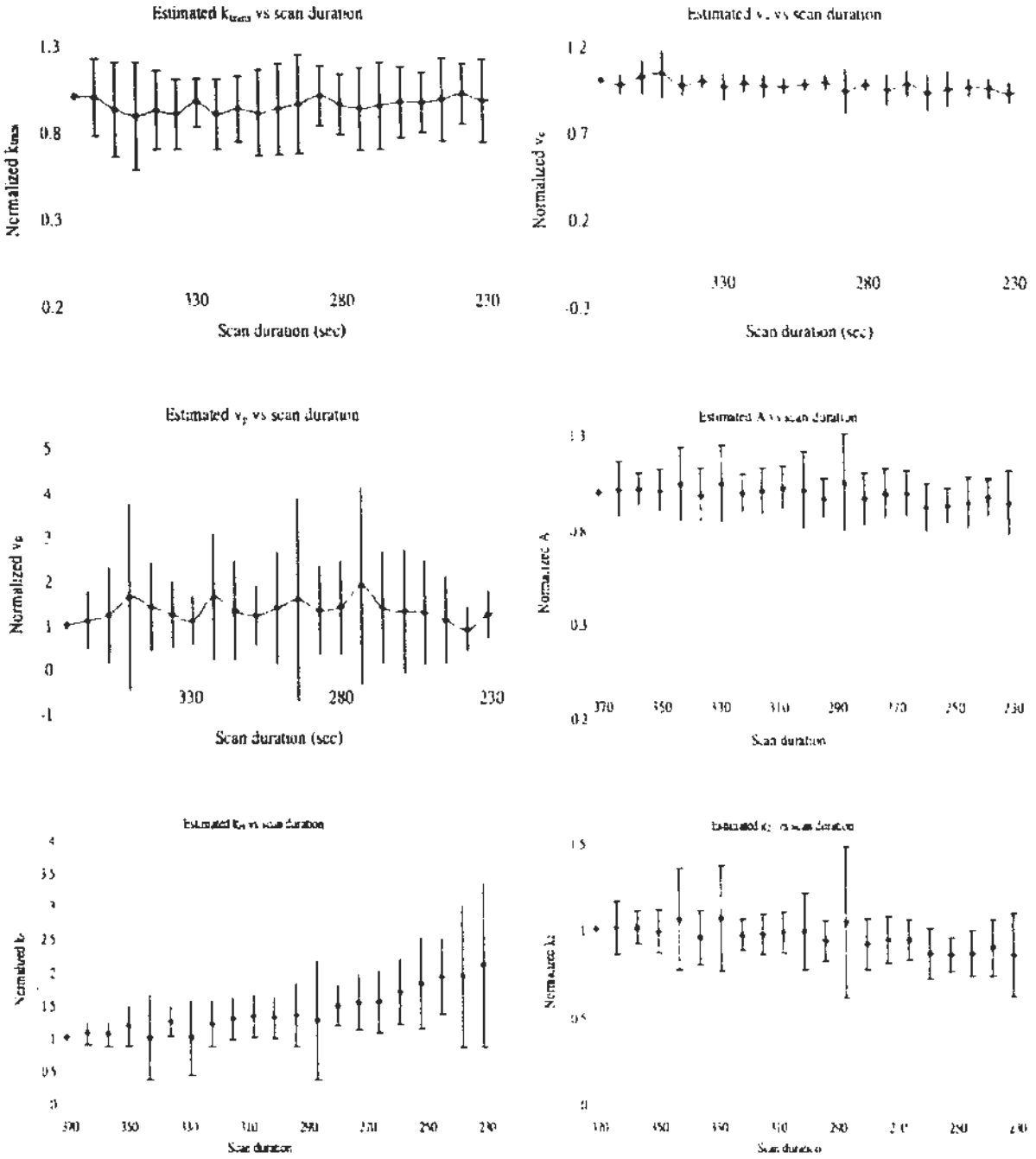

Figure 3.7: Variation of estimated DCE-MRI parameters versus scan duration.

Statistical tests showed that the parameters of the Tofts and Kermode model estimated from reduced scan duration were not significantly different from the baseline value. For the Brix model, the parameter A estimated from different scan duration was not significantly different from the baseline value. For the parameter k_{el},

estimated values with scan duration less than or equal to 280 sec were significantly higher than the baseline value ($p < 0.05$), while for k_{21}, estimated values with scan duration less than or equal to 259 sec were significantly lower than the baseline value ($p < 0.05$).

Results also showed that curve fitting was successful for the Tofts and Kermode model at reduced scan duration down to 231 sec. The Brix model did not show such stability, and the proportion of failure in curve fitting increased with reduced scan duration. Failure in curve fitting approached 10% at scan duration of 305 sec or lower.

In general, the Tofts and Kermode model demonstrated a higher stability than the Brix model, except for the parameter of v_p. As evident from the plots in Figure 3.7, v_p varied substantially at different scan duration, signifying the instability of the parameter. Other than this, scan duration down to 231 sec seemed to be sufficient for use in Tofts and Kermode. If Brix model is employed, reduced scan duration created increased curve fitting failure and significant change in the estimated parameters.

3.3.5 Discussion

Results revealed that by using flip angle of 20 degrees in the dynamic acquisition, the signal increase due to accumulation of contrast agent is maximized, while the sensitivity of signal increase to flip angle error is reduced. Schabel and

Parker (2008) attempted to search for the optimized flip angle for the different gradient echo sequences in the dynamic acquisition of DCE-MRI. In one of the sequences that they have studied, which was similar to the sequences used in this study in terms of TR, TE, temporal and spatial resolution, they arrived at an optimal flip angle of about 20 degrees, which agreed to the result in this study.

Reduction of SNR in the dynamic acquisition reduces precision and accuracy for DCE-MRI parameters. v_p is the most susceptible to noise, and it demonstrated a large percentage coefficient of variation (>60%) at low SNR. The parameters k_{trans} and v_e demonstrated the highest accuracy at different levels of SNR, achieving less than 5% deviation from the expected value. The parameters k_{21} and A demonstrated the highest degree of robustness (<20% in percentage coefficient of variation) in terms of precision for parameter estimation.

With reduced scan duration, the Tofts and Kermode model demonstrated a higher stability than the Brix model, except for the parameter of v_p. Scan duration down to 231 sec seemed to be sufficient for use in Tofts and Kermode. If Brix model is employed, reduced scan duration created increased curve fitting failure and significant change in the estimated parameters.

Few studies have investigated the effect of SNR and scan duration on estimation of DCE-MRI parameters. Yue et al (2010) has reported on the effect of noise and scan duration on DCE-MRI parameters for cranial lesions, using a standard

pharmacokinetic model which is similar to the Tofts and Kermode model explored in this thesis. Their result showed that reduced SNR or scan duration increased the instability and estimation bias. However, they showed a better stability for the parameter of v_p than the parameters of k_{trans} and k_{ep} ($k_{ep} = k_{trans}/v_e$). This is in contrary to the result of the present study. One possible reason may be the difference in the range of DCE-MRI parameters, which was suited for cranial lesions instead of head and neck lesions. Another possible reason may be the lower noise level hypothesized in their study, which may improve the stability more substantially than the other two parameters. However, the exact reason for the discrepancy would require further investigation.

3.4 Summary

The issues pertaining to data acquisition for the DCE-MRI of the head and neck region were examined. The optimal flip angles used in the spoiled gradient echo sequences was determined to be 2, 10, 20 and 30 degrees. T1 estimation was validated to yield good accuracy and reproducibility.

The flip angle for the dynamic acquisition was chosen to be 20 degree to yield good signal increase as well as less sensitivity to flip angle errors. Reduced SNR in the dynamic acquisition was shown to reduce precision and accuracy in the estimation of all parameters. The parameters k_{trans} and v_e demonstrated the highest

accuracy even at low SNR. v_p is the most susceptible to noise in estimation precision. The parameters k_{21} and A demonstrated the highest degree of robustness in terms of precision for parameter estimation at different SNR levels. The results showed the reliability of certain DCE-MRI parameters, namely the k_{trans}, v_e, A and k_{21} in situation of low SNR. Pixel-wise analysis is thus possible for these parameters. For other parameters that are less robust, such as v_p, ROI analysis is more appropriate. Otherwise methods have to be sought to increase the SNR.

With reduced scan duration, the Tofts and Kermode model demonstrated a higher stability than the Brix model, except for the parameter of v_p. Scan duration down to 231 sec seemed to be sufficient for use in Tofts and Kermode. If Brix model is employed, reduced scan duration created increased curve fitting failure and significant change in the estimated parameters.

4.1 Introduction

In this chapter, factors related to the analysis process of DCE-MRI were investigated. The Arterial Input Function (AIF), which is an important component in the DCE-MRI parameter estimation, was examined for the effect on parameter estimation by: 1) the use of the left and right neck artery for extraction of AIF; 2) the use of population-averaged AIF versus individual-AIF; and 3) random noise and systematic error in the AIF. These issues have been scarcely examined in the head and neck region (Dave et al., 2009), and the results are expected to be instructive for subsequent analysis process of DCE-MRI.

This chapter also demonstrated the effect on the omission of the plasma contribution to the overall contrast concentration in the Tofts and Kermode model. Mathematically the plasma contribution is represented by the contrast concentration in the plasma compartment multiplied by the plasma volume fraction ($C_p \times v_p$). The omission of such contribution was actually proposed in the original Tofts and Kermode model, since it was assumed that the vascular compartment was relatively small and could be neglected in most situations. In addition, the result from the previous chapter showed that v_p is highly sensitive to noise, and thus showed a limited reliability for clinical use. Despite this, the omission of this term in the

parameter estimation process may result in biased estimation of the other two DCE-MRI parameter of the model, namely the k_{trans} and v_e. The results presented in this chapter aims to demonstrate the effect.

The final section of this chapter illustrates the assessment of reproducibility for the DCE-MRI parameters. This serves as an indicator for the quality of the DCE-MRI parameter generated in the studies of this thesis.

4.2 Data Acquisition Protocol

The data acquisition protocol is derived from the results of the previous chapter. The protocol is used in the study of this chapter, as well as the subsequent clinical studies described in chapter 5-7. Patients were scanned in a 1.5T MR scanner (Philips Medical System, Best, the Netherlands) with the head and neck SENSE coil. Four 3D T1-weighted gradient echo images were performed with different flip angles to generate the T1 map (repetition time, TR = 2.7 ms; echo time, TE = 0.9 ms; flip angle, α = 2, 10, 20, 30°; slice thickness, TH = 4 mm; matrix size = 128 x 128; field of view, FOV = 230 mm; number of acquisitions, NSA = 4). Dynamic gradient echo images were then acquired at a time resolution of 3.5 s for 106 time points (repetition time, TR = 2.7 ms; echo time, TE = 0.9 ms; flip angle, α = 20°; slice thickness, TH = 4 mm; matrix size = 128 x 128; FOV = 230 mm; number of acquisitions, NSA = 1). The imaged volume extends from the superior border of sphenoid sinus to cervical

C4 level.

The contrast agent (Dotarem Gd-DOTA, Guerbet, Paris, France) at a dose of 0.2 ml/kg was injected intravenously with a power injector at a rate of 3 ml/s, which commenced at 20 sec after the start of the dynamic sequence. Saline was used to flush the contrast agent at the end of the injection to ensure that all contrast agents were delivered. The injection speed was chosen to be practically repeatable with sufficient temporal resolution to capture the rising slope of enhancement.

4.3 Image Analysis Protocol

By the use of the acquired data, T1 estimation and contrast concentration derivation are performed as described in chapter 3. Besides the lesion and organ of interest, the left and right carotid arteries (either internal carotid or common carotid, depending on the location of the tumor and image coverage) were contoured. These arteries are important sources of oxygenated blood for head and neck tumors (Bailey, Johnson, Newlands, 2006), and should be able to represent the influx of contrast into the tumor. For each contoured artery, the ROI occupied a volume of 141mm^3, corresponding to one hundred pixels within the artery. The averaged contrast concentration curve within this ROI was taken to represent the AIF. A consistent ROI size was adopted, and a single researcher contoured the AIF to ensure consistency. AIFs that did not match the following criteria were considered

artifact-prone: 1. No well defined first and second pass peak, or 2. Presence of significantly abnormal spikes or troughs in the contrast concentration curve. These AIFs were excluded from the analysis.

4.4 Arterial Input Function

4.4.1 Introduction

Arterial Input Function (AIF) is an important technical component in the analysis process of DCE-MRI. AIF is the functional representation of the contrast concentration from the blood supply for the area of interest. It serves as the input function for the contrast dynamic models to generate the DCE-MRI parameters, and is also used to normalize and compensate for the variation in contrast input to the tissue of interest. These variations are caused by differences in injection timing, injected contrast dose, kidney function and cardiac output of patients. Adequate signal, image coverage, temporal and spatial resolution are prerequisites for AIF of good precision and accuracy. While these attributes cannot be maximized under the condition of limited signal, a compromise has to be made. Cheng (2008) performed a simulation study and showed that an accurate, high temporal resolution AIF is essential for the estimation of v_p in the Tofts and Kermode model. However he also stated that bi-exponentially-fitted AIF with compromised temporal resolution may be sufficient for v_e estimation with an underestimation in k_{trans}. Therefore, an optimal

AIF depends on the method of generation and also the aim for the DCE-MRI model.

Efforts were made in the past by researchers to obtain simple and reliable AIFs to reflect the true blood supply to the tissue of interest. Early pharmacokinetic models used simple mathematical functions to represent the AIF. The initial Tofts' model (Tofts and Kermode, 1991) used bi-exponential function to simulate AIF. The benefit of such method is the simplicity and regularity of the function. However, it fails to accurately represent the initial rapid surge of contrast in blood flow. Also, the cardiac variation between patients has not been adequately addressed. A number of other solutions have been proposed to tackle the problem, including the use of reference tissue method (Yang, Karczmar, Medved, et al., 2009), and other mathematical functions that attempted to provide adequate representation of the patient specific AIF (Lavini and Verhoeff., 2010).

Despite these efforts, most studies used AIFs that were directly measured from patients. Some other researchers have advocated the use of individual-AIF or population-averaged AIF. The former strategy suggests that patient-to-patient variation was substantial and AIF should be taken from individual scans to better represent the arterial supply. The later strategy recommends a population-averaged AIF to simplify data processing workflow. Population-averaged AIF may also be less susceptible to measurement error, which is usually a problem in the measurement of arterial blood supply due to the presence of fluid turbulence and flow effect. The use

of population-averaged AIF may thus improve reliability of the DCE-MRI parameters. Dave et al (2009) reported a study on the use of population-averaged AIF versus individual-AIF in the DCE-MRI of neck node metastasis. Although they did not show any significant difference between the parameters determined by each method, over 10% differences between the parameters were observed. Calamante et al (2000) suggested that the closer the AIF was to the true arterial supply, the more accurate will be for the dynamic modeling. However, the closer the AIF is to the imminent blood supply, the narrower will be the vessel, and then the problem of partial volume effect comes into play. In summary, the choice on the use of population-averaged AIF or individual-AIF is unsettled for DCE-MRI in the head and neck region.

The issue of AIF is unique in the head and neck region due to the small size and large number of feeding vessels to the region of interest. The carotid artery is the major blood supply in this region. The size and location of the artery allows for a convenient and relatively reliable source of AIF extraction. The branch ipsilateral to the tumor or organ of interest is commonly chosen to extract the AIF. However, midline-crossing tumors may be supplied by the artery on both sides. AIF extracted on the two sides may be different due to obstruction of unilateral vessels by malignancies, rendering the DCE-MRI results unreliability. There is a lack of evidence to demonstrate the similarity of the AIF extracted from either side of the

neck in patients with head and neck cancer. In short, publications on AIF in this region are very limited. A number of issues regarding AIF in the head and neck region were identified and examined in the subsequent sections: the effect of using bilateral artery for the AIF; and the effect of using population-averaged AIF versus individual-AIF for data processing. Finally, the effect of random noise and systematic error in the AIF on DCE-MRI parameters was demonstrated by mathematical simulation.

4.4.2 Difference between Bilateral AIF

4.4.2.1 Method

To examine the difference in the left and right carotid artery in DCE-MRI, ten patients with nasopharyngeal carcinoma were scanned with acquisition protocol described in section 4.2. LT-AIF and RT-AIF were obtained for each patient scan by contouring the left and right carotid artery at the same level of the cervical neck. The area under curve for the initial 60 and 90 seconds of the AIF (AUC60AIF and AUC90AIF) were recorded and compared between LT-AIF and RT-AIF for each patient. Mathematical correlation was conducted between the pairs of AIF to examine the similarity of LT-AIF and RT-AIF for each patient.

4.4.2.2 Results

Of the 21 patients scanned, 3 were excluded due to the presence of artifact. The mean difference in AUC60AIF and AUC90AIF between the LT-AIF and RT-AIF were 12.1 ± 9.3% and 10.3 ± 8.2% respectively. Correlation between the pairs of AIF is 0.979 ± 0.023. AIF taken in the carotid artery on either side of the neck region were similar. AIF could be extracted on either side where artifact was not present or the vessel was not distorted by nearby lesion.

4.4.3 Study on the Use of Population-Averaged AIF versus Individual-AIF

4.4.3.1 Method

A population-averaged AIF was obtained from 73 scans of patients with head and neck cancer. AIFs on the left and right carotid arteries for all of these scans were extracted, and a total of 146 AIFs were obtained. Twenty-eight AIFs were identified to be contaminated by artifact, and thus a total of 118 AIFs remained. These AIFs were summed together for each time points and then divided by 118, thus the population-averaged AIF was obtained. On the other hand, ten patients with nasopharyngeal carcinoma were scanned with the protocol twice (2 weeks apart) before treatment. AIFs were extracted from the 20 scans, and these AIFs were termed individual-AIFs. DCE-MRI parameters for the parotid glands were generated with the population-averaged AIF and the individual-AIF. The reproducibility of the

DCE-MRI parameters, which described the expected difference in the parameters estimated between the two scans, was assessed. Mathematical expression of the reproducibility was given in section 3.2.5.1 in Chapter 3. The mean difference between the pairs of parameters (generated by population-averaged AIF and the individual-AIF) was also examined. Test for significance of difference in the parameters generated by these two methods were conducted by pair-wise t-test.

4.4.3.2 Results

The population-averaged AIF is shown in Figure 4.1.

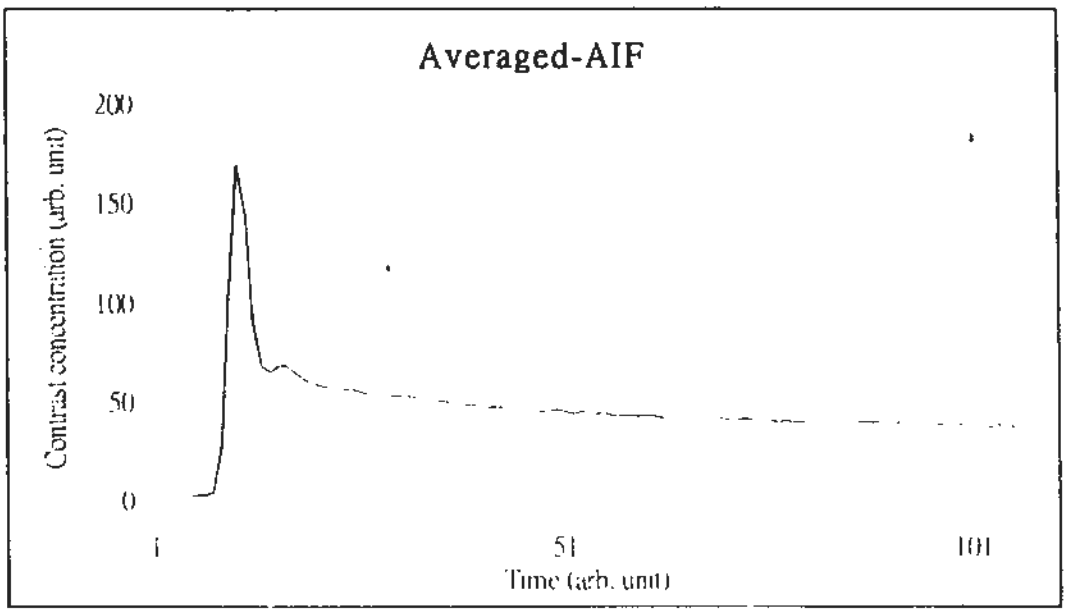

Figure 4.1: Population-averaged AIF.

The reproducibility for the DCE-MRI parameters, generated by population-averaged AIF and individual-AIF, is shown in Table 4.1. Difference in the parameters generated by population-averaged AIF and the individual-AIF is

shown in Table 4.2. Pair-wise t-test showed no significant difference ($p > 0.05$) in all parameters generated by the two AIFs.

	Individual-AIF	Population-averaged AIF
k_{trans}	± 66%	± 91.1%
v_e	± 58%	± 81.2%
v_p	± 86%	± 168.1%
AUC60	± 53%	± 90.3%
AUC90	± 53%	± 86.7%

Table 4.1: Reproducibility of the DCE-MRI parameters for the parotid glands.

Parameters	Mean ± s.d.	Maximum difference
k_{trans}	6.1 ± 26.6%	47.8%
v_e	6.8 ± 17.8%	35.5%
v_p	20.6 ± 50.3%	142.9%
AUC60/90	16.7 ± 12.8%	40.1%

Table 4.2: Difference in the DCE-MRI parameters for the parotid glands generated by using population-averaged AIF and individual-AIF.

Results showed that the use of population-averaged AIF degraded the

reproducibility of the DCE-MRI parameters as compared to the use of individual-AIF. Differences induced in the DCE-MRI parameters, by the use of population-averaged AIF as opposed to that of individual-AIF, were about 6 - 21% on average. The results suggested that individual-AIF is favorable in terms of reproducibility of the estimated parameters. Use of population-averaged AIF should also be cautious in view of the potential error induced in the DCE-MRI parameters estimated by this method.

4.4.4 Effect of Random Noise and Systematic Error in the AIF

4.4.4.1 Method

Monte Carlo simulation by the use of software written in Interactive Data Language (IDL, Boulder, CO, USA), was carried out to examine the effect on the reproducibility of DCE-MRI parameters by random noise and systematic error in the AIF. It was assumed that two major types of errors exist in AIF, namely random and systematic error. Random error refers to the random noise observed in images, and magnitude of such error depends on pulse sequences, scanner hardware, volume of ROI, etc. Systematic error can be caused by artifact, and in the case of AIF, this error is contributed in a large part by partial volume effect due to the small size of the vessels where the AIF is extracted.

The simulation involved a 'standard' contrast concentration curve for head and

neck lesions, which was constructed mathematically by incorporating typical DCE-MRI parameters into the Tofts and Kermode model. The population-averaged AIF obtained in section 4.3 was used as a standard AIF, in which random noise and systemic error were added to simulate error-contaminated AIF. The magnitude of the added random noise was chosen to yield SNR at the peak of enhancement to be 5, 10, 20, 30 and 50, and these were the level of noise typically encountered in the images of this study. Systematic error in AIF, which simulated the partial volume effect, was mimicked by reducing the overall magnitude of contrast concentration curve by 15% and 30%. One thousand simulated AIFs were generated for Monte Carlo simulation in each combination of random noise and systematic error. Curve fitting for parameter estimation was conducted with the use of these simulated AIF. The statistics of the estimated parameters was then used to calculate the reproducibility.

4.4.4.2 Results

The results of the Monte Carlo simulations, expressed in terms of reproducibility of the generated parameters, are shown in Figure 4.2. Lower reproducibility represents less variation and this better quality of the derived parameters.

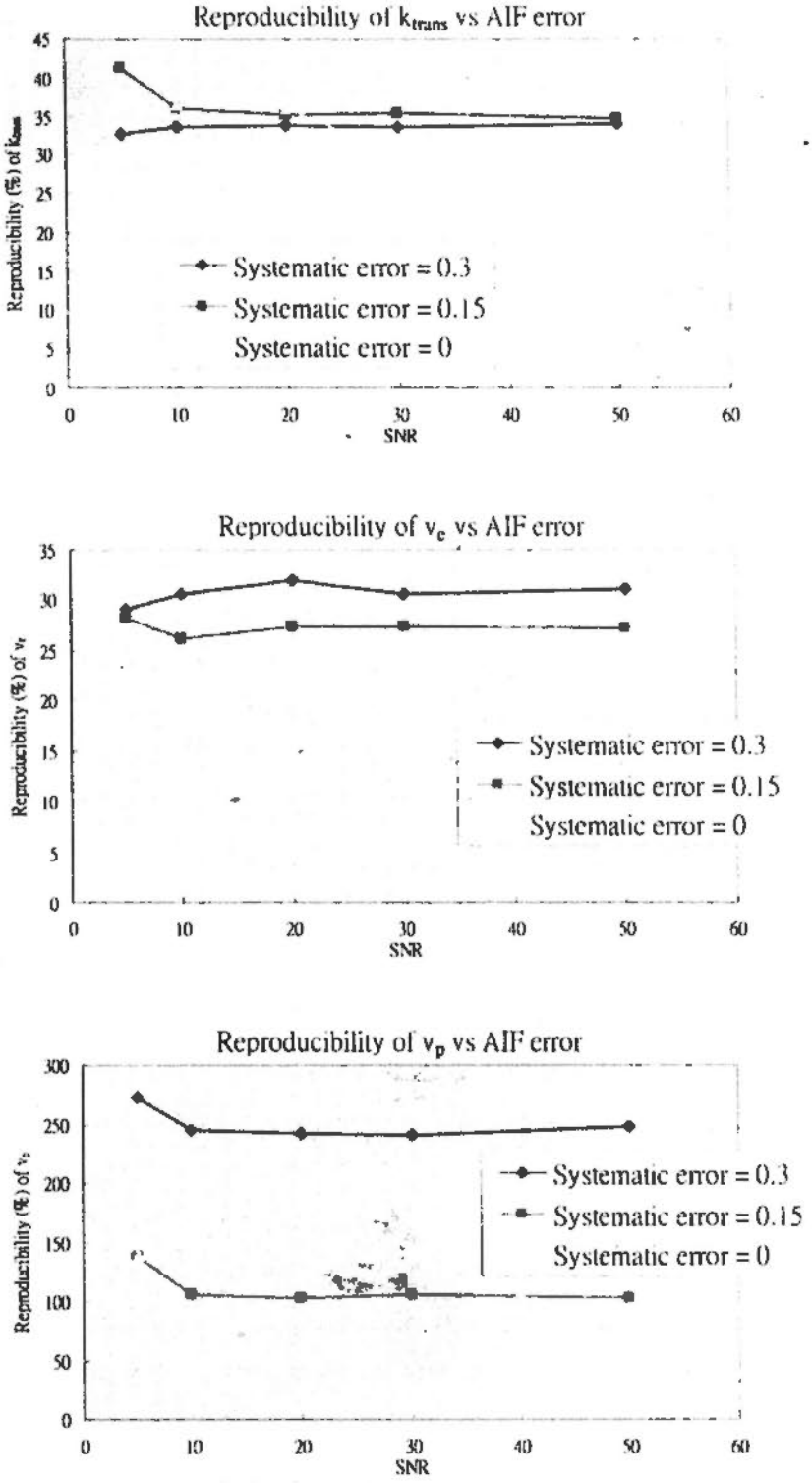

Figure 4.2: Monte Carlo simulation results for reproducibility of k_{trans}, v_e and v_p.

Simulation results showed that random error affected more substantially the reproducibility of k_{trans} than the systematic error, while the reverse is true for v_e and v_p. In practice, this implied that if k_{trans} is the primary objective of the analysis,

random noise should be reduced in the images. This could be achieved by using AIFs obtained from a larger ROI, or other means to enhance the arterial input signal. On the other hand, if v_e and v_p were the primary objectives, sources of systematic error in AIF may need to be reduced. This could be achieved by selecting voxels at the center of the artery for the AIF, instead of on the rim of vessels to reduce the partial volume effect.

4.4.5 Summary

AIF is important in DCE-MRI processing, and is necessary to cater for the variation in the contrast input and generate reproducibility results. Results shown in this thesis suggested that bilateral AIF are not different, thus the left and right carotid arteries could be used for DCE-MRI processing. Individual-AIF was preferred over population-averaged AIF in terms of reproducibility of the estimated parameters. Finally, both random noise and systematic error in AIF affected the DCE-MRI, and their relative importance depended on the DCE-MRI parameters that were used.

Very few previous publications have reported on the above issues, except for several that have studied the difference between population-averaged AIF and individual-AIF. The results shown in this study demonstrated a difference of 6-21% between the DCE-MRI parameters estimated by the use of population-averaged AIF and individual AIF. This is in accordance to the results reported by Dave et al (2009).

Pair-wise t-test showed that the difference, however, were not significant. This also agreed with the reports by Dave et al (2009) and Wang et al. (2008). However, results in this study suggested that reproducibility of DCE-MRI parameters was degraded by the use of population-averaged AIF. This is in contrary to that suggested by Parker et al. (2006). There are a number of differences between the two studies, which may contribute to the discrepancy in result. Firstly, the region of interest in the study by Parker et al. is the abdominal and pelvic region, and respiratory motion is substantial in this part of the body. Population-averaged AIFs may alleviate this problem while motion artifact may contaminate the individual AIF. Secondly, the semi-automatic extraction of AIF depicted in Parker's study may increase the variation of the AIFs collected, thus contributing to the comparatively higher variation in the estimated DCE-MRI parameter generated by the individual-AIF. The present result suggests the advantage of individual-AIF over population averaged-AIF. This may generally be explained by the high complexity of blood flow in the head and neck region, rendering considerable variation in blood supply between patients and between scans. Such variations are catered by AIF obtained from individual scans.

4.5 Inclusion of the Vascular Contribution for Total Contrast Concentration in Tofts and Kermode Model

4.5.1 Method

Values of k_{trans}, v_e and v_p typical for head and neck lesions were fitted into the expression by Tofts and Kermode model to reconstruct contrast concentration curves. Three values, representing the lower, medium and higher range of each parameter were chosen to demonstrate the effect at these scenarios. The values assigned to k_{trans} are (low: 0.6 min^{-1}, medium: 0.8 min^{-1}, high: 1.2 min^{-1}), v_e (low: 0.4, medium: 0.5, high: 0.6), v_p (low: 0.05, medium: 0.075, high: 0.1). Twenty-seven combinations were thus generated. Gaussian noise was added to the 27 simulated curves and parameter estimation was conducted in similar fashion to the above sessions. The error of the estimated parameters, as compared to the originally assigned values, was obtained. The error for each curve fitting in arbitrary unit was also recorded.

4.5.2 Results and Discussions

k_{trans}	v_e	v_p	Error (est. k_{trans})	Error (est. v_e)	Fit error
Low	Low	Low	27.6%	7.2%	0.306
		Medium	36.7%	11.7%	0.312
		High	53.1%	16.7%	0.323
Low	Medium	Low	25.9%	4%	0.314

		Medium	31.1%	7.8%	0.317
		High	31.5%	11.6%	0.330
Low	High	Low	20.6%	3.4%	0.327
		Medium	31.1%	5.3%	0.327
		High	31.1%	8.5%	0.336
Medium	Low	Low	19%	6.9%	0.302
		Medium	33.5%	11%	0.307
		High	46.2%	16.9%	0.313
Medium	Medium	Low	14.3%	4.5%	0.304
		Medium	39.1%	7.1%	0.329
		High	33.9%	4.5%	0.345
Medium	High	Low	13%	3.4%	0.309
		Medium	20.5%	6.3%	0.314
		High	23.6%	9.2%	0.325
High	Low	Low	17.6%	6.2%	0.301
		Medium	30.2%	10%	0.304
		High	40.0%	14.5%	0.308
High	Medium	Low	15.4%	3.0%	0.327
		Medium	50.4%	4.0%	0.333

		High	43.1%	9.3%	0.326
High	High	Low	10.4%	3.4%	0.304
		Medium	16.7%	6.3%	0.310
		High	34.9%	7.8%	0.330

Table 4.3: Error of parameter estimation for each simulation and the curve fit error.

Omission of the term $C_p v_p$ in the curve fitting induced error of up to 53.1% in k_{trans}. Error in the estimated v_e may exceed 10%. The error increased with higher values of v_p, or lower values of k_{trans} or v_e. Curve fitting error is higher with higher values of v_p. In summary, omission of $v_p C_p$ in the estimation expression induced substantial error in k_{trans} estimation, and also induced increased error in curve fitting for scenario in the head and neck lesions.

4.6 General Assessment on the Reliability of DCE-MRI Parameters

4.6.1 Method

Reproducibility is an important attribute to describe the reliability of the DCE-MRI data. It is also a general indicator on the quality of the DCE-MRI processing. Parameters that are reproducible improve the clinical usefulness of the data, which stems from the fact that small changes are detectable that may represent

therapeutic effect, or a difference in the vascular properties of the lesions. Reproducibility studies and parameters used to describe the attributes were summarized in published papers (Laking, West, Buckley, et al., 2006; Marcus, Marcus, Cucu, et al., 2009).

The reproducibility of tumors and the parotid glands were assessed. A total of 5 lesions were included. The lesions were scanned twice at 2 weeks apart before treatment. In addition, 20 parotid glands from 10 nasopharyngeal carcinoma patients were scanned at 2 weeks apart before chemoradiation treatment.

4.6.2 Results and Discussions

The results of the study are shown in Table 4.4 and 4.5.

Parameters	wCV	Reproducibility
k_{trans}	± 14% (± 0.244 min^{-1})	± 39% (± 0.676 min^{-1})
v_e	± 5% (± 0.028)	± 14% (± 0.078)
v_p	± 23% (± 0.040)	± 63% (± 0.111)
A	± 11% (± 4.258)	± 30% (± 11.795)
k_{el}	± 23% (± 0.107 sec^{-1})	± 64% (± 0.296 sec^{-1})
k_{21}	± 6% (± 0.012sec^{-1})	± 17% (± 0.033 sec^{-1})
AUC60	± 12% (± 0.046)	± 33% (± 0.127)

AUC90	± 15% (± 0.131)	± 42% (± 0.363)

Table 4.4: Reproducibility result for head and neck lesions.

Parameters	wCV	Reproducibility
k_{trans}	± 24% (± 0.220 min^{-1})	± 66% (± 0.594 min^{-1})
v_c	± 21% (± 0.081)	± 58% (± 0.224)
v_p	± 31% (± 0.012)	± 86% (± 0.033)
A	± 23% (± 8.8)	-44 to +78% (-16.697 to +29.707)
k_{el}	± 39% (± 0.245 sec^{-1})	-60 to +149% (-0.375 to +0.933 sec^{-1})
k_{21}	± 14% (± 0.037 sec^{-1})	-31 to +43.9% (-0.081 to +0.116 sec^{-1})
AUC60	± 19% (± 0.048)	± 53% (± 0.133)
AUC90	± 19% (± 0.110)	± 53% (± 0.305)

Table 4.5: Reproducibility result for the parotid glands.

Reproducibility results of DCE-MRI in head and neck lesions reported in this thesis is comparable to those values of other tumors obtained by Galbraith et al (2002) and Roberts et al (2006). Results for parotid glands are comparable to those obtained from muscles in the same report, and also similar to the results on normal muscles and fat from Padhani et al (2002) and results on normal muscles by Eveloch et al (2004). Technically, DCE-MRI parameters generated from pharmacokinetic models

showed comparable reproducibility with those parameters generated from model-free analysis (e.g. AUC60 and AUC90). The former is more complex and computationally intensive than the later. However, it provides better physiological meaning, in accord with the suggestions from Roberts et al (2006).

4.7 Conclusion

Results shown in this chapter on AIF suggested that 1) bilateral AIF were not different, thus the left and right carotid arteries could be used for DCE-MRI processing; 2) Individual-AIF was preferred over population-averaged AIF in terms of reproducibility of the estimated parameters; 3) both random noise and systematic error in AIF affected the DCE-MRI, and their relative importance depended on the DCE-MRI parameters that were used.

The second part of this chapter showed that omission of the term $C_p v_p$ in the curve fitting induced error of up to 53.1% in k_{trans}. Error in the estimated v_e may exceed 10%. The error increased with higher values of v_p, or lower values of k_{trans} or v_e. Curve fitting error was higher with higher values of v_p. The effect of omitting $v_p C_p$ in the estimation expression is thus substantial in the head and neck lesions.

The reproducibility of the DCE-MRI parameters generated in the studies of this thesis was comparable to those reported in other literatures. This guaranteed the quality of the data and the processing in these studies.

CHAPTER 5 - DCE-MRI TO DIFFERENTIATE HEAD AND NECK MALIGNANCIES

5.1 Introduction

Head and neck cancer most commonly originates from the upper aerodigestive tract, including the lip, oral cavity, nasal cavity, paranasal sinuses, pharynx, and larynx. The majority of head and neck cancers are squamous cell carcinomas (HNSCC), originating from the mucosal lining of the head and neck region. Different types of head and neck tumors are characterized by the originating anatomical site, and also the originating cell type. Tumor types differ in their clinical presentation, prognosis, treatment outcome and available treatment options. Therefore, characterization of tumors helps to guide selection of treatment and predict survival.

Malignant tumors in the head and neck region are diagnosed by physical and radiological examinations, panendoscopy, and are usually confirmed by biopsy. Functional imaging offers a non-invasive method to provide physiological information to characterize the primary tumor. A number of functional imaging techniques were under investigation for use in head and neck cancers. Diffusion weighted MR imaging (DWI) has been used to differentiate different tumor types in the head and neck region (Fong, Bhatia, Yeung, et al., 2010). Positron emission tomography (PET) with the use of different tracers is used to assess tumor hypoxia

(Nehmeh, Lee, Schroder, et al., 2008) and tumor cell proliferation (Menda, Ponto, Dornfeld, et al., 2009) in head and neck cancer. Besides providing further information on the tumor physiology, these imaging techniques are also means to guide selection and development of future targeted treatment drugs.

DCE-MRI is potential candidate of functional imaging to provide benefit in the management of head and neck cancers. There are a number of published reports on DCE-MRI of head and neck lesions with qualitative analysis (Escott, Rao, Ko, et al., 1997; Tezelman, Giles, Tunca, et al., 2007; Alibek, Zenk, Bozzato, et al., 2007; Baba, Furusawa, Murakami, et al., 1997; Hisatomi, Asaumi, Konouchi, et al., 2002). These reports investigated the shape of dynamic contrast enhancement curve for diagnostic purpose. Other reports on analysis of enhancement curve, such as the use of enhancement ratio and slope (Hoskin, Saunders, Goodchild, et al., 1999; Asaumi, Yanagi, Konouchi, et al., 2004; Asaumi, Yanagi, Hisatomi, et al., 2003; Fischbein, Noworolski, Henry, et al., 2003; Noworolski, Fischbein, Kaplan, et al., 2003; Konouchi, Asaumi, Yanagi, et al., 2003; Baba, Yamashita, Onomichi, et al., 1999; Gückel, Schnabel, Deimling, et al., 1996; Oysu, Ayanoglu, Kodalli, et al., 2005; Tomura, Omachi, Sakuma, et al., 2005; Ariyoshi and Shimahara, 2006; Hisatomi, Asaumi, Yanagi, et al., 2007) characterized tumors in a more quantitative manner. In general, tumors that demonstrated high enhancement ratio and slope corresponded to vascular and active tumor and these tumors responded better to treatment because of

better perfusion and less hypoxic and necrotic regions. In comparison, pharmacokinetic modeling of the tracer kinetics, which generates DCE-MRI parameters with a better defined physiological meaning have not been reported as extensively in the head and neck (Kim, Quon, Loevner, et al., 2007; Machiels, Henry, Zanetta, et al., 2010; Jansen, Schöder, Lee, et al., 2009; Shukla-Dave, Lee and Stambuk, 2009), and has not been reported in relationship to the characterization of different tumors.

The study investigated the use of DCE-MRI in head and neck cancers for differential diagnosis of three histological types of head and neck cancers: squamous cell carcinoma (SCC), undifferentiated carcinoma (UD) and lymphoma. These three tumors differ in tumor aggressiveness and response to radiotherapy both of which are factors shown to be influenced by tumor vascularity. Therefore, it was believed that differences may be found in the DCE-MRI parameters amongst these types of tumors. Data were analyzed by the use of area under curve (AUC) of contrast concentration, and the pharmacokinetic models proposed by Tofts and Kermode (1991) and Brix (1991).

DCE-MRI parameters parameters potentially useful for differentiation of tumor types were identified. Heterogeneity of these parameters within the lesions was analyzed by the use of histogram analysis.

The DCE-MRI parameters were tested for significant difference amongst the

three types of lesion. These parameters were examined with Receiver Operator Characteristics (ROC) curve analysis to calculate the sensitivity and specificity for differentiating one type of lesion against the others.

5.2 Methods

5.2.1 Patients and Data Acqusition

63 patients with histological proven malignant head and neck lesions, with 26 undifferentiated carcinomas (all nasopharyngeal region), 28 squamous cell carcinomas (10 hypopharynx, 10 tonsil, 2 retromolar trigone, 2 oesophageal, 1 supraglottic , 1 larynx, 1 nasal cavity, 1 maxillary sinus) and 8 lymphomas (1 parotid, 1 maxilla, 2 tonsil, 1 tongue base, 2 nasopharyngeal, 1 oral cavity; 6 low grade and 2 high grade) underwent DCE-MRI scanning at the time of their staging MRI examination. The local research ethics committee approved the study, and patients were entered in the study after informed consent. Patients were scanned in a 1.5T MR scanner (Philips Medical System, Best, the Netherlands) with the head and neck SENSE coil. Four 3D T1-weighted gradient echo images were performed with different flip angles to generate the T1 map (repetition time, TR = 2.7 ms; echo time, TE = 0.9 ms; flip angle, α = 2, 10, 20, 30°; slice thickness, TH = 4 mm; matrix size = 128 x 128; field of view, FOV = 230 mm; number of acquisitions, NSA = 4). Dynamic gradient echo images were then acquired at a time resolution of 3.5 s for

106 time points (repetition time, TR = 2.7 ms; echo time, TE = 0.9 ms; flip angle, α = 20°; slice thickness, TH = 4 mm; matrix size = 128 x 128; FOV = 230 mm; number of acquisitions, NSA = 1). The imaged volume extends from the superior border of sphenoid sinus to cervical C4 level.

The contrast agent (Dotarem Gd-DOTA, Guerbet, Paris, France) at a dose of 0.2 ml/kg was injected intravenously with a power injector at a rate of 3 ml/s, which commenced at 20 s after the start of the dynamic sequence. Saline was used to flush the contrast agent at the end of the injection to ensure that all contrast agents were delivered. The injection speed was chosen to be repeatable with sufficient temporal resolution to capture the rising slope of enhancement.

To reduce motion artifact, patients were reminded not to swallow during scanning time. Motion of the patients during scan was monitored and corrected if necessary. Images with substantial artifacts were excluded.

5.2.2 Data processing

A number of processing steps are involved to generate the DCE-MRI after data acquisition.

5.2.2.1 Visual Inspection of Images

Visual inspection is a simple and reliable means to identify image artifacts.

Common artifacts that can easily be identified are motion artifact and pulsation artifact. Images with significant artifact at the area of interest were discarded.

5.2.2.2 Image Alignment

Misaligned images are aligned by the use of SPM software provided by the Wellcome Trust Center for Neuroimaging in the United Kingdom, with non-deformable affine registration. The alignment process was intended to correct for patient motion between the scans. The 6 correctable dimensions of an affine 'rigid-body' transformation are: transformation in the x, y and z direction, roll, yaw and pitch. The image alignment software minimizes the sum of squared differences between the scans and the necessary corrections were determined. Image alignment was implemented accordingly.

In the neck region, patients may swallow during scans. This may affect areas around the laryngeal region or airway that renders significant misalignment for nearby tumors or organs of interest. This type of image misalignment is termed non-rigid deformation. At present, reliable non-rigid registration software is not available to rectify swallowing distortions. Instructions were given to patient to avoid swallowing during the scans. Otherwise, if the induced misalignment was serious and uncorrectable, the images were discarded.

5.2.2.3 Contouring

Primary tumors were contoured on the T1-weighted post contrast images. An experienced radiologist contoured the primary tumor of each patient. The contours were than manually transferred to the spoiled gradient echo images for processing, based on the references from the T1 weighted images. For consistency, contouring was performed by a single radiologist. The left and right carotid arteries (either internal carotid or common carotid, depending on the location of the tumor and image coverage) were contoured. These arteries are important source of oxygenated blood for head and neck tumors (Bailey, Johnson, Newlands, 2006), and should be able to represent the influx of contrast into the tumor. The contoured artery is used to generate the AIF for subsequent DCE-MRI processing. Finally, the parotid glands on both sides of several patients were contoured for the clinical study described in subsequent chapter.

5.2.2.4 T1 Map Generation

T1 was estimated pixel by pixel by the 4 spoiled gradient echo images using the Bloch formula. Equation [5.1] described the relationship between signal intensity and the T1 for spoiled gradient echo sequence at steady state (Bernstein, King, Zhou, 2004).

$$S = K \cdot \rho \cdot \frac{\sin(\alpha) \cdot \left(1 - e^{-\frac{TR}{T1}}\right)}{1 - \cos(\alpha) e^{-\frac{TR}{T1}}} \cdot e^{-\frac{TE}{T2}} \qquad [5.1]$$

Where S is the signal intensity, K represents a constant related to the receiver gain and other scanner specific parameters, ρ is the proton density, TR is the repetition time, T1, α is the flip angle, TE is the echo time. The T1 estimation algorithm was implemented using IDL (Interactive Data Language, RSI, Boulder, CO, USA). T1 map for the field of view was determined.

5.2.2.5 Contrast Concentration Curve Derivation

Using the derived T1, the signal intensity-time curve for each pixel was transformed into contrast concentration-time curve. Contrast agents are known to alter the spin-spin relaxation rates of tissues, and thus induce a change in T1. The relationship of T1 and contrast concentration is shown in equation [5.2].

$$C = \frac{T_{10} - T_1}{R_{el} T_{10} T_1} \qquad [5.2]$$

The relaxivity constant R_{el} was taken as 4.39/s/mM. C is the contrast concentration, T1 is the tissue T1 value at the presence of contrast, $T1_0$ is the baseline tissue T1.

5.2.2.6 DCE-MRI Parameter Estimation

The resultant contrast concentration dynamic curve for each pixel was used as input for the DCE-MRI modeling, with pharmacokinetic models from Tofts and Kermode (1991) and Brix (1991). k_{trans}, v_e and v_p from the Tofts' model and A, k_{21} and k_{el} from the Brix model were estimated for every pixel using multiple starting point Marquardt-Levendag curve fitting (Ahearn, Staff, Redpath, et al., 2005). In addition, the area under the contrast concentration curve for the initial 60 seconds (AUC60), and the initial 90 seconds (AUC90) were taken. Details of the parameter estimation was described in the previous chapter, and the estimation was performed with in-house developed software implemented using IDL (Interactive Data Language, RSI, Boulder, CO, USA). The mean of these parameters were taken and compared between the different types of tumors. The parameters that yield significant difference amongst the tumors were selected for histogram analysis, which generates the mean, 25%, 50%, 75% and 95% percentile value of each lesion to characterize the heterogeneity of the lesions.

5.2.3 Statistical analysis

Kruskal-Wallis test for different DCE-MRI parameters were performed to determine parameters with significant difference ($p<0.01$) amongst the three different types of lesions. DCE-MRI parameters that showed significant differences

underwent further Receiver Operator Characteristic (ROC) analysis to determine the sensitivities and specificities with the highest degree of accuracy. Also, a cutoff value was chosen that maximized specificity while optimizing the sensitivity.

5.3 Results

The mean DCE-MRI parameters for the 3 types of tumors are shown in table 5.1.

		UD	SCC	Lymphoma
Tofts	k_{trans} (min^{-1})	1.26 ± 0.61	0.78 ± 0.47	0.59 ± 0.18
	v_e	0.65 ± 0.16	0.64 ± 0.13	0.54 ± 0.17
	v_p	0.11 ± 0.12	0.08 ± 0.06	0.07 ± 0.03
Brix	A	49.32 ± 12.07	38.92 ± 10.95	37.13 ± 6.08
	k_{el} (10^{-1}/sec)	0.39 ± 0.08	0.51 ± 0.20	0.47 ± 0.25
	k_{21}(10^{-1}/sec)	0.23 ± 0.02	0.22 ± 0.02	0.22 ± 0.02
Semi-quantitative	AUC60	0.31 ± 0.11	0.23 ± 0.10	0.21 ± 0.05
	AUC90	0.74 ± 0.28	0.54 ± 0.21	0.50 ± 0.09

Table 5.1: Mean and standard deviation of the DCE parameters for UD, SCC and lymphoma.

There were significant differences ($p < 0.01$) in the k_{trans}, AUC60 and AUC90 between UD and SCC and between UD and lymphoma, but no parameters showed a significant difference between SCC and lymphoma. The mean and the values at the 25%, 50%, 75% and 95% percentile for these DCE-MRI parameters are shown in Figure 5.1.

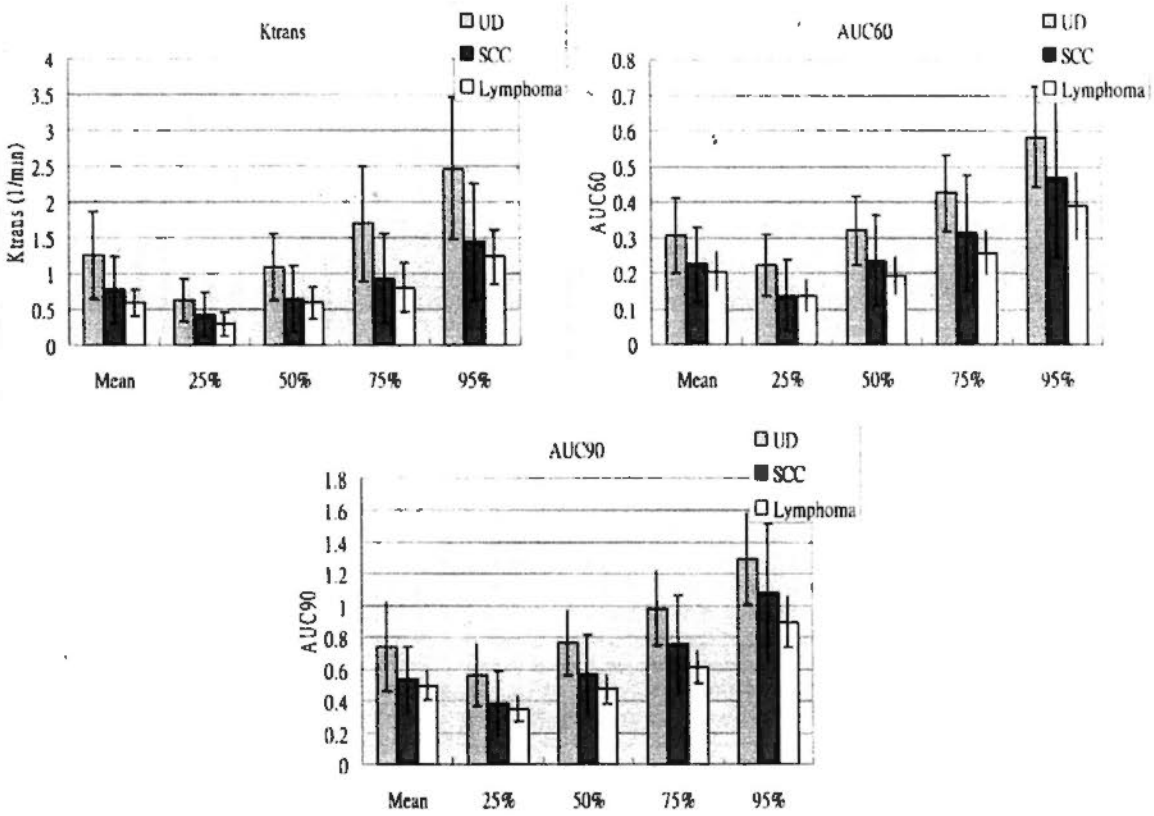

Figure 5.1: Bar charts of k_{trans}, AUC60 and AUC90 for the three types of lesions.

ROC analysis was performed and results of the parameters that demonstrated the greatest accuracy and sensitivity for differentiation of the tumors are shown in tables 5.2 and 5.3. Figure 5.2 shows the average histogram for the k_{trans}, AUC60 and AUC90 of UD, SCC and lymphoma. Sample images of the parameter maps of k_{trans}, AUC60 and AUC90 and the corresponding T1 image, are shown in Figure 5.3.

	Parameter	Accuracy	Sensitivity %	Specificity %	Cutoff value
UD/SCC	Mean AUC90	0.784	68%	88%	0.616
UD/Lymphoma	75% AUC90	0.973	100%	88.5%	0.754

Table 5.2: Parameters with the maximum accuracy for differentiation of tumors.

	Parameter	Accuracy	Sensitivity %	Specificity %	Cutoff value
UD/SCC	25% AUC60	0.695	36.7%	100%	0.071
Lymphoma/UD	75% AUC90	0.973	88.5%	100%	0.754

Table 5.3: Parameters with maximum sensitivity at 100% specificity.

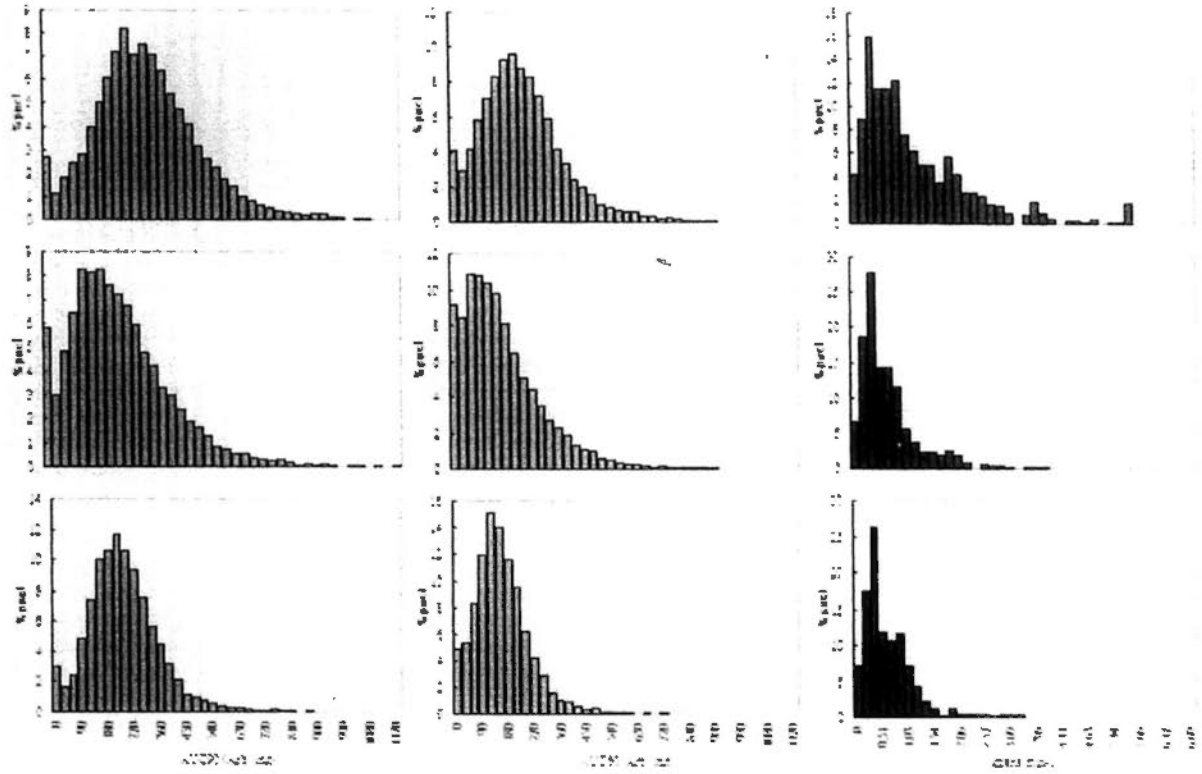

Figure 5.2: Histogram averaged over patients for each type of lesions for k_{trans}, AUC60 and AUC90.

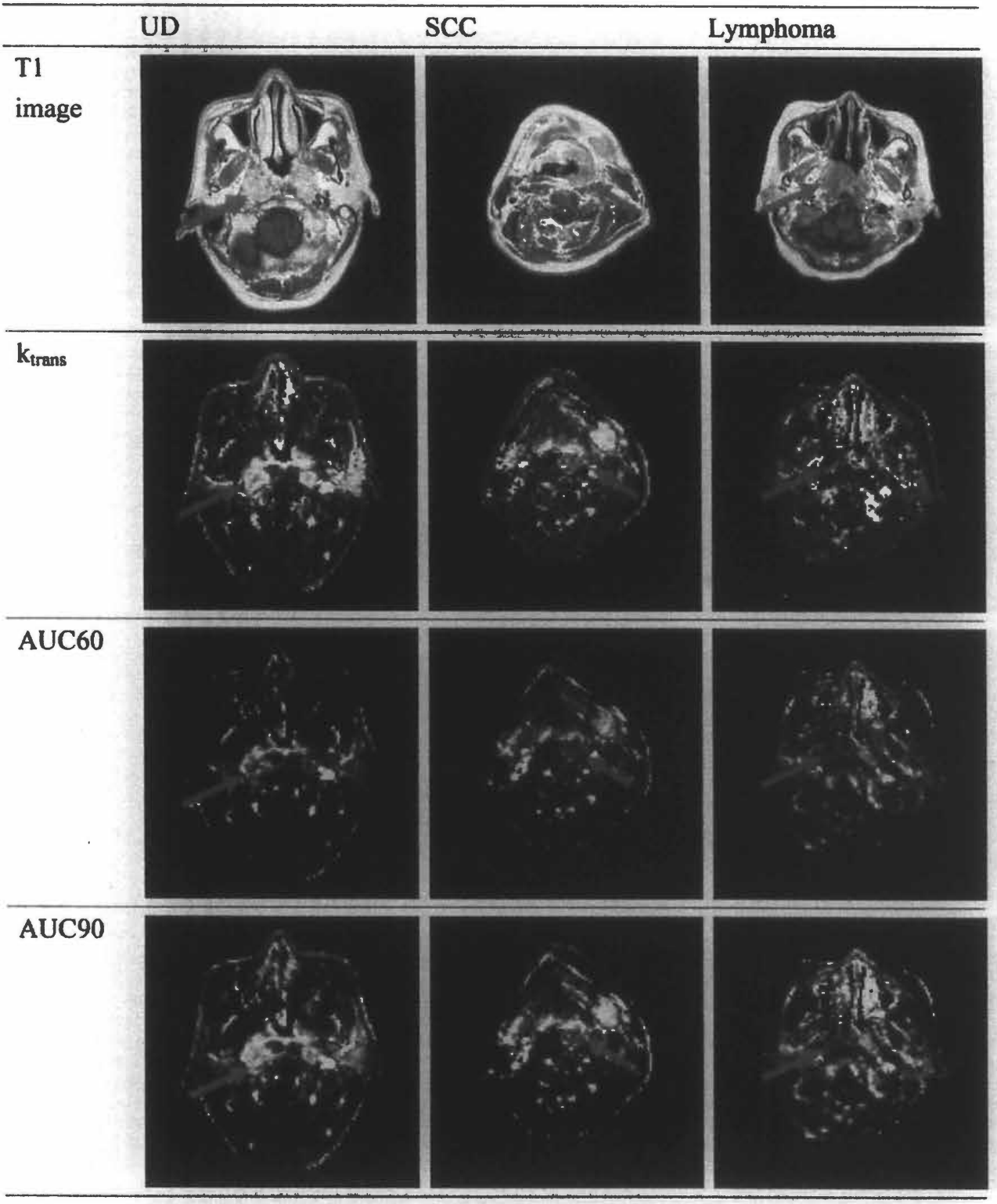

Figure 5.3: Sample images of the k_{trans}, AUC60 and AUC90 and the corresponding T1 image. Red arrow denotes the location of the lesion.

5.4 Discussion

Relatively few research studies have reported results using DCE-MRI parameters from head and neck cancers generated using pharmacokinetic models and quantitative analysis (Machiels, Henry, Zanetta, et al., 2010; Jansen, Schöder, Lee, et al., 2009; Shukla-Dave, Lee and Stambuk, 2009) and none have used the tool to distinguish between UD, SCC and lymphoma. In this study, k_{trans}, AUC60 and AUC90 showed significant differences between UD/SCC and UD/lymphoma but none of the parameters showed a significant difference between SCC/lymphoma. DCE-MRI parameters generated by the Brix model did not demonstrate significant difference amongst the lesion types, which suggested its limited potential for this application. The parameter that showed the highest accuracy was the AUC90, yielding 78% and 97% respectively for differentiation between UD/SCC and UD/lymphoma. When measuring functional parameters, tumor heterogeneity can influence the results and so methods which take into account heterogeneity in tumor vascularity, such as histogram analysis (Hayes, Padhani and Leach, 2002; Jackson, O'Connor, Parker, et al., 2007; Yuh, Mayr, Jarjoura, et al., 2009) are becoming a recognized method to assess cancers. Results from histogram analysis concur with this view, whereby using AUC90 values obtained from 75% and 25% percentile obtained results with the maximum accuracy and sensitivity.

The k_{trans} value in this study for UD was significantly higher than the other two

types of tumors. Since k_{trans} is in part related to vascular permeability, this may infer that vessels in UD have a higher permeability than the other two types of tumors. Another biomarker which is related to vascular permeability (Senger, Water, Brown, et al., 1993), is vascular endothelial growth factor (VEGF). Interestingly the rate of positive/high expression in VEGF for UD has been reported to range from 45.7-80% (Guang-Wu, Sunagawa, Li, et al., 2000; Pan, Kong, Lin, et al., 2008; Li, Hu, Qiong, et al., 2008) and the upper limit of this range for UD is greater than that of SCC (Mineta, Miura, Ogino, et al., 2000; Vipa, Boonchu, Juvady, et al., 2008; Bandoh, Hayashi, Takahara, et al., 2004; Sawatsubashi, Yamada, Fukushima, et al., 2000) (24.1-50%) or lymphoma (Gratzinger, Zhao, Marinelli, et al., 2007; Hazar, Paydas, Zorludemir, et al., 2003; Mainou-Fowler, Angus, Miller, et al., 2006 ; Gratzinger, Advani, Zhao, et al., 2010) (0-60%). The k_{trans} results therefore appear to correlate with the VEGF data.

In addition to k_{trans}, AUCs in the study were significantly higher in UD than in SCC and lymphoma and both of these parameters have been suggested as primary end points for DCE studies on anti-vascular therapies (Leach, Brindle, Evelhoch, et al., 2005). Compared to k_{trans}, AUC has no biological specificity but is rather a measure of amount of contrast delivered to and retained by tumor in a given time period. The ROC analysis reveals that AUC90 yields better accuracy and sensitivity than k_{trans} in the differentiation of tumors. This may be due to the fact that AUC is

more robust because of its relative simplicity in the process of parameter extraction. This is supported in a study by Galbraith et al (Galbraith, Lodge, Taylor, et al., 2002), which showed that AUC has a better reproducibility than k_{trans}.

Limited number of cases in the lymphoma group is the major limitation of our study. Difficulty in recruitment is the reason for such limitation. Despite the weakness, we do not expect a major difference in study outcome if more cases are recruited. There was a relatively narrow range of DCE-MRI values for lymphoma as compared to SCC in the present series. This data is likely to be reproducible with a larger sample size.

Another functional MRI technique, diffusion weighted imaging (DWI), has shown significant differences amongst all three of these cancers. Using the apparent diffusion coefficient (ADC) as the DWI biomarker (Fong, Bhatia, Yeung, et al., 2010), it was found that the ADC value of UD was in between that of lymphoma (lower ADC) and SCC (higher ADC), which is a different trend to that seen with DCE-MRI where it is SCC which has parameters that are in between UD (higher k_{trans} and AUC) and lymphoma (lower k_{trans} and AUC). For identification of cancer groups it is clinically useful to set the specificity to 100% while trying to maintain a high sensitivity and by doing so it appears that DCE and DWI produce complementary information with DCE of value in distinguishing lymphoma from UD and DWI for distinguishing lymphoma from SCC.

5.5 Summary

In this study, we analyzed the DCE-MRI data of undifferentiated carcinoma (UD), squamous cell carcinoma (SCC) and lymphoma with the use of quantitative analysis and pharmacokinetic modeling. Results identified several parameters that showed significant difference between UD/SCC and UD/lymphoma, namely k_{trans}, AUC60 and AUC90. However, no parameters showed a difference between SCC and lymphoma. The highest accuracy for DCE-MRI was obtained by taking into account tumor heterogeneity to analyze different percentile values obtained from a histogram. DCE-MRI parameters identified in this study may prove its clinical utility to assist differentiation of different types of head and neck tumors. Of all DCE-MRI parameters the AUC90 was shown to produce the highest accuracy, which would be an advantage in routine clinical practice because of its relative simplicity in the process of parameter extraction compared to the model based parameters such as k_{trans}.

Chapter 6 - Pilot Study for Early Prediction of Treatment Failure in Head and Neck Squamous Cell Carcinomas Using DCE-MRI

6.1 Introduction

Head and neck cancers are usually treated with radiotherapy or chemotherapy, or a combination of both, but treatment failures are not uncommon amongst these patients. A study (Koch, Brennan, Zahurak, et al., 1996) of 110 patients with squamous cell carcinoma in the head and neck region (HNSCC) reported 35% patients had locoregional persistent tumor or recurrent disease after treatment. Some prognostic factors, such as tumor stage, histology grade, patient age and co-morbidity helped identify patients at higher risk of treatment failure. Despite this, variation in outcome exists for patients with similar factors. Additional information from functional imaging may improve prediction of treatment outcome for individual patients. If this information is available in the early phase of treatment, it may help physicians to alter treatment, or identify patients at higher risk of treatment failure so they can undergo more intensive post–treatment monitoring.

Zahra et al (2007) published a review that summarized the articles on the use of DCE-MRI for prediction of treatment response and survival of various types of tumors. For head and neck lesions, the enhancement ratio (Oysu, Ayanoglu, Kodalli,

et al., 2005), the enhancement slope (Tomura, Omachi, Sakuma, et al., 2005) and the pretreatment k_{trans} from the Tofts and Kermode model (Kim, Loevner, Quon, et al., 2010), have shown to correlate with tumor residual and recurrence.

In this study, DCE-MRI was performed using pharmacokinetic models by Tofts and Kermode (1991) and Brix et al. (1991) and also using the contrast concentration curve to obtain area under the curve (AUC) for prediction of treatment failure in HNSCC. DCE-MRI was performed before treatment and at 2 weeks after start of chemoradiation or radiotherapy. The timing of the second scan was chosen such that it was at the early stage of treatment. Early changes in DCE-MRI parameters, which may predict treatment response, are clinically useful to guide continuation of present treatment or alternation to other more effective management scheme. Baseline pre-treatment DCE-MRI parameters and the early change in DCE-MRI parameters during the course of treatment were correlated with treatment outcome. It was expected that parameters with high correlation could potentially be useful clinically to predict treatment failure before or at an early stage of disease management. In addition, heterogeneity of the DCE-MRI parameters at the primary tumor site was analyzed. There were reports that methods which take into account spatial heterogeneity of DCE-MRI parameters, such as histogram analysis (Yuh, Mayr, Jarjoura, et al., 2009; Hayes, Padhani and Leach, 2002; Jackson, O'Connor, Parker, et al., 2007), could influence the predictive power of the DCE-MRI parameters (Rose,

Mills, O'Connor, et al., 2009).

6.2 Methods

6.2.1 Patients

Patients with primary head and neck squamous cell carcinoma (HNSCC) without prior treatment were recruited. The local research ethics committee approved the study, and patients were requested to sign the informed consent prior to the scan. These patients received chemo-radiation or radiation alone. Patients underwent regular clinical and radiological follow up after treatment. Treatment outcome at the primary site was assessed at one year with subsequent follow up, and patients were divided into the local control (LC) and local failure (LF). Local failure in the HNSCC site was determined by histological confirmation of SCC (biopsy or surgical resection) or when there was a serial increase in size on follow-up. Local control in the primary site was determined by histological confirmation (surgical resection) or by follow up for at least 1 year from the start of treatment.

6.2.2 Image Acquisition and Data Processing and DCE-MRI Parameters

DCE-MRI data was acquired and processed according to the protocol described in the chapter 5. Maps of the DCE-MRI parameters, including k_{trans}, v_e, v_p from the Tofts and Kermode model, A, k_{21}, k_{el} from the Brix model, AUC60 and AUC90 were

generated.

Baseline DCE-MRI parameters averaged for all pixels in the tumors were obtained. Histogram analysis was performed to obtain the 25%, 50%, 75% and 95% percentile value of each tumor to characterize the heterogeneity. Changes in these values between baseline and 2 weeks after start of treatment were also recorded.

6.2.3 Statistical Analysis

T-test on the baseline DCE-MRI parameters and change in DCE-MRI parameters between the local control (LC) and local failure (LF) group were conducted. $p<0.05$ was chosen as the level of confidence. Parameters that demonstrated significant difference between the two groups were used to evaluate effectiveness to predict treatment response. The cutoff value that provided the maximum sensitivity and specificity to identify local failure was determined.

6.3 Results

6.3.1 Patient

DCE-MRI was performed at 16 primary sites in 16 patients. Mean follow up period was 37.4 ± 11.0 months, range: 22-58 months. Three of the 16 (19%) patients showed local failure during the follow up period. Patient details are shown in Table 6.1.

	Local control	Local failure
Gender	11 males, 2 females	3 males
Site	5 hypopharynx, 6 tonsil, 1 larynx, 1 esophagus	2 hypopharynx, 1 oropharynx
Age	45-73	52-53

Table 6.1: Details of the recruited patients.

6.3.2 DCE-MRI Results – Baseline

The mean baseline DCE-MRI parameters are shown in Table 6.2.

	Local control	Local failure
k_{trans} (min^{-1})	0.760 ± 0.466	0.633 ± 0.283
v_e	0.606 ± 0.129	0.632 ± 0.053
v_p	0.077 ± 0.055	0.047 ± 0.011
A	43.77 ± 15.61	33.33 ± 4.16
k_{el} (10^{-2} sec^{-1})	0.22 ± 0.02	0.22 ± 0.01
k_{21}(10^{-1} sec^{-1})	0.48 ± 0.17	0.60 ± 0.23
AUC60	0.232 ± 0.101	0.191 ± 0.080
AUC90	0.531 ± 0.184	0.480 ± 0.176

Table 6.2: Mean baseline DCE-MRI parameters.

The k_{trans} from the Tofts and Kermode model, A from the Brix model, AUC60 and AUC90 were lower in the LF group than in the LC group. However, there was no significant difference in any baseline DCE-MRI parameters between the two groups using mean or 25%, 50%, 75% and 95% percentile values.

6.3.3 DCE-MRI Results – Changes After 2 Weeks

The percentage changes in mean DCE-MRI parameters are shown in Table 6.3.

	Local control	**Local failure**
k_{trans}	10.7 ± 40.9	195.7 ± 205
v_e	24.0 ± 22.5	0.7 ± 19.4
v_p	236.7 ± 355.5	642.0 ± 835.7
A	22.5 ± 22.3	31.3 ± 15.7
k_{el}	-25.6 ± 22.9	-21.3 ± 32.2
k_{21}	-4.6 ± 13.5	4.8 ± 7.0
AUC60	30.6 ± 30.3	97.0 ± 60.7
AUC90	41.9 ± 31.7	80.3 ± 43.3

Table 6.3: Percentage change in DCE-MRI parameters.

Except for k_{el} and k_{21}, all DCE-MRI parameters showed a general trend of increase after the start of treatment. There were significant differences between the

LC and the LF group for the change in 25% percentile k_{trans}, 75% percentile k_{trans}, 95% percentile k_{trans} and mean k_{trans} with p-values of 0.002, 0.03, 0.011 and 0.007 respectively after Bonferroni correction. Tumors in the local failure group demonstrated a larger increase in k_{trans} as compared to those with local treatment control. Data plot for these parameters are shown in Figure 6.1.

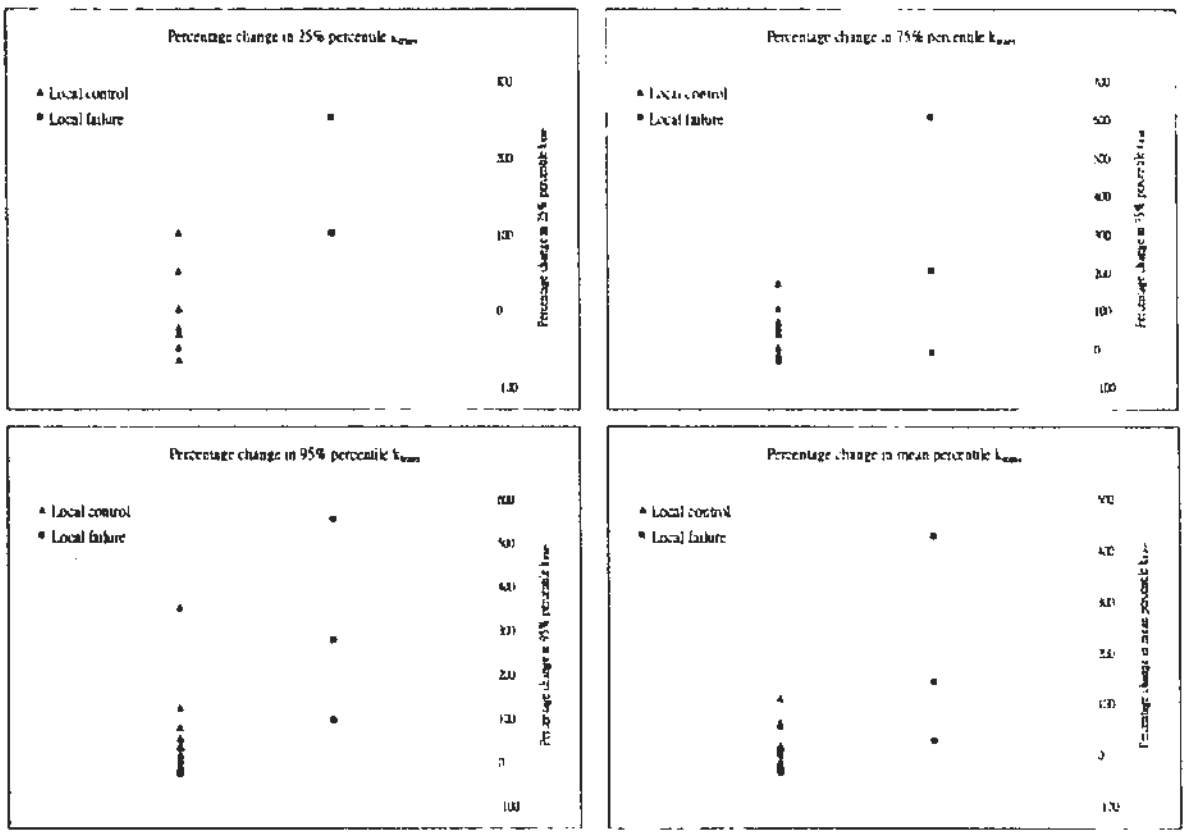

Fig. 6.1: 25% percentile k_{trans} (upper left), 75% percentile k_{trans} (upper right), 95% percentile k_{trans} (lower left) and mean k_{trans} (lower right). Local control (▲) and local failure group (■) are shown.

Amongst these parameters, the 25% percentile k_{trans} demonstrated the highest significance of difference between the 2 groups. Also, a maximum accuracy in

differentiating patients with local failure from those with local control was obtained by using this parameter. By choosing a cutoff value of 100% for the change in 25% percentile k_{trans}, the sensitivity and specificity in prediction of local failure was maximized. A sensitivity of 100% and specificity of 84.6% was obtained.

6.4 Discussion

This small pilot study evaluated DCE-MRI parameters obtained from Tofts model and area under contrast concentration curve (AUC60 and AUC90) to predict treatment outcome at the primary site of HNSCC in patients treated by chemoradiation or radiotherapy alone. Quantitative and pharmacokinetic models have been the trend and recommended tool of analysis for DCE-MRI data (Leach, Brindle, Evelhoch, et al., 2005). The use of pharmacokinetic modeled DCE-MRI for prediction of treatment outcome in the head and neck region, has to the authors' knowledge only been reported by Kim et al (2010). That study showed that the pretreatment k_{trans} in 33 metastatic cervical lymph nodes was significantly lower in nodes that showed a residual disease after treatment than in those that responded. For other types of cancers, reports have been published using pretreatment k_{trans} and AUC as a predictor of treatment outcome. Zahra et al (2009) showed that a higher pretreatment k_{trans} was related to better tumor regression in cervix cancer treated with chemoradiation. George et al (2001) reported similar relationship between k_{trans} and

response to treatment in rectal cancer patients. Jarnagin et al (2009) showed that a higher pretreatment AUC in primary liver tumors is correlated to better survival after chemotherapy. In general, higher baseline k_{trans} or AUC, which implies better perfusion or higher permeability of tumor vessels correlated with a better treatment outcome. Our data is in accordance to this general trend, showing a higher average k_{trans} and AUC in the LC group. However, significance was not reached for the difference between the LC and LF group, and a larger study is necessary to confirm this trend in head and neck primary tumors.

This study further investigated the use of DCE-MRI in the early phase of therapy for prediction of treatment outcome. Results showed that the change in k_{trans} early in a course of treatment (2 weeks after the start of treatment) has the potential to predict treatment outcome. Those patients who showed a significantly higher increase in k_{trans} were more likely to fail treatment. A similar trend was observed in our data for AUC60 and AUC90, despite the fact that significance was not reached.

Effective cancer treatment ultimately leads to the destruction of tumor vascular structures, leading to a reduction in k_{trans} for responding tumors (Pickles, Lowry, Manton, et al., 2005). However, early in the course of treatment variable results have been reported. A reduction in DCE-MRI vascular parameters has been shown when using chemotherapy in two publications studying breast cancer, which demonstrated a reduction in AUC and k_{trans} in responders early after the start of treatment (Ah-See,

Makris, Taylor, et al., 2008; Johansen, Jensen, Rydland, et al., 2009). On the other hand, when using radiotherapy an early increase in k_{trans} is usually observed in tumors, which is believed to be mostly due to inflammation. Due to the offset of these two effects (an increase in vascularity from inflammation and a decrease from tumour vascular destruction) it may be expected that an effective chemoradiation therapy regime should induce a smaller rise in DCE-MRI parameters at the early stage of treatment. This hypothesis is proposed to explain our results, which showed that the increase was significantly lower in the LC group than in the LF group.

Our data showed that the change in the 25% percentile k_{trans} was shown to be the best predictor for treatment failure. This suggested the importance of assessing heterogeneity of a tumour. Rose et al (2009) proposed that spatial arrangement of DCE-MRI parameters might carry essential diagnostic and prognostic information, and spatial heterogeneity in DCE-MRI parameters has been shown to be useful to predict tumor control and recurrence in cervical cancer (Yuh, Mayr, Jarjoura, et al., 2009; , Prescott, Zhang, Wang, et al., 2010) and breast cancer (Pickles, Lowry, Manton, et al., 2005). There has been no report on the use of heterogeneity analysis on DCE-MRI to predict treatment response in head and neck cancer, and we believe that our data is the first to show such potential for this cohort of patient.

Our study involved only a limited number of subjects, and only 3 patients showed failure in local control. Level of significance for certain parameters to show

a difference between the two groups is thus limited. Further investigation with a larger study population may confirm potential of these parameters for prediction of treatment response.

6.5 Summary

Results from this small pilot study showed that primary HNSCC with a smaller increase in tumor perfusion at the early stage of treatment, as represented by the DCE-MRI parameter k_{trans}, were significantly more likely to fail treatment. Heterogeneity assessment added value to the predictive power of the DCE-MRI parameters. Results showed also a trend towards higher average k_{trans} and AUC in primary tumors that responded to treatment, although with the small numbers of patients the results did not reach significance. DCE-MRI pararneter k_{trans}, derived from pharmacokinetic models have the potential to be a marker to predict treatment failure in HNSCC.

7.1 Introduction

The parotid glands lie within, or close to, the radiation field of many head and neck cancers and hence these glands are often unavoidably irradiated during radiation treatment (RT). Radiation injury to the parotid glands induces xerostomia which has a significant impact on the patient's quality of life. New developments in radiotherapy have focused on using techniques such as conformal RT and intensity modulated radiotherapy (IMRT) to reduce the radiation dose to the parotid glands, while at the same time delivering sufficient dose to the cancer targets (Kam, Leung, Zee, et al., 2007; Eisbruch, Ten Haken, Kim, et al., 1999).

However, even with these newer techniques it is not always possible to prevent the glands from receiving a significant radiation dose. There is, therefore, interest in finding other strategies for better protection of the organ. These require an understanding of the process of radiation induced damage on a cellular level. Histological studies have been conducted in rats and rhesus monkeys, which showed inflammation, edema, acinar cell degeneration and necrosis, vessel damage and organ atrophy after irradiation (Stephens, Ang, Schultheiss, et al., 1986; Konings, Faber, Cotteleer, et al., 2006). Similar studies are more difficult to perform on human

subjects due to the invasive nature of obtaining parotid tissue samples and inability to examine the whole gland. Therefore, an in-vivo tool to monitor radiation damage in the parotid on the cellular and vascular level would be valuable.

Dynamic contrast-enhanced magnetic resonance imaging (DCE-MRI) is a functional imaging technique that provides information on tissue perfusion through dynamic contrast analysis by compartment modeling or curve fitting. DCE-MRI parameters, obtained using pharmacokinetic models such as those proposed by Tofts and Kermode (1991) and Brix et al (1991), provide data which can reflect physiological processes such as vascularity, vessel permeability and cellularity of the examined tissue. DCE-MRI has the potential to yield valuable in-vivo information into the damage that occurs in organs that are irradiated and therefore provides a non-invasive method for studying the irradiated parotid glands. The focus of this study was to use DCE-MRI to determine if radiation leads to any changes in the DCE-MRI parameters and if so to determine if there is any correlation with radiation dose and the degree of parotid gland atrophy.

7.2 Methods

7.2.1 Patients

DCE-MRI data was retrospectively evaluated in a cohort of patients undergoing radiotherapy for nasopharyngeal carcinoma (NPC) who had been recruited for

another DCE-MRI study which had been performed with ethical approval from the local ethics committee and informed consent. All patients received baseline DCE-MRI before treatment and at 3 months after treatment. The mean radiation dose received by each parotid gland in each patient was obtained from the treatment planning records. Patients were treated with IMRT at a dose of 70 gray (Gy) to the gross tumor over a period of 7 weeks.

7.2.2 Image Acquisition and Data Processing and DCE-MRI Parameters

Image acquisition and processing were performed according to the protocol described in the chapter 5. Maps of DCE-MRI parameters including k_{trans}, v_e, v_p from the Tofts and Kermode model, A, k_{21}, k_{el} from the Brix model, AUC60 and AUC90 were generated.

For each patient, both parotid glands were contoured on the T1 scan before and after treatment. A single observer performed the contouring. Volume atrophy was defined as the percentage reduction in volume of the parotid gland after radiotherapy.

The mean DCE-MRI parameters of each of gland were obtained for analysis. Examples of the parameter images with the T1W contrast enhanced image are shown in Figure 7.1.

(a)

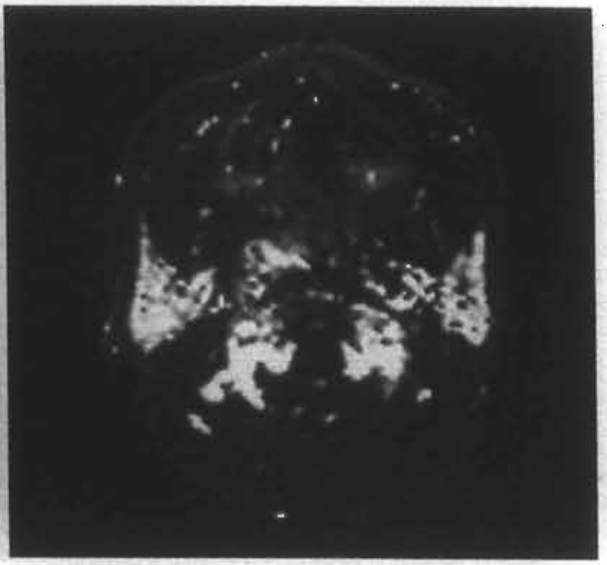

(b)

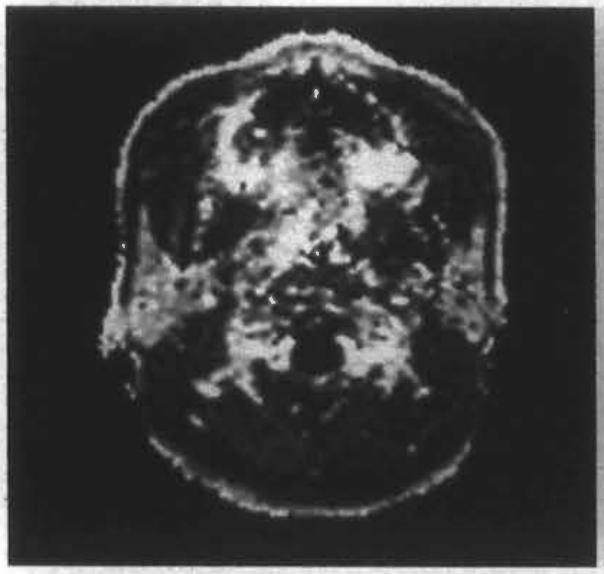

(c)

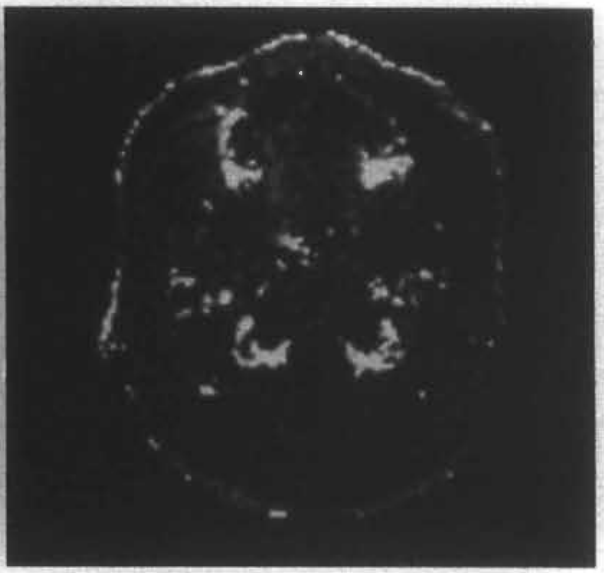

(d)

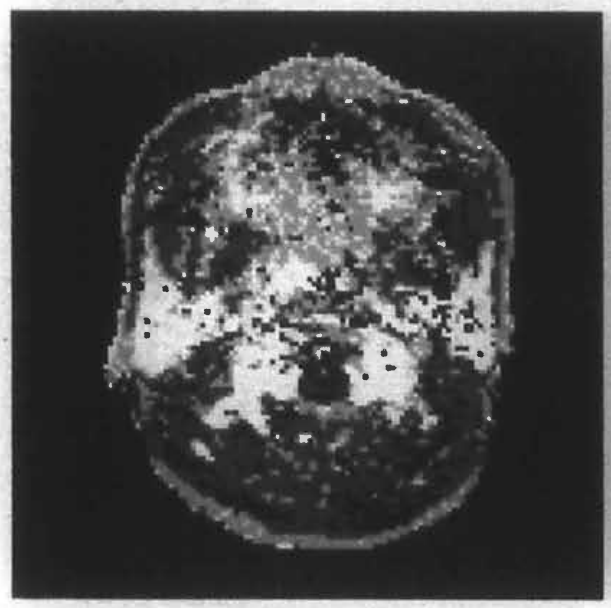

(e)

(f)

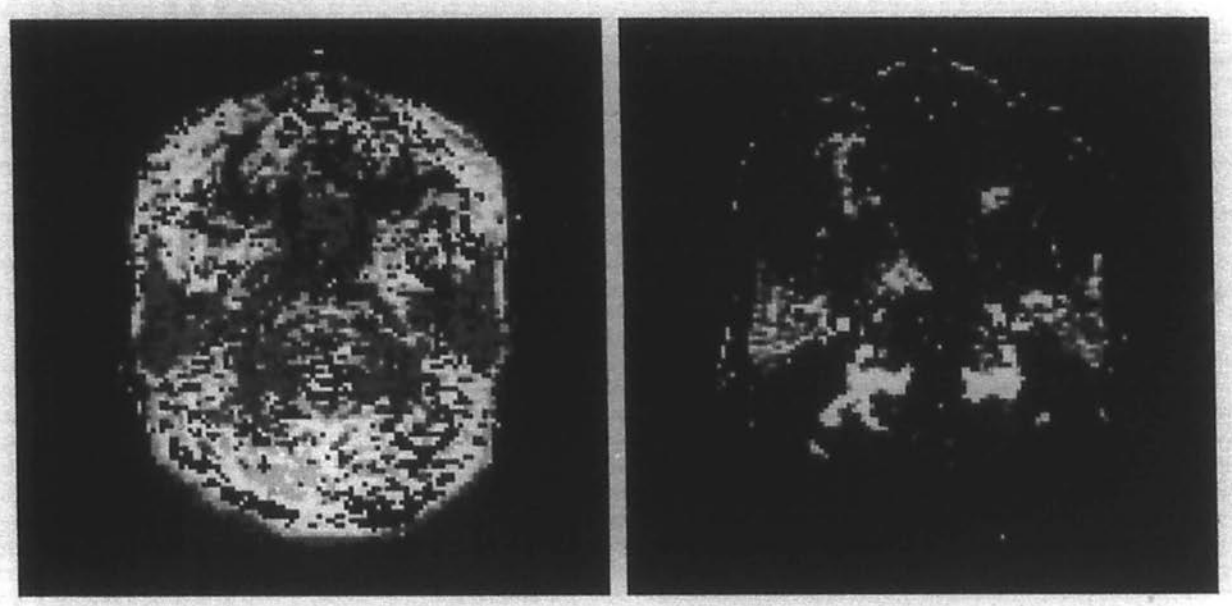

(g) (h)

(i)

Figure 7.1: Parameter maps of (a) T1W contrast enhanced image, (b) k_{trans}, (c) v_e and (d) v_p, (e) A, (f) k_{21}, (g) k_{el}, (h) AUC60, (i) AUC90.

* Right Parotid gland

** Left Parotid gland

7.2.3 Statistical analysis

Three objectives underwent statistical analysis. The first objective was to identify a significant change in any of the DCE-MRI parameters after radiotherapy by the use of paired t-test. The second objective was to correlate any changes in DCE-MRI parameters with radiation dose. The third objective was to correlate baseline DCE-MRI parameters and post-irradiation change in DCE-MRI parameters with parotid volume atrophy. For the last two objectives, Pearsons' test was used to test for any significant correlations. P-values were corrected by Bonferroni method on multiple correlation tests. All statistical tests were conducted with the software PRISM (La Jolla, CA, USA).

7.3 Results

7.3.1 Patients

The study comprised of 21 patients (16 males and 5 females with a mean age 49.0 ± 9.9, age range: 30-62), with 42 parotid glands for analysis. The mean radiation dose received by each parotid gland was 47.1 ± 6.6 Gy. Concurrent chemotherapy was also administered to the patients. The mean parotid gland atrophy was -32 ± 20%. All AIFs extracted from the patients were visually inspected to contain clearly distinguishable 1st and 2nd pass of contrast in the contrast concentration curve. This served as a quality assurance process to exclude artifact in the arteries. Also, we

examined the reproducibility of the AIF and obtained reproducibility (signifying range of variation with a 95% confidence interval) of about 30% for AUC60 and AUC90 of AIF. The induced variation in DCE-MRI parameters is significantly less than the change induced by radiation in this study.

7.3.2 DCE-MRI parameters

The mean DCE-MRI parameters before radiotherapy (baseline) and after radiotherapy (3 months post treatment) are shown in table 8.1. All DCE-MRI parameters showed a significant rise after radiotherapy ($p < 0.01$).

Parameters	Baseline	3 months post-treatment	p-value
k_{trans} (1/min)	0.89 ± 0.40	1.52 ± 0.33	< 0.0001
v_e	0.42 ± 0.13	0.81 ± 0.13	< 0.0001
v_p	0.044 ± 0.018	0.21 ± 0.12	< 0.0001
A	37.7 ± 8.33	138.2 ± 26.5	< 0.0001
k_{el} (sec^{-1})	0.056 ± 0.015	0.040 ± 0.008	< 0.0001
k_{21} (sec^{-1})	0.020 ± 0.003	0.022 ± 0.001	0.0033
AUC60	0.260 ± 0.094	0.533 ± 0.131	< 0.0001

Table 7.1: Summary statistics.

7.3.3 Correlation of radiation dose with change in DCE-MRI parameters

Results showed there was a significant inverse correlation between percentage change in k_{trans} and radiation dose ($p = 0.0045$), a higher radiation dose being correlated with a smaller percentage change in k_{trans}. However, the correlation is insignificant ($p = 0.1695$) when a possible outlier with higher percentage change in k_{trans} is removed from the analysis. No significant correlation was found between the other DCE-MRI parameters and radiation dose.

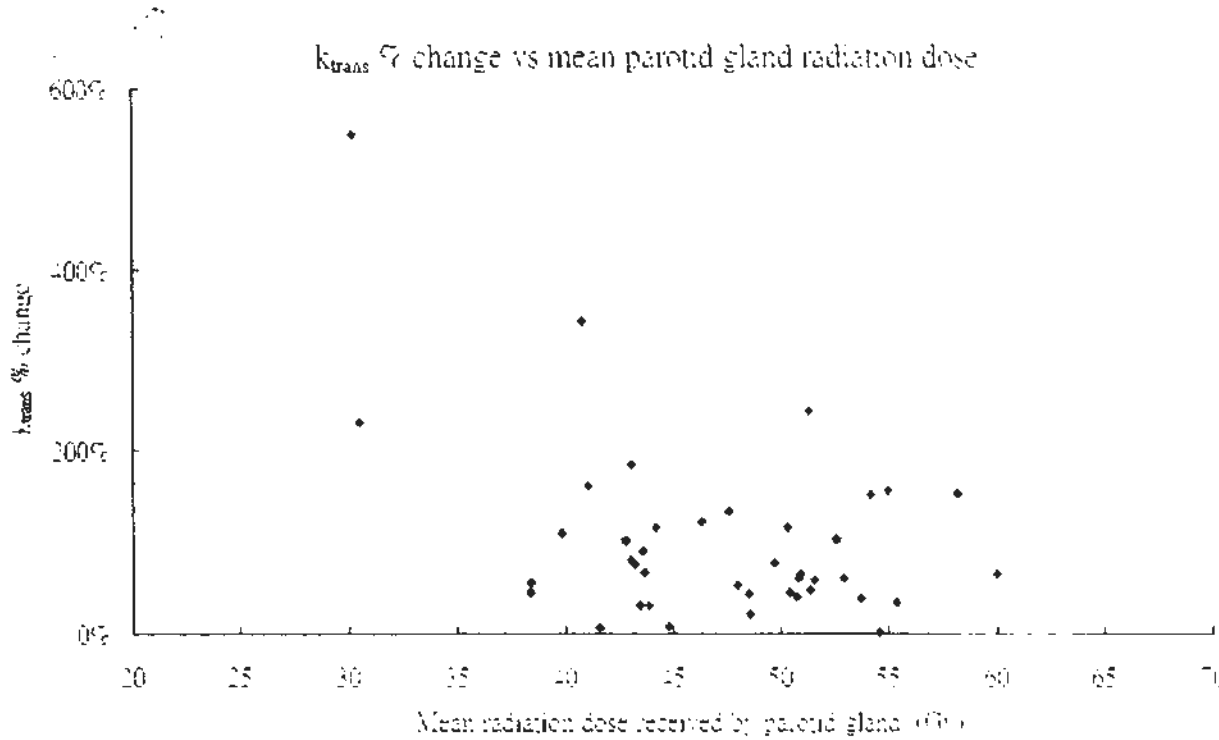

Figure 7.2: Plot of percentage change in k_{trans} versus mean radiation dose received by the parotid glands.

7.3.4 Correlation of parotid gland atrophy with DCE-MRI parameters before and after treatment

Parotid gland atrophy correlated with baseline v_e and v_p ($p = 0.0008$, 0.0003 respectively) and change in v_e after treatment ($p = 0.0022$). Atrophy being less in patients with a higher baseline v_e and v_p and lower percentage increase in v_e after radiotherapy (Figures 3 and 4). There was no correlation between parotid gland atrophy and other DCE-MRI parameters.

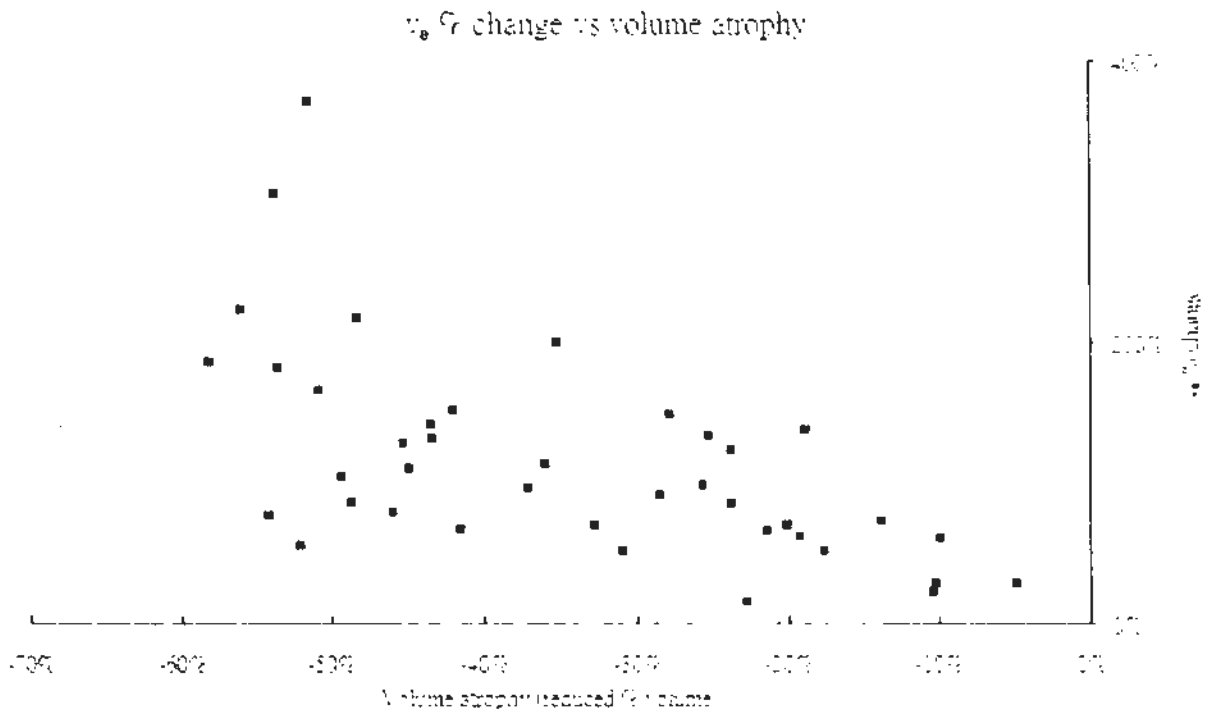

Figure 7.3: Plot of percentage change in v_e versus volume atrophy.

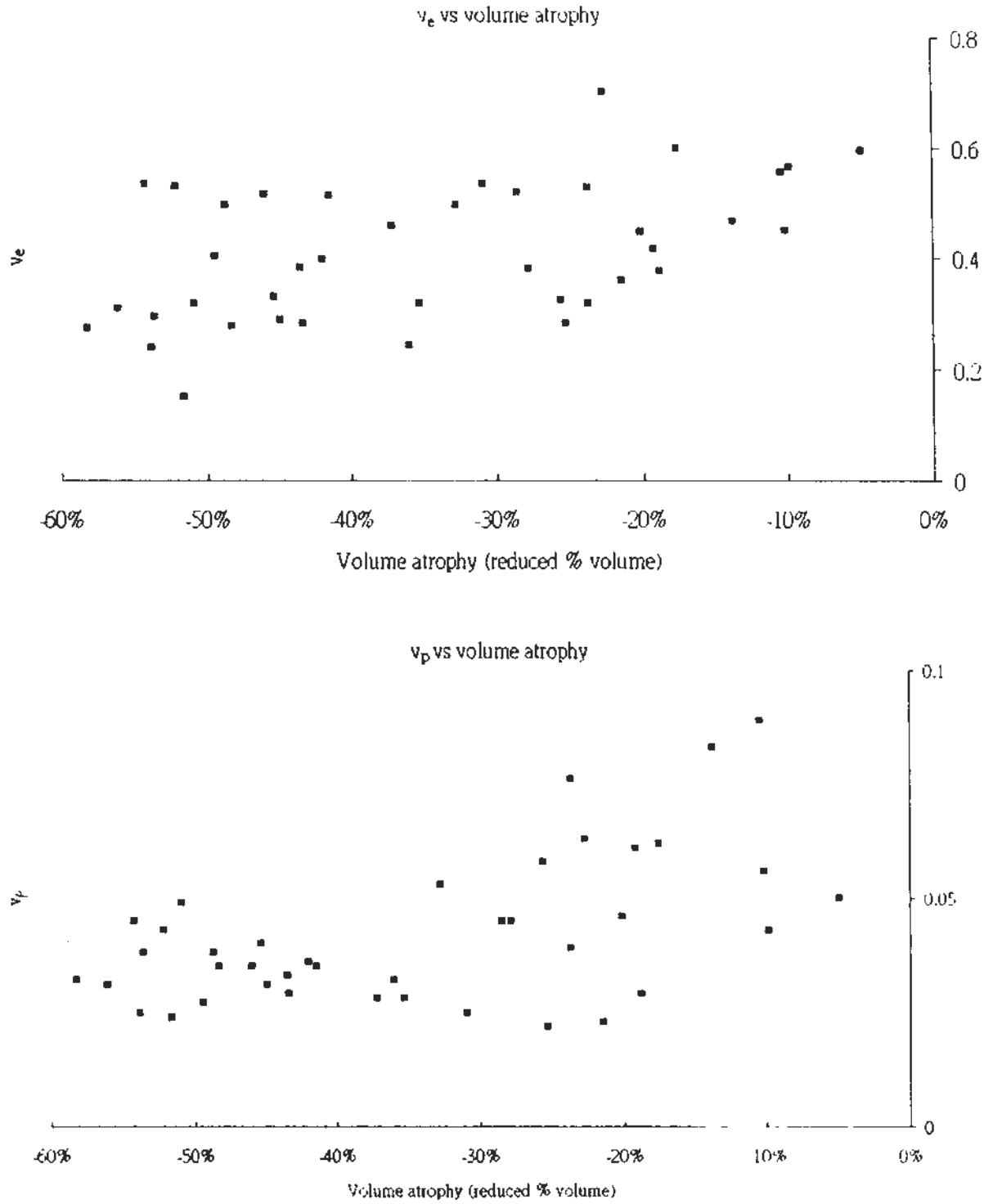

Figure 7.4: Plot of baseline v_e and v_p versus volume atrophy.

7.4 Discussion

Human and animal studies have shown parotid gland volume atrophy and reduced salivary production are both common in irradiated parotid glands (Kam,

Leung, Zee, et al., 2007; Stephens, Ang, Schultheiss, et al., 1986; Bussels, Maes, Flamen, et al., 2004) and the radiation dose delivered to the parotid glands correlates with the loss of parotid function (Eisbruch, Ten Haken, Kim, et al., 1999). Other animal studies have shown this change in salivary function is directly related to histological changes (Stephens, Ang, Schultheiss, et al., 1986; Konings, Faber, Cotteleer, et al., 2006). Degeneration, necrosis of acinar cells, and inflammation are seen in the early stage of irradiation while later changes include organ atrophy and an increase in the amount of connective tissue (Stephens, Ang, Schultheiss, et al., 1986).

Imaging studies on irradiated parotid glands have been published, with an emphasis on changes in salivary production (Blanco, Chao, El Naqa, et al., 2005) or dosimetric sparing of the organ (Wada, Uchida, Yokokawa, et al., 2009). In this study, we used DCE-MRI as a tool to investigate the effect of radiation on the parotid glands. Despite the fact that no data on parotid function was available in this study, attempt was made to correlate the DCE-MRI result with parameters or attributes that were closely related to parotid function. Radiation dose and volume atrophy have been shown to relate to parotid function. Teshima et al (2010) showed in radiation treated head and neck cancer patients that fractional reduction in parotid gland volume was significantly correlated to reduction in saliva amount. The author concluded that parotid volume reduction may predict irradiated saliva gland function. On the other hand, acinar cell was known to contribute the water and protein content

of saliva, and acinar cell loss was one major cause of volume reduction in human parotid glands after irradiation (Lombaert, Brunsting, Wierenga, et al., 2008). Loss of acinar cell thus resulted in reduction of parotid gland volume and ability of saliva production. These studies provided evidence for the close relationship between volume atrophy and loss of function in parotid gland. In this way, if a relationship between DCE-MRI parameters and atrophy could be shown, that implied a possibility that DCE-MRI parameters may also be correlated with parotid function. This will be useful clinically, although further DCE-MRI studies to include functional data is necessary for confirmation.

The first objective was to determine if radiotherapy would cause any significant change in the DCE-MRI parameters and if so whether there was any correlation with radiation dose. The results of this study demonstrated that all three DCE-MRI parameters increased significantly three months after completion of radiotherapy, as compared to the baseline values. It is postulated that the increase in k_{trans} may be the result of the early inflammation and disruption of normal endothelium induced by radiation. Such observations are reported in irradiated tumors at the initial stage of radiation therapy (Zahra, Hollingsworth, Sala, et al., 2007; Ng, Goh, Milner, et al., 2007). It is also known that later on, radiation subsequently damages the vessels and reduces permeability and vascular density, which would be expected to lead to a decrease in the k_{trans}. The fact that a rise and not a fall in k_{trans} was seen in this study

suggests that the glands were still going through this earlier phase of damage at three months after radiotherapy with inflammation and endothelium disruption being the predominant feature. However, a weak negative correlation was found between the percentage change in k_{trans} and radiation dose, that is, higher radiation doses caused less of a percentage rise in the k_{trans}. A possible explanation for this unexpected result is that glands that received the higher dose were already starting to enter the later phase of damage so that the effects of inflammation and endothelium disruption were being counteracted by the later effect of vessel damage which cause a decrease in permeability and vascular density and hence decrease in k_{trans}. Yet, our observation was limited by the fact that radiation dose received by the parotid glands in our study were quite large. A better correlation may be demonstrated in future studies between DCE-MRI parameters and a wider range of radiation dose.

The v_e and v_p also showed a rise after radiotherapy. In the case of v_e it is postulated that the rise may have been be related to the increase in extra-cellular extra-vascular space (EES) caused by serous acinar cell loss and edema. In the case of v_p it is postulated that rise may have been be related to inflammation which induces vasodilatation and so could increase blood volume. However, unlike the k_{trans} neither of these two DCE-MRI parameters showed a direct correlation with radiation dose.

The second objective was to correlate parotid gland atrophy with DCE-MRI

parameters. The study showed that there was a relationship between v_e and v_p but not with the k_{trans}. A higher baseline v_e and v_p was associated with less glandular atrophy. The cause for this association with respect to v_e is unclear but for v_p it is possible that glands with a higher plasma volume, meaning that the organ is better perfused, would have greater protection from radiation injury. A greater percentage increase in v_e was observed in organs with greater atrophy which would be expected given that organ atrophy and increased EES are results of increased radiation dose.

A similar study from Juan et al (Juan, Chen, Jen, et al., 2009) has reported using the Brix model which showed a correlation between DCE-MRI parameters and radiation dose. They reported that the peak enhancement and time to peak were correlated positively while the k_{el}, was correlated negatively to dose. They attributed the decrease in k_{el} to increased EES after cell loss, which is in accord to our observation of increased v_e after radiotherapy. The k_{21}, which is the transfer rate constant between plasma and EES, also decreased after radiotherapy. This is in contradiction to our observation of increased k_{trans}. Part of the reason for this discrepancy may be the difference in timing of image acquisition between the two studies. Juan's cohort of patients included RT-MR time varying from 2 to 43 months. Our study imaged patients at baseline and at 3 months after treatment, which is advantageous for describing the early RT effects.

The main limitation of this study is that without excision of the parotid gland

the cellular cause for the DCE-MRI observations can only be postulated. Animal studies would be needed to confirm the histological basis of the DCE-MRI findings. Also, the present study only examined the effects of radiation at one time point soon after treatment, with no correlation with gland function. To study the correlation between DCE-MRI parameters with late effect of glandular function, prospective study with serial imaging and salivary flow measurement would be necessary.

In summary, the study increased knowledge on irradiated parotid glands from the perspective of vascular change by the use of DCE-MRI. Baseline parameters such as v_e and v_p that demonstrated significant correlation with organ atrophy showed potential of such parameters in predicting response after radiotherapy. Treatment planning may make use of this information for tailor-made sparing strategies with individual patients.

7.5 Summary

This study shows the potential of DCE-MRI to be a non-invasive tool for examining radiation induced injury in the parotid glands at a cellular level. A significant increase in k_{trans}, v_e and v_p, A, k_{21} and a reduction in k_{el} have been shown in the parotid gland three months after irradiation for the treatment of head and neck cancer. The correlation between greater glandular atrophy and a lower baseline v_e and v_p and higher post treatment increase in v_e shows the potential for using

DCE-MRI for prediction and assessment of radiation damage to the organ.

8.1 Summary of Results

The thesis has described the work on DCE-MRI, in particular the use of the pharmacokinetic models proposed by Tofts and Kermode, and Brix, and the semi-quantitative metrics of Area Under Curve (AUC). The work was focused on the application of the technique in the head and neck region. In the first part, major technical issues pertaining to the acquisition and processing of DCE-MRI data were studied, from which results were generated to optimize the acquisition and analysis protocol. Three pilot clinical studies followed suit to demonstrate the potential clinical usefulness of the technique in the management of head and neck cancer. It was expected that the work will add to the existing limited evidence on the technical and clinical aspects of DCE-MRI in this specific part of the body. Future work is encouraged to be undertaken for the ultimate application of DCE-MRI in clinical usage.

8.1.1 Technical Studies

The first part of the thesis was focused on the technical issues of DCE-MRI that was related to 1) data acquisition and 2) processing of the technique. The findings were used to establish the protocol, and the protocol was applied on several

applications in head and neck cancers. The acquisition protocol was studied in the first place. Spoiled gradient echo pulse sequences with flip angles of 2, 10, 20 and 30 degrees were found to yield good reproducibility of T1 estimation. A flip angle of 20 degree was chosen for the dynamic acquisition as optimal to yield good signal-to-noise ratio as well as to reduce sensitivity of parameter estimation to flip angle errors. The T1 estimation was validated by phantom and in-vivo measurement.

The effect of signal-to-noise ratio (SNR) in the dynamic acquisition data on the outcome of DCE-MRI was studied. A reduction in the precision of all the DCE-MRI parameters, except k_{el}, due to increased level of noise was observed. v_p is the most susceptible to noise in terms of estimation precision. The parameters k_{21} and A demonstrated the highest degree of robustness for parameter estimation at different noise levels. Sufficient SNR is needed in the acquired DCE-MRI data, especially if parameters sensitive to noise have to be employed. Noise reduction strategies include using ROI analysis, or tradeoff of image coverage and temporal resolution, etc.

On the other hand, scan duration is another data acquisition parameter that may affect the processing outcome, and thus was studied in this thesis. Reduced scan duration resulted in increased deviation of the estimated DCE-MRI parameters, especially for k_{el} and k_{21}. The estimation of v_p became highly variable at reduced scan duration. Parameter estimation for Brix model was increasingly unstable with reduced scan duration. In summary, it was suggested that if Tofts and Kermode

model was used for analysis, reducing scan duration would reduce the reliability of v_p. Otherwise, reducing the scan duration down to 231 sec does not create significant issue to parameter estimation. For the Brix model, reducing the scan duration to 305 sec would result in about 10% failure in curve fitting. Also, the accuracy deteriorates appreciably for the estimation of k_{el} and k_{21} below this scan duration.

With the above results, an acquisition protocol was established, which could complete data acquisition within approximately 7 minutes.

The DCE-MRI analysis process was further investigated, which included the issues of 1) Arterial Input Function (AIF); 2) omission of the plasma contribution in Tofts and Kermode model, and; 3) assessment on the reproducibility of the DCE-MRI parameters.

Results showed that bilateral AIF from the carotid artery in the cervical neck region were not substantially different, thus the left and right carotid arteries could be used for DCE-MRI processing. Individual-AIF was preferred over population-averaged AIF in terms of reproducibility of the estimated parameters. Finally, both random and systematic error in AIF affected the accuracy and precision of DCE-MRI. The relative importance of these errors depended on the DCE-MRI parameter that was employed. If k_{trans} is the primary objective of the analysis, random noise should be reduced in the images. On the other hand, if v_e and v_p were the primary objectives, sources of systematic error in AIF may need to be reduced.

Omission of the term $C_p v_p$ in the curve fitting induced error of up to 53.1% in k_{trans}. Error in the estimated v_e may exceed 10%. The error increased with higher values of v_p, or lower values of k_{trans} or v_e. Curve fitting error was higher with higher values of v_p. The effect of omitting $v_p C_p$ in the estimation expression was thus substantial in the head and neck lesions.

The reproducibility of the DCE-MRI parameters generated in the studies of this thesis was comparable to those reported in other literatures. In general, the wCV of the DCE-MRI parameters studied in this thesis was 10-30% in head and neck lesions, with better reproducibility for v_e in Tofts' model and k_{21} in Brix model. These results guaranteed the quality of the data and the processing in the clinical studies that followed.

8.1.2 Clinical Studies

The DCE-MRI protocol, which generated DCE-MRI parameters from the Tofts' and Kermode model and Brix model, and also quantitative parameters such as AUC60 and AUC90, was validated for their clinical usefulness in 3 head and neck clinical applications: differentiation of lesion types, prediction of treatment failure and assessment of irradiated parotid glands.

Several parameters were shown to bear significant difference between undifferentiated carcinoma (UD) and squamous cell carcinoma (SCC), and also

between UD and lymphoma. These parameters were k_{trans}, AUC60 and AUC90. However, no parameters showed a difference between SCC and lymphoma. The highest accuracy for DCE-MRI was obtained by taking into account tumor heterogeneity to analyze different percentile values obtained from a histogram. Of all DCE-MRI parameters the AUC90 was shown to produce the highest accuracy, which could be an advantage in routine clinical practice because of its relative simplicity in the process of parameter extraction compared to the model based parameters such as k_{trans}.

Results from a small pilot study showed that primary HNSCC with a smaller increase in tumor perfusion at the early stage of treatment, as represented by the DCE-MRI parameter k_{trans}, were significantly more likely to fail treatment. Heterogeneity assessment added value to the predictive power of the DCE-MRI parameters. Results showed also a trend towards higher average k_{trans} and AUC in primary tumors that responded to treatment, although with the small numbers of patients the results did not reach significance. DCE-MRI parameter k_{trans}, derived from pharmacokinetic models had the potential to be a marker to predict treatment failure in HNSCC.

The last clinical study showed potential of DCE-MRI to be a non-invasive tool for examining radiation induced injury in the parotid glands at a cellular level. A significant increase in all DCE-MRI parameters has been shown in the parotid gland

three months after irradiation for the treatment of head and neck cancer. The correlation between greater glandular atrophy and a lower baseline v_e and v_p and higher post treatment increase in v_e showed the potential for using DCE-MRI for prediction and assessment of radiation damage to the organ.

In summary, the studies in this thesis demonstrated the effort to establish a protocol for DCE-MRI of the head and neck region. The protocol has been validated by in-vivo data in terms of reproducibility. Clinical application of the technique has been demonstrated. The k_{trans} and v_e from the Tofts' model, and the AUC60 and AUC90 seemed to bear the highest potential for clinical use, and the relative strength of individual parameters depends on the specific application. AUCs are in general simpler to generate, and is more robust as demonstrated by the reproducibility results. Model generated parameters, despite the complicated means of parameter generation, bear physiological meaning. It is also shown to be more sensitive to infer predict radiation effect on parotid glands and for the prediction of tumor local control.

8.2 Future Work

This thesis demonstrated the potential of DCE-MRI for the management of head and neck cancer. A number of future directions for the development of the technique are proposed.

8.2.1 3T DCE-MRI

With the matured technology and pulse sequences, 3T MRI scanners are gaining popularity in clinical use. The major advantage of increasing the magnetic field from 1.5T to 3T is the increased signal, which may improve the precision on the estimation of DCE-MRI parameters. Moreover, new scanners are equipped with better phase array coils, which further increase signal and imaging speed; faster gradient equipped in new scanners also enable acquisition of dynamic data with better temporal resolution. All these are advantages to explore the use of DCE-MRI in the 3T environment.

A number of DCE-MRI studies were conducted in 3T scanners, and the majority of them were focused on the application in prostate (Kozlowski, Chang, Meng, et al., 2010) and breast cancer (Di Giovanni, Azlan, Ahearn, et al., 2010). Relaxation parameters of tissues under the magnetic field of 3T are different from that in 1.5T. Also, improved hardware may allow better spatial and temporal resolution for the acquired data. Thus the optimal acquisition protocol may need to be determined in 3T scanners, and a thorough investigation to fine tune the protocol for 3T DCE-MRI in head and neck cancers would be required.

Kim et al (2010) predicted chemoradiation treatment response in head and neck squamous cell carcinoma by DCE-MRI in 1.5T and 3T scanners. He did not showed significant difference in the results using either 1.5T or 3T. However, Martí-Bonmatí

et al (2008) suggested that DCE-MRI parameters in cartilage were different in 1.5T and 3T scanners. This proposed the possibility that DCE-MRI parameters has to be determined separately for 3T and 1.5T, and cross referencing the parameter values may not be appropriate. Further clinical studies may need to be performed in both 1.5T and 3T scanners, to demonstrate the advantage of the latter to the former, and also to establish the reference DCE-MRI values in 3T MRI for clinical use.

8.2.2 Flip Angle Uncertainties

Spoiled gradient echo is a common pulse sequence for determination of T1 and dynamic data acquisition in DCE-MRI. Flip angle uncertainties are induced by heterogeneity of the B1-field transmission. The issue is more pronounced in the situation of uneven loading of the RF transmission coils, and in high field strength where the standing radiofrequency (RF) wave effect is more prominent (Ibrahim, Lee, Abduljalil, et al., 2001). Variation in flip angles will result in erroneous determination of T1, and in turn affects substantially the accuracy of DCE-MRI parameters (Di Giovanni, Azlan, Ahearn, et al., 2010). The common method to correct for this problem is the determination of B1-field map to cater for differences in RF transmission. However, this requires additional software and manipulation of images. Further studies may be needed to estimate the influence of such in the head and neck region and devise optimal method of correction.

8.2.3 AIF Extraction

AIF affects substantially the estimation of DCE-MRI parameters. The quality of AIF depends on the location of extraction and image quality. Difficulty to determine the accurate T1 of the arteries also deteriorates the AIF. Quality of AIF affects the estimation of DCE-MRI parameters, and it was shown in this thesis that individual-AIF yielded better result than population-averaged AIF in terms of DCE-MRI parameters reproducibility. The selection of the best AIF in the head and neck region is challenging because of the numerous artery supplies to the lesions or organs of interest, and also the small size of the arteries involved. At present, the AIFs were selected manually, and this is a time consuming process which is also prone to intra- and inter-observer errors. Research groups have proposed auto-segmentation of the artery for AIF extraction (Peruzzo D., Bertoldo A., Zanderigo F., et al., 2011), albeit further validation is required for reliable application in the head and neck region.

Other problems such as inflow effect for the AIF has been shown to affect result of estimated DCE-MRI values (Garpebring, Wirestam, Ostlund, et al., 2011; Roberts, Little, Watson, et al., 2011). Further studies to devise methods for robust AIF in the head and neck region are worthwhile to be pursued.

8.2.4 Deformable Registration

Image registration software corrects for patient motion during the scan. This will improve the contrast concentration data, and an accurate registration of the images is essential if higher spatial resolution is to be pursued for DCE-MRI. At present, rigid registration is the common type of method to correct for image misalignment. Such method corrects for translation and rotation of the patient body. However, non-rigid deformation, which results in the change in the shape of the patient anatomy, may occur due to swallowing motion, change in neck flexion angle, motion of jaws, tongues, etc. Correction of these is difficult but essential especially when the tissue of interest is near to these areas. A number of research groups have developed algorithm for deformable registration of head and neck images, which were mostly used on CT images for adaptive radiotherapy (Al-Mayah A., Moseley J., Hunter S., 2010). Deformable registration for MRI, with the sub-millimeter accuracy required in tumor assessment, requires substantial future research effort.

8.2.5 Auto Lesion Segmentation

Lesion segmentation is often performed in DCE-MRI analysis if statistics on the lesion is to be obtained. At present, lesion segmentation is performed manually by radiologists or experienced researchers. Intra-observer and inter-observer variation exists, which may contribute to the uncertainty in DCE-MRI statistics. Software

algorithms that can automatically segment lesions on MR images reduce the workload and also improve consistency of the contours and the statistics. Prior effort on head and neck tumor auto-segmentation (Lee F.K., Yeung D.K., King A.D., et al., 2005) needs to be explored further to improve accuracy and practicality.

8.2.6 Clinical Studies

The value of DCE-MRI on cancer management is revealed by evidence generated from clinical studies. The studies presented in this thesis have shown the potential of the technique for tumor characterization, treatment outcome prediction and evaluation of irradiated parotid glands. Further studies which involve a larger number of patients to confirm the clinical use in these areas are needed. Moreover, other clinical applications that may be worthwhile to investigate with DCE-MRI include: detection of metastatic nodal spread, biomarker for assessment of anti-angiogenic drug effectiveness, tools to identify areas for dose painting in radiotherapy, distinguishing of recurrent or residual cancer from post-irradiation necrosis, prediction of patient survival, assessment of radiation injury to organs at risk such as submandibular gland, temporal lobe necrosis, etc.

Lack of histological and functional data was another limitation of the studies. In addition to biopsy information, it is also important to obtain histological slices for direct correlation with DCE-MRI parameter maps. As shown in the clinical studies of

this thesis, heterogeneity of the DCE-MRI parameters within the tumors may provide additional clinical information. Further studies with the use of histological examination provide good validation of the heterogeneity information. On the other hand, salivary production, which is ultimate indication on the functional integrity of the parotid glands, is also needed in future studies for further confirmation of the use of DCE-MRI on the assessment of irradiated parotid glands.

The clinical utilization of DCE-MRI cannot be realized without a robust implementation protocol and software. The thesis has suggested a data acquisition protocol which is reasonably simple to implement. Processing software that is easy to use, robust, efficiency and reliable has to be developed to facilitate a widespread clinical use of DCE-MRI in the head and neck region.

8.3 Conclusions

This thesis investigated several important technical aspects of DCE-MRI, which lead to optimized protocol for the technique in the head and neck region. Clinical potential of DCE-MRI in the management of head and neck cancers have been demonstrated by 3 pilot clinical studies. Future studies are encouraged to realize the ultimate clinical application of DCE-MRI in the head and neck region.

Ah-See M.L., Makris A., Taylor N.J., et al. (2008). Early changes in functional dynamic magnetic resonance imaging predict for pathologic response to neoadjuvant chemotherapy in primary breast cancer. Clin. Cancer Res. **14**: 6580-6589.

Ahearn T.S., Staff R.T., Redpath T.W., et al. (2005). The use of the Levenberg-Marquardt curve-fitting algorithm in pharmacokinetic modeling of DCE-MRI data. Phys. Med. Biol. **50**: N85-N92.

Al-Mayah A., Moseley J., Hunter S. (2010). Biomechanical-based image registration for head and neck radiation treatment. Phys. Med. Biol. **55**: 6491-6500.

Alibek S., Zenk J., Bozzato A., et al. (2007). The value of dynamic MRI studies in parotid tumors. Acad. Radiol. **14**:701-710.

Ariyoshi Y., Shimahara M.. (2006). Relationships between dynamic contrast-enhanced MRI findings and pattern of invasion for tongue carcinoma. Oncol. Rep. **15**:1339-1343.

Asaumi J., Hisatomi M., Yanagi Y., et al. (2005). Assessment of ameloblastomas using MRI and dynamic contrast-enhanced MRI. Eur. J. Radiol. **56**: 25-30.

Asaumi J., Yanagi Y., Hisatomi M., et al. (2003). The value of dynamic contrast-enhanced MRI in diagnosis of malignant lymphoma of the head and neck. Eur. J. Radiol. **48**: 183-187.

Asaumi J., Yanagi Y., Konouchi H., et al. (2004). Application of dynamic contrast-enhanced MRI to differentiate malignant lymphoma from squamous cell carcinoma in the head and neck. Oral Oncol. **40**: 579-584.

Baba Y., Furusawa M., Murakami R., et al. (1997). Role of dynamic MRI in the evaluation of head and neck cancers treated with radiation therapy. Int. J. Radiat. Oncol. Biol. Phys. **37**:783-787.

Baba Y., Yamashita Y., Onomichi M., et al. (1999). Dynamic magnetic resonance imaging of head and neck lesions. Top. Magn. Reson. Imaging. **10**:125-129.

Bailey B.J., Johnson J.T., Newlands S.D.. Head and neck surgery– otolaryngology, 4th ed. (Philadephia, PA, Lippincott Williams & Wilkins, 2006: 1817)

Bandoh N., Hayashi T., Takahara M., et al. (2004). VEGF and bFGF expression and microvessel density of maxillary sinus squamous cell carcinoma in relation to p53 status, spontaneous apoptosis and prognosis. Cancer Lett. **208**: 215–225.

Bernstein M.A., King K.F., Zhou X.J. Handbook of MRI Pulse Sequences. (Elsevier; Amsterdam: 2004. p. 587 chapter 14)

Bisdas S., Baghi M., Wagenblast J., et al. (2009). Tracer kinetics analysis of dynamic contrast-enhanced CT and MR data in patients with squamous cell carcinoma of the upper aerodigestive tract: comparison of the results. Clin. Physiol. Funct. Imaging. **29**:339-346.

Bisdas S., Seitz O., Middendorp M., et al. (2010). An exploratory pilot study into the association between microcirculatory parameters derived by MRI-based pharmacokinetic analysis and glucose utilization estimated by PET-CT imaging in head and neck cancer. Eur. Radiol. **20**: 2358-2366.

Blanco A.I., Chao K.S., El Naqa I., et al. (2005). Dose-volume modeling of salivary function in patients with head-and-neck cancer receiving radiotherapy. Int. J. Radiat. Oncol. Biol. Phys. 62: 1055-1069.

Bloch F, Hansen W.W., Packard M. (1946). Nuclear induction. Phy. Rev. **69**: 127.

Bluml S., Schad L.R., Stepanow B., et al. (1993). Spin-lattice relaxation time measurement by means of a turboFLASH technique. Magn. Reson. Med. 30: 289-295.

Bonekamp D., Macura K.J. (2008). Dynamic contrast-enhanced magnetic resonance imaging in the evaluation of the prostate. Top. Magn. Reson. Imaging. **19**: 273-284.

Brix G., Semmler W., Port R., et al (1991). Pharmacokinetic parameters in CNS Gd-DTPA enhanced MR imaging. J. Comput. Assist. Tomogr. **15**: 621-628.

Brookes J.A., Redpath T.W., Gilbert F.J., et al. (1999). Accuracy of T1 measurement in dynamic contrast enhanced breast MRI using two- and three-dimensional variable flip angle fast low angle shot. J. Magn. Reson. Imaging **10**: 254-259.

Buadu L.D., Murakami J., Murayama S., et al. (1996). Breast lesions: correlation of contrast medium enhancement patterns on MR images with histopathologic findings

and tumor angiogenesis. Radiology **200**: 639-649.

Buckley D.L. (2002). Uncertainty in the analysis of tracer kinetics using dynamic contrast enhanced T1-weighted MRI. Magn. Reson. Med. **47**: 601-606.

Buckeley D.L., Roberst C., Parker G..J.M., et al. (2004). Prostate Cancer: Evaluation of vascular characteristics with dynamic contrast enhanced T1-weighted MR Imaging – initial experience. Radiology **233**: 709-715.

Bussels B., Maes A., Flamen P., et al. (2004). Dose response relationships with the parotid gland after radiotherapy for head and neck cancer. Radiother. Oncol. **73**: 297-306.

Byron J. Bailey, Jonas T. Johnson, Shawn D. Newlands. In: Head and neck surgery otolaryngology. 4th edition Philadephia, PA: Lippincott Williams & Wilkins, 2006: 1817

Calamante F., Gadian D.G., Connelly A.. (2000). Delay and dispersion effects in dynamic susceptibility contrast MRI: simulations using singular value decomposition. Magn. Reson. Med. **44**; 464-473.

Carmeliet P., Jain R.K. (2000). Angiogenesis in cancer and other diseases. Nature. **407**: 249-257.

Chang E.Y., Li X., Jerosch-Herold M., et al. (2008). The evaluation of esophageal adenocarcinoma using dynamic contrast-enhanced magnetic resonance imaging. J. Gastrointest. Surg. **12**: 166–175.

Chang Y.C., Huang C.S., Liu Y.J., et al. (2004). Angiogenic response of locally advanced breast cancer to neoadjuvant chemotherapy evaluated with parametric histogram from dynamic contrast-enhanced MRI. Phys Med Biol. **49**: 3593-3602.

Cheng H.L.M. (2008). Investigation and optimization of parameter accuracy in dynamic contrast enhanced MRI. J. Magn. Reson. Imaging. **28**: 736-743.

Dale B.M., Jesberger J.A., Lewin J.S., et al. (2003). Determining and optimizing the precision of quantitative measurements of perfusion from dynamic contrast enhanced MRI. J. Magn. Reson. Imaging. **18**: 575-584.

Daniel B.L., Yen Y.F., Glover G.H., et al. (1998). Breast disease: dynamic spiral MR imaging. Radiology **209**: 499-509.

Damadian R. (1971). Tumor detection by nuclear magnetic resonance. Science **171**: 1151.

Di Giovanni P., Azlan C.A., Ahearn T.S., et al. (2010). The accuracy of pharmacokinetic parameter measurement in DCE-MRI of the breast at 3 T. Phys. Med. Biol. **55**: 121-132.

Duewell S.H., Ceckler T.L., Ong K., et al. (1995). Musculoskeletal MR imaging at 4T and at 1.5T: comparison of relaxation times and image contrast. Radiology. **196**: 551-555

Eisbruch A., Ten Haken R. K., Kim H.M., et al.. (1999). Dose, volume, and function relationships in parotid salivary glands following conformal and intensity-modulated irradiation of head and neck cancer. Int. J. Radiat. Oncol. Biol. Phys. 45: 577-587.

Escott E.J., Rao V.M., Ko W.D., et al. (1997). Comparison of dynamic contrast-enhanced gradient-echo and spin-echo sequences in MR of head and neck neoplasms. Am. J. Neuroradiol. **18**:1411-1419.

Evelhoch J.. (1999). Key Factors in the acquisition of contrast kinetic data for oncology. J. Magn. Reson. Imaging. **10**: 254-259.

Evelhoch J., Garwood M., Vigneron D., et al. (2005). Expanding the Use of Magnetic Resonance in the Assessment of Tumor Response to Therapy: Workshop Report. Cancer Res. **65**: 7041–7044.

Eveloch J.L., LoRusso P.M., He Z., et al. (2004). Magnetic resonance imaging measurements of the response of murine and human tumors to the vascular-targeting agent ZD6126. Clin, Cancer Res. **10**: 3650–3657.

Fallone B.G., Rivest D.R., Riauka T.A., et al. (2010). Assessment of a commercially available automatic deformable registration system. J. Appl. Clin. Med. Phys. **11**: 3175.

Fischbein N.J., Noworolski S.M., Henry R.G., et al. (2003). Assessment of metastatic cervical adenopathy using dynamic contrast enhanced MR imaging. Am. J. Neuroradiol. **24**: 301-311.

Folkman J. (1995). Angiogenesis in cancer, vascular, rheumatoid and other disease.

Nat. Med. **1**: 27-31.

Fong D., Bhatia K.S.S., Yeung D., et al. (2010). Diagnostic accuracy of diffusion-weighted MR imaging for nasopharyngeal carcinoma, head and neck lymphoma and squamous cell carcinoma at the primary site. Oral Oncol. **46**: 603-606.

Food & Drug Authority Public Health Advisory 2006 - Gadolinium-containing Contrast Agents for Magnetic Resonance Imaging (MRI)

Fram E.K., Herfkens R.J., Johnson G.A., et al. (1987). Rapid calculation of T1 using variable flip angle gradient refocused imaging. Magn. Reson. Imaging. **5**: 201-208.

Franiel T., Hamm B., Hricak H., (2011). Dynamic contrast enhanced magnetic resonance imaging and pharmacokinetic models in prostate cancer. Eur. Radiol. **21**: 616-626.

Galbraith S.M., Lodge M.A., Taylor N.J., et al. (2002). Reproducibility of dynamic contrast-enhanced MRI in human muscle and tumours: comparison of quantitative and semi-quantitative analysis. NMR Biomed. **15**: 132-142.

Garpebring A., Wirestam R., Ostlund N., et al. (2011). Effects of inflow and radiofrequency spoiling on the arterial input function in dynamic contrast enhanced MRI: A combined phantom and simulation study. Magn. Reson. Med. In press.

George M.L., Dzik-Juarsz A.S., Padhani A.R., et al. (2001). Non-invasive methods of assessing angiogenesis and their value in predicting response to treatment in colorectal cancer. Br. J. Surg. **88**: 1628-1636.

Gratzinger D., Advani R., Zhao S., et al. (2010). Lymphoma cell VEGFR2 expression detected by immunohistochemistry predicts poor overall survival in diffuse large B cell lymphoma treated with immunochemotherapy (R-CHOP). Br. J. Haematol. **148**: 235 244.

Gratzinger D., Zhao S.C., Marinelli R.J., et al. (2007). Microvessel Density and Expression of Vascular Endothelial Growth Factor and Its Receptors in Diffuse Large B-Cell Lymphoma Subtypes. Am. J. Pathol. **170**: 1362-1369.

Guang-Wu H., Sunagawa M., Li J.E., et al. (2000). The relationship between microvessel density, the expression of vascular endothelial growth factor (VEGF),

and the extension of nasopharyngeal carcinoma. Laryngoscope **110**: 2066 - 2069.

Gückel C., Schnabel K., Deimling M., et al. (1996). Dynamic snapshot gradient-echo imaging of head and neck malignancies: time dependency and quality of contrast-to-noise ratio. MAGMA. **4**: 61-69.

Haase A., Frahm J., Matthaei D., et al. (1986). FLASH imaging - rapid NMR imaging using low flip-angle pulses. J. Magn. Reson. **67**: 258-266.

Hayes C., Padhani A.R., Leach M.O.. (2002). Assessing changes in tumour vascular function using dynamic contrast-enhanced magnetic resonance imaging. NMR Biomed. **15**: 154-163.

Hazar B., Paydas S., Zorludemir S., et al. (2003). Prognostic Significance of Microvessel Density and Vascular Endothelial Growth Factor (VEGF) Expression in Non-Hodgkin's Lymphoma. Leukemia & Lymphoma. **44**: 2089 2093.

Henderson E., Rutt B.K., Lee T.Y.. (1998). Temporal sampling requirements for the tracer kinetics modeling of breast disease. Magn. Reson. Imaging **16**: 1057-1073.

Hisatomi M., Asaumi J., Konouchi H., et al. (2002). Assessment of dynamic MRI of Warthin's tumors arising as multiple lesions in the parotid glands. Oral. Oncol. **38**: 369-372.

Hisatomi M., Asaumi J., Yanagi Y., et al. (2007). Diagnostic value of dynamic contrast-enhanced MRI in the salivary gland tumors. Oral Oncol. **43**: 940-947.

Hong Kong Cancer Registry: http://www3.ha.org.hk/cancereg/

Hoskin P.J., Saunders M.I., Goodchild K., et al. (1999). Dynamic contrast enhanced magnetic resonance scanning as a predictor of response to accelerated radiotherapy for advanced head and neck cancer. Br. J. Radiol.**72**: 1093-1098.

Hulka C.A., Edmister W.B., Smith B.L., et al. (1997). Dynamic echo-planar imaging of the breast: experience in diagnosing breast carcinoma and correlation with tumor angiogenesis. Radiology **205**: 837-842.

Ibrahim T.S., Lee R., Abduljalil A.M., et al. (2001). Dielectric resonances and B(1) field inhomogeneity in UHFMRI: computational analysis and experimental findings. Magn. Reson. Imaging **19**: 219-226.

Isebaert S., De Keyzer F., Haustermans K., et al.. (2011). Evaluation of semi-quantitative dynamic contrast enhanced MRI parameters for prostate cancer in correlation to whole-mount histopathology. Eur. J. Radiol. In press.

Jackson A., O'Connor J.P.B., Parker G.J.M., et al. (2007). Imaging tumor vascular heterogeneity and angiogenesis using dynamic contrast-enhanced magnetic resonance imaging. Clin. Cancer Res. **13**: 3449-3459.

Jansen J.F., Schöder H., Lee N.Y., et al. (2010). Noninvasive assessment of tumor microenvironment using dynamic contrast-enhanced magnetic resonance imaging and 18F-fluoromisonidazole positron emission tomography imaging in neck nodal metastases. Int. J. Radiat. Oncol. Biol. Phys. **77**: 1403-1410.

Jarnagin W.R., Schwartz L.H., Gultekin D.H., et al. (2009). Regional chemotherapy for unresectable primary liver cancer: results of a phase II clinical trial and assessment of DCE-MRI as a biomarker of survival. Ann. Oncol. **20**: 1589-1595.

Johansen R., Jensen L.R., Rydland J., et al. (2009). Predicting survival and early clinical response to primary chemotherapy for patients with locally advanced breast cancer using DCE-MRI. J. Magn. Reson. Imaging **29**: 1300-1307.

Juan C.J., Chen C.Y., Jen Y.M., et al. (2009). Perfusion characteristics of late radiation injury of parotid glands: quantitative evaluation with dynamic contrast-enhanced MRI. Eur. Radiol. **19**: 94-102.

Judd R.M., Atalay M.K., Rottman G.A., et al. (1995). Effects of myocardial water exchange on T1 enhancement during bolus administration of MR contrast agents. Magn. Reson. Med. **33**: 215-223.

Kam M.K., Leung S.F., Zee B., et al. (2007). Prospective randomized study of intensity-modulated radiotherapy on salivary gland function in early-stage nasopharyngeal carcinoma patients. J. Clin. Oncol. 31: 4873-4879.

Kim S., Loevner L.A., Quon H., et al. (2010). Prediction of response to chemoradiation therapy in squamous cell carcinomas of the head and neck using dynamic contrast-enhanced MR imaging. Am. J. Neuroradiol. **31**: 262-268.

Kim S., Quon H., Loevner L.A., et al. (2007). Transcytolemmal water exchange in pharmacokinetic analysis of dynamic contrast-enhanced MRI data in squamous cell

carcinoma of the head and neck. J. Magn. Reson. Imaging. **26**: 1607-1617.

Knopp M.V., Weiss E., Sinn H.P., et al. (1999). Pathophysiologic basis of contrast enhancement in breast tumors. J. Magn. Reson. Imaging **10**: 260-266.

Koch W.M., Brennan J.A., Zahurak M., et al. (1996). p53 Mutation and locoregional treatment failure in head and neck squamous cell carcinoma. J. Natl. Cancer Inst. **88**: 1580-1586.

Konings A.W., Faber H., Cotteleer F., et al. (2006). Secondary radiation damage as the main cause for unexpected volume effects: a histopathologic study of the parotid gland. Int. J. Radiat. Oncol. Biol. Phys. **64**: 98-105.

Konouchi H., Asaumi J., Yanagi Y., et al. (2003). Evaluation of tumor proliferation using dynamic contrast enhanced-MRI of oral cavity and oropharyngeal squamous cell carcinoma. Oral Oncol. **39**:290-295.

Kozlowski P., Chang S.D., Meng R., et al. (2010). Combined prostate diffusion tensor imaging and dynamic contrast enhanced MRI at 3T-quantitative correlation with biopsy. Magn. Reson. Imaging **28**: 621-628.

Laking G.R., West C., Buckley D.L., et al. (2006). Imaging vascular physiology to monitor cancer treatment. Crit. Rev. Oncol. Hematol. **58**: 95-113.

Lavini C., Verhoeff J.J.. (2010). Reproducibility of the gadolinium concentration measurements and of the fitting parameters of the vascular input function in the superior sagittal sinus in a patient population. Magn. Reson. Imaging. **28**: 1420-1430.

Leach M.O., Brindle K.M., Evelhoch J.L., et al. (2005). The assessment of antiangiogenic and antivascular therapies in early-stage clinical trials using magnetic resonance imaging: issues and recommendations. Br. J. Cancer. **92**: 1599-1610.

Lee F.K., Yeung D.K., King A.D., et al. (2005). Segmentation of nasopharyngeal carcinoma (NPC) lesions in MR images. Int. J. Radiat. Oncol. Biol. Phys. **61**: 608-620.

Li Y.H., Hu C.F., Qiong Q., et al. (2008). Elevated expressions of surviving and VEGF protein are strong independent predictors of survival in advanced nasopharyngeal carcinoma. J. Transl. Med. **6**: 1.

Loiselle C.R., Eby P.R., Peacock S., et al., (2011). Dynamic contrast enhanced magnetic resonance imaging and invasive breast cancer: primary lesion kinetics correlated with axillary lymph node extracapsular extension. J. Magn. Reson. Imaging. **33**: 96-101.

Lombaert I.M.A., Brunsting J.F., Wierenga P.K., et al. (2008). Rescue of Salivary Gland Function after Stem Cell Transplantation in Irradiated Glands. PLoS ONE **4**: e2063.

Machiels J.P., Henry S., Zanetta S., et al. (2010). Phase II study of sunitinib in recurrent or metastatic squamous cell carcinoma of the head and neck: GORTEC 2006-01. J. Clin. Oncol. **28**:21-28.

Mainou-Fowler T., Angus B., Miller S., et al. (2006). Micro-vessel density and the expression of vascular endothelial growth factor (VEGF) and platelet-derived endothelial cell growth factor (PdEGF) in classical Hodgkin lymphoma (HL). Leukemia & Lymphoma. **47**: 223-230.

Marcus C.D., Marcus V.L., Cucu C., et al. (2009). Imaging techniques to evaluate the response to treatment in oncology: Current standards and perspectives. Crit. Rev. Oncol. Hematol. **72**: 217–238.

Marsh R.E., Riauka T.A., McQuarrie S.A.. (2007). Use of a simulated annealing algorithm to fit compartmental models with an application to fractal pharmacokinetics. J. Pharm. Pharm. Sci. **10**: 168-179.

Martí-Bonmatí, Sanz-Requena, Alberich-Bayarri. (2008). Pharmacokinetic MR analysis of the cartilage is influenced by field strength. Eur. J. Radiol. **67**: 448-452.

Menda Y., Ponto B.L.L., Dornfeld K.J., et al. (2009). Kinetic analysis of 3′-deoxy-3′-1^{8}F-fl uorothymidine (1^{8}F-FLT) in head and neck cancer patients before and early after initiation of chemoradiation therapy. J. Nucl. Med. **50**: 1028–1035.

Mineta H., Miura K., Ogino T., et al. (2000). Prognostic value of vascular endothelial growth factor (VEGF) in head and neck squamous cell carcinomas. Br. J. Cancer **83**: 775–781.

Murase K. (2004). Efficient method for calculating kinetic parameters using T1-weighted dynamic contrast-enhanced magnetic resonance imaging. Magn. Reson.

Med. 51: 858-862.

Nehmeh S.A., Lee N.Y., Schroder H., et al. (2008). Reproducibility of intratumor distribution of 18F-fluoromisonidazole in head and neck cancer. Int. J. Radiat. Oncol. Biol. Phys. **70**: 235–242.

Newbold K., Castellano I., Charles-Edwards E., et al. (2009). An exploratory study into the role of dynamic contrast-enhanced magnetic resonance imaging or perfusion computed tomography for detection of intratumoral hypoxia in head-and-neck cancer. Int. J. Radiat. Oncol. Biol. Phys. **74**: 29-37.

Ng Q.S., Goh V., Milner J., et al. (2007). Acute tumor vascular effects following fractionated radiotherapy in human lung cancer: in vivo whole tumor assessment using volumetric perfusion computed tomography. Int. J. Radiat. Oncol. Biol. Phys. **67**: 417–424.

Noworolski S.M., Fischbein N.J., Kaplan M.J., et al. (2003). Challenges in dynamic contrast-enhanced MRI imaging of cervical lymph nodes to detect metastatic disease. J. Magn. Reson. Imaging. **17**: 455-462.

Oberholzer K., Pohlmann A., Schreiber W., et al. (2008). Assessment of tumor microcirculation with dynamic contrast-enhanced MRI in patients with esophageal cancer: initial experience. J. Magn. Reson. Imaging. **27**: 1296-1301.

Oghabian M.A., Gharehaghaji N., Amirmohseni S., et al. (2010). Detection sensitivity of lymph nodes of various sizes using USPIO nanoparticles in magnetic resonance imaging. Nanomedicine **6**: 496-499.

Oysu S.A., Ayanoglu E., Kodalli N., et al. (2005). Dynamic contrast-enhanced MRI in the differentiation of posttreatment fibrosis from recurrent carcinoma of the head and neck. Clin. Imaging. **29**:307-312.

Padhani A.R., Hayes C., Landau S., et al. (2002). Reproducibility of quantitative dynamic MRI of normal human tissues. NMR Biomed. **15**: 143-153.

Pan J., Kong L., Lin S., et al. (2008). The clinical significance of coexpression of cyclooxygenases-2, vascular endothelial growth factors, and epidermal growth factor receptor in nasopharyngeal carcinoma. Laryngoscope **118**: 1970- 1975.

Peruzzo D., Bertoldo A., Zanderigo F., et al.. (2011). Automatic selection of arterial

input function on dynamic contrast-enhanced MR images. Comput Methods Programs Biomed. In press.

Pickles M.D., Lowry M., Manton D.J., et al. (2005). Role of dynamic contrast enhanced MRI in monitoring early response of locally advanced breast cancer to neoadjuvant chemotherapy. Breast Cancer Res. Treat. **91**: 1-10.

Prescott J.W., Zhang D., Wang J.Z., et al. (2010). Temporal analysis of tumor heterogeneity and volume for cervical cancer treatment outcome prediction: preliminary evaluation. J. Digit. Imaging **23**: 342-357.

Purcell E.M. (1946). Resonance absorption by nuclear magnetic moments in solid. Phy. Rev. **69**: 37

Ridge J.A., Glisson B.S., Lango M.N., et al. Cancer Management: A Multidisciplinary Approach. UBM Medica, 13rd ed. (2011).

Roerts C., Issa B., Stone A., et al. (2006). Comparative study into the robustness of compartmental modeling and model-free analysis in DCE-MRI studies. J. Magn. Reson. Imaging **23**: 554 563.

Roberts C., Little R., Watson Y., et al. (2011). The effect of blood inflow and B1-field inhomogeneity on measurement of the arterial input function in axial 3D spoiled gradient echo dynamic contrast-enhanced MRI. Magn. Reson. Med. **65**: 108-119.

Rose C.J., Mills S.J., O'Connor J.P., et al. (2009). Quantifying spatial heterogeneity in dynamic contrast-enhanced MRI parameter maps. Magn. Reson. Med. **62**: 488-499.

Sansone M., Fusco R., Petrillo A., et al, 2011. An expectation-maximisation approach for simultaneous pixel classification and tracer kinetic modelling in dynamic contrast enhanced-magnetic resonance imaging. Med. Biol. Eng. Comput. 49: 485-495.

Sawatsubashi M., Yamada T., Fukushima N., et al. (2000). Association of vascular endothelial growth factor and mast cells with angiogenesis in laryngeal squamous cell carcinoma. Virchows Arch. **436**: 243–248.

Schabel M.C. and Parker D.L., (2008). Uncertainty and bias in contrast concentration

measurements using spoiled gradient echo pulse sequences. Phys. Med. Biol. **53**: 2345–2373.

Senger D.R., Water L.V.D., Brown L.E., et al. (1993). Vascular permeability factor (VPF, VEGF) in tumor biology. Cancer and Metastasis Rev. **12**: 303-324.

Shukla-Dave A., Lee N., Stambuk H., et al. (2009). Average arterial input function for quantitative dynamic contrast enhanced magnetic resonance imaging of neck nodal metastases. BMC Med. Phys. **9**: 4.

St Lawrence K.S., Lee T.Y. (1998). An adiabatic approximation to the tissue homogeneity model for water exchange in the brain: I. Theoretical derivation. J. Cereb. Blood Flow Metab. **18**: 1365-1377.

Stephens L.C., Ang K.K., Schultheiss T.E., et al. (1986). Target cell and mode of radiation injury in rhesus salivary glands. Am. J. Pathol. **124**: 469-478.

Teshima K., Murakami R., Tomitaka E., et al. (2010). Radiation-induced Parotid Gland Changes in Oral Cancer Patients: Correlation Between Parotid Volume and Saliva Production. Jap. J. Clin. Oncol. **40**: 42-46.

Tezelman S., Giles Y., Tunca F., et al. (2007). Diagnostic value of dynamic contrast medium enhanced magnetic resonance imaging in preoperative detection of thyroid carcinoma. Arch Surg. **142**: 1036-1041.

Tofts P.S., Brix G., Buckley D.L., et al. (1999). Estimating kinetic parameters from dynamic contrast-enhanced T1-weighted MRI of a diffusible tracer: standardized quantities and symbols. J. Magn. Reson. Imaging **10**: 223-232.

Tofts P.S., Kermode A.G. (1991). Measurement of the blood-brain barrier permeability and leakage space using dynamic MR imaging: Fundamental concepts. Magn. Reson. Med. **17**: 357-367.

Tokuda J., Mamata H., Gill R.R., et al. (2011). Impact of nonrigid motion correction technique on pixel-wise pharmacokinetic analysis of free-breathing pulmonary dynamic contrast-enhanced MR imaging. J. Magn. Reson. Imaging. **33**:968-973.

Tomura N., Omachi K., Sakuma I., et al. (2005). Dynamic contrast-enhanced magnetic resonance imaging in radiotherapeutic efficacy in the head and neck tumors. Am. J. Otolaryngol. **26**:163-167.

Tunca F., Giles Y., Salmaslioglu A., et al. (2007). The preoperative exclusion of thyroid carcinoma in multinodular goiter: Dynamic contrast-enhanced magnetic resonance imaging versus ultrasonography-guided fine-needle aspiration biopsy. Surgery. **142**: 992-1002.

Tuncbilek N., Tokatli F., Altaner S., et al. (2011). Prognostic value DCE-MRI parameters in predicting factor disease free survival and overall survival for breast cancer patients. Eur. J Radiol. In press.

Turnbull L.W. (2009). Dynamic contrast-enhanced MRI in the diagnosis and management of breast cancer. NMR Biomed. **22**: 28-39.

Unetsubo T., Konouchi H., Yanagi Y., et al. (2009). Dynamic contrast-enhanced magnetic resonance imaging for estimating tumor proliferation and microvessel density of oral squamous cell carcinomas. Oral Oncol. **45**: 621-626.

Van Cann E.M., Rijpkema M., Heerschap A., et al. (2008). Quantitative dynamic contrast-enhanced MRI for the assessment of mandibular invasion by squamous cell carcinoma. Oral Oncol. **44**: 1147-1154.

Vipa B., Boonchu K., Juvady L., et al. (2008). Vascular endothelial growth factor A and proliferation marker in prediction of lymph node metastasis in oral and pharyngeal squamous cell carcinoma. Arch. Otolaryngol. Head Neck Surg. **134**: 1305–1311.

Wada A., Uchida N., Yokokawa M., et al. (2009). Radiation-induced xerostomia: objective evaluation of salivary gland injury using MR sialography. Am. J. Neuroradiol. 30: 53-58.

Wang H.Z., Riederer S.J., Lee J.N.. (1987) Optimizing the precision in T1 relaxation estimation using limited flip angles. Magn. Reson. Med. **5**: 399-416.

Wang Y., Huang W., Panicek D.M., et al. (2008). Feasibility of using limited-population-based arterial input function for pharmacokinetic modeling of osteosarcoma dynamic contrast-enhanced MRI data. Magn. Reson. Med. **59**: 1183-1189.

Yang B.T., Wang Z.C., Xian J.F., et al. (2009). Leiomyoma of the sinonasal cavity: CT and MRI findings. Clin. Radiol. **64**: 1203-1209.

Yang C., Karczmar G.S., Medved M., et al. (2009). Reproducibility assessment of a multiple reference tissue method for quantitative dynamic contrast enhanced-MRI analysis. Magn. Reson. Med. **61**: 851-859.

Yue C., Li D., Shen Z., et al. (2010). Sensitivity of Quantitative Metrics Derived from DCE MRI and a Pharmacokinetic Model to Image Quality and Acquisition Parameters. Acad. Radiol. **17**: 468-478.

Yuh W.T., Mayr N.A., Jarjoura D., et al. (2009). Predicting control of primary tumor and survival by DCE MRI during early therapy in cervical cancer. Invest. Radiol. **44**: 343-350.

Zahra M.A., Hollingsworth K.G., Sala E., et al. (2007). Dynamic contrast-enhanced MRI as a predictor of tumor response to radiotherapy. Lancet Oncol. **8**: 63-74.

Zahra M.A., Tan L.T., Priest A.N., et al. (2009). Semiquantitative and quantitative dynamic contrast-enhanced magnetic resonance imaging measurements predict radiation response in cervix cancer. *Int. J. Radiat. Oncol. Biol. Phys.* **74**:766-773.

Zhu X.P., Li K.L., Kamaly-Asl I.D., et al. (2000). Quantification of endothelial permeability, leakage space, and blood volume in brain tumors using combined T1 and T2* contrast enhanced dynamic MR imaging. J. Magn. Reson. Imaging. **11**: 575-585.

PUBLICATIONS AND CONFERENCE PROCEEDINGS

The following publications are derived from the work of this thesis:

Journal Publications

1. Lee F.K.H., King A.D., Kam M.K.M., et al. (2011). Radiation injury of the parotid glands during treatment for head and neck cancer: Assessment using Dynamic Contrast-enhanced MR imaging. Radiat Res. 175: 291-296.
2. Lee F.K.H., King A.D., Yeung D.K.W., et al. (2011). Dynamic contrast enhancement magnetic resonance imaging (DCE-MRI) for differential diagnosis in head and neck cancers. Accepted by Eur. J. Radiol.
3. Lee F.K.H., King A.D., Chow S.K.K., et al. (2011). Dynamic contrast enhanced magnetic resonance imaging (DCE-MRI) a pilot study for early prediction of treatment failure in head and neck squamous cell carcinomas. Submitted to Am. J. Roent.

Conference Proceedings

1. Monitoring therapeutic effect of cetuximab in the treatment of nasopharyngeal carcinoma by DCE-MRI. International Society for Magnetic Resonance in Medicine (ISMRM) Annual Meeting 2008, Toronto, Canada

2. Dynamic contrast enhancement (DCE) MRI of parotid glands after radiotherapy. International Society for Magnetic Resonance in Medicine (ISMRM) Annual Meeting 2009, Hawaii, USA

3. Dynamic contrast enhanced magnetic resonance imaging analysis of different head and neck cancers. International Society for Magnetic Resonance in Medicine (ISMRM) Annual Meeting 2009, Hawaii, USA

Monitoring therapeutic effect of cetuximab in the treatment of nasopharyngeal carcinoma by DCE-MRI

F. K. Lee[1], B. Ma[2], D. K. Yeung[1], and A. D. King[1]

[1]Department of diagnostic radiology and organ imaging, the Chinese University of Hong Kong, Hong Kong, China, People's Republic of, [2]Department of clinical oncology, the Chinese University of Hong Kong, Hong Kong, China, People's Republic of

Background

Dynamic contrasted enhanced MRI (DCE-MRI) is becoming a popular technique to evaluate the therapeutic effect of anti-angiogenic and anti-vascular drugs for the treatment of cancers. The potential of DCE-MRI to predict treatment outcome is attractive as it can provide valuable information for treatment planning. In this study, we attempted to use this technique to monitor the therapeutic effect of cetuximab (Merck KgaA, Darmstadt, Germany), an epidermal growth factor receptor (EGFR) inhibitor, in the treatment of nasopharyngeal carcinoma (NPC). The effect of this drug in combination with chemotherapy for NPC has been published[2,3], while this report describes the preliminary attempt to examine the potential of the DCE technique in the early detection of drug response.

Method

A total of 11 NPC patients underwent two DCE-MRI scans: 1 week before the commencement of cetuximab treatment and 1 week after, using a 1.5T Intera NT scanner (Philips Medical Systems, Best, the Netherlands) with a head and neck coil. The scanning parameters of the sequences used are shown in Table 1.

Scan	TR/TE/α (msec/°)	Matrix	Δt (sec)	T_a (min)
3D T1W FFE 2 AXIAL	2.7/0.9/2	128x128x25	-	-
3D T1W FFE 10 AXIAL	2.7/0.9/10	128x128x25	-	-
3D T1W FFE 20 AXIAL	2.7/0.9/20	128x128x25	-	-
3D T1W FFE 30 AXIAL	2.7/0.9/30	128x128x25	-	-
3D T1W FFE 20 DYN AXIAL	2.7/0.9/20	128x128x25x106	3.5	6.2
T1W+C SE AXIAL	482/12/-	512x512x30	-	-

Table 1: MRI scan parameters.

Patients were administered with a single dose of gadolinium (Dotarem, Guerbet, France) by bolus injection using a power injector. T1 maps were derived from the four sets of FFE images. The dynamic contrast concentration curves of each pixel were derived from the dynamic FFE images using the Ernst formula. The two compartment model proposed by Tofts et al[4,5] was used to derive the dynamic parameter maps of Ktrans, ve and vp. The area under the contrast concentration curve at the initial 60 and 90 seconds (AUC60, AUC90) of the dynamic scans were also obtained. The primary lesions were contoured on the T1W+C SE image by an experienced head and neck radiologist, and the averages of the acquired parameters within the lesions were obtained.

Results

The mean and standard deviation of the DCE parameters and the absolute percentage change of NPC before and after treatment are shown in Table 2 and 3, respectively.

Ktrans (ml/ml/min)	ve	vp	AUC60 (mM sec)	AUC90 (mM sec)
1.54 ± 0.86	0.7 ± 0.21	0.19 ± 0.15	1977.2 ± 471.4	4728.8 ± 860.3

Table 2: mean and standard deviation of the DCE parameters for primary NPC before cetaximab.

	Tumor size	Ktrans	ve	vp	AUC60	AUC90
Absolute % change	9.7 ± 6.8	91.8 ± 88.8	34.7 ± 33.4	165.7 ± 325.2	27.9± 30.4	21.6 ± 25.2

Table 3: Absolute percentage change in the studied parameters after cetaximab.

A substantial change was observed in the dynamic parameters of Ktrans, ve, vp, AUC60 and AUC90. At the same time no substantial change in lesion size was observed in any of the 11 patients. The absolute percentage difference in lesion volumes between the two scans was 9.7±6.8%.

Conclusions

We report the DCE parameters of primary NPC lesions. We observed a substantial amount of change in the DCE parameters after commencement of cetuximab treatment. Although the reproducibility of the parameters has to be verified in further studies, these substantial changes in the parameters, which precede tumor shrinkage, reveal the potential to use DCE-MRI to monitor therapeutic effect of the drug from the perspective of vascular dynamics. The usefulness of the result relies on the long term study on the predictability of the parameters on the treatment outcome.

References

1. Evelhoch J, Brown T, Chenevert T et al. Consensus recommendation for acquisition of dynamic contrasted enhanced MRI data in oncology. *Proc Int Soc Magn Reson Med Eighth Scientific Meeting and Exhibition*, p.1439
2. Chan AT, Hsu MM, Goh BC et al. Multicenter, phase II study of cetuximab in combination with carboplatin in patients with recurrent or metastatic nasopharyngeal carcinoma. *J Clin Oncol.* 2005; 23: 3568-3576
3. Sung FL, Poon TC, Hui EP et al. Antitumor effect and enhancement of cytotoxic drug activity by cetuximab in nasopharyngeal carcinoma cells. *In Vivo.* 2005; 19: 237-245.
4. Tofts PS and Kermode AG. Measurement of the blood brain barrier permeability and leakage space using dynamic MR imaging. 1. Fundamental concepts. *Magn Reson Med.* 1991; 17: 357-367
5. Tofts PS, Brix G, Buckley DL et al. Estimating kinetic parameters from dynamic contrast-enhanced T1 weighted MRI of a diffusable tracer: standardized quantities and symbols. *J Magn Reson Imaging* 1999; 10: 223-232

2201

Dynamic contrast enhanced magnetic resonance imaging analysis of different head and neck cancers

K-H. Lee[1], A. D. King[1], K-W. Yeung[1], B-Y. Ma[2], K-H. Yu[2], K. Bhatia[1], and A. Ahuja[1]

[1]Department of Diagnostic Radiology and Organ Imaging, Prince of Wales Hospital, The Chinese University of Hong Kong, Hong Kong, Hong Kong SAR, China, People's Republic of, [2]Department of Clinical Oncology, the Chinese University of Hong Kong, Prince of Wales Hospital, The Chinese University of Hong Kong, Hong Kong, Hong Kong SAR, China, People's Republic of

Objective: The aim of the study was to determine the characteristics of three head and neck cancers on dynamic contrast enhanced magnetic resonance imaging (DCE-MRI) and to determine if there are any significant differences between them.

Method: 54 cancer patients with head and neck cancers comprising of undifferentiated nasopharyngeal carcinoma (UD) (n= 22), squamous cell carcinoma (SCC) (n = 24) and lymphoma (n = 8) underwent DCE-MRI in a 1.5T scanner before treatment. The DCE-MRI protocol included gradient echo acquisitions (TR/TE = 2.7/0.9ms, 128 x 128 matrix, 25 slices, slice thickness = 4mm, FOV = 23 x 23cm, NSA = 1) with different flip angles (2/10/20/30) for T1 determination. It also included dynamic gradient echo acquisition with similar parameters and flip angle of 20, time resolution of 3.5 sec for 371 sec. Contrast agent (Dotarem, Guerbet, France) was injected into the patients at 20 sec after start of the dynamic scan with a power injector at a speed of 3ml/sec. Pharmacokinetic models were employed for analysis, yielding parameters of k_{trans}, v_p and ve from the Tofts model[1], A, k_{el} and k_{21} from the Brix model[2]. Semi-quantitative analysis was also performed, generating parameters of area under curve of the initial 60 seconds and 90 seconds (AUC60 and AUC90 respectively), peak enhancement and time to peak. The means of the DCE parameters in the three groups of lesions were tested for any significant difference using one-way ANOVA with Bonferroni correction.

Results: The DCE parameters of the different types of head and neck malignancies are tabulated below:

		UD	SCC	Lymphoma
Tofts	k_{trans} (1/min)	1.197 ± 0.577	0.739 ± 0.415	0.591 ± 0.179
	v_e	0.665 ± 0.152	0.632 ± 0.134	0.535 ± 0.174
	v_p	0.093 ± 0.106	0.073 ± 0.049	0.069 ± 0.033
Brix	A (arb. Unit)	50.046 ± 12.381	38.955 ± 11.664	37.125 ± 6.081
	k_{el} (x 10^{-2}/sec)	0.386 ± 0.086	0.501 ± 0.207	0.465 ± 0.251
	k_{21} (x 10^{-1}/sec)	0.235 ± 0.018	0.221 ± 0.022	0.221 ± 0.017
Semi-quantitative	AUC60 (norm. unit)	0.306 ± 0.106	0.225 ± 0.103	0.205 ± 0.054
	AUC90 (norm. unit)	0.743 ± 0.279	0.538 ± 0.206	0.499 ± 0.093
	Peak enhancement (arb. unit)	2.660 ± 0.483	2.666 ± 0.754	2.465 ± 0.133
	Time to peak (sec)	94.5 ± 72.1	119 ± 70	150.5 ± 102.9

* AUC60 and AUC90 are normalized to that of the carotid artery

There was a significant difference between UD and SCC in the k_{trans}, AUC 60, AUC90 and A ($p< 0.01$) and between UD and lymphoma k_{trans}, AUC 60 and AUC90 ($p< 0.01$) and A ($p< 0.05$), but no significant difference between SCC and lymphoma.

Conclusion: There is a significant difference in DCE-MRI parameters of head and neck cancers which has the potential to allow MRI to discriminate between NPC and SCC or lymphoma, but not between lymphoma and SCC. Further studies are required to determine the physiological basis for these differences.

Acknowledgement

We are like to express our gratitude to Dr. David Buckley for his advice in the DCE analysis of the data.

Reference

1. Brix G, Semmler W, Port R et al. *J Comput Assist Tomogr* 1991 (15): 621-628.
2. Tofts PS, Kermode AG. *Magn Reson Med* 1991 (17): 357-367.

Dynamic contrast enhancement (DCE) MRI of parotid glands after radiotherapy

K-H. Lee[1], K-W. Yeung[1], K-M. Kam[2], B-Y. Ma[2], A. D. King[1], K-H. Yu[2], C. Hu[1], and A. Ahuja[1]

[1]Department of Radiology and Organ Imaging, Prince of Wales Hospital, The Chinese University of Hong Kong, Hong Kong, Hong Kong SAR, China, People's Republic of, [2]Department of Clinical Oncology, Prince of Wales Hospital, The Chinese University of Hong Kong, Hong Kong, Hong Kong SAR, China, People's Republic of, [3]Shenzhen Fifth Hospital and Luo-hu District Hospital, Shenzhen, Guangdong, China, People's Republic of

Introduction: Radiation injury occurs in the parotid glands of patients being irradiated for head and neck cancer. Increased contrast enhancement in MRI of parotid glands after radiotherapy has been reported[1] and so to improve the understanding of radiation injury we studied further these changes in contrast enhancement using dynamic contrast enhancement MRI (DCE-MRI).

Method: Eighteen nasopharyngeal carcinoma patients underwent DCE-MRI in a 1.5T scanner (Intera, Philips Medical Systems, Best, the Netherlands) before and at 3 months after completion of radiotherapy. The DCE-MRI protocol included gradient echo acquisitions (TR/TE = 2.7/0.9ms, 128 x 128 matrix, 25 slices, slice thickness = 4mm) with different flip angles (2/10/20/30) for T1 determination, dynamic gradient echo images with time resolution of 3.5 sec for 371 sec. Contrast agent (Dotarem, Guerbet, France) was injected into the patients at 20 sec after start of dynamic scan with a power injector at 3ml/sec. These patients received intensity modulated radiotherapy and the mean radiation doses received by parotid glands were recorded. Data were analyzed using two pharmacokinetic models from Tofts[2] and Brix[3] and semi-quantitative analysis. Correlation on the percentage change of parameter means pre- and post treatment with the mean parotid dose was conducted using two-tailed Pearson test.

Results: The result of the correlation tests and the plots of the significantly correlated parameters are shown below.

	% change in parameter	p-value	R square
Tofts	k_{trans}	0.0014**	0.2639
	v_e	0.0053**	0.2069
	v_p	0.4516	0.0017
Brix	A	.0.0021**	0.2593
	k_{21}	0.9213	0.0003
	k_{21}	0.3005	0.0335
Semi-quantitative	AUC60	0.0066*	0.1973
	Peak enhancement	0.7172	0.0039
	Time to peak	0.9709	0.0000

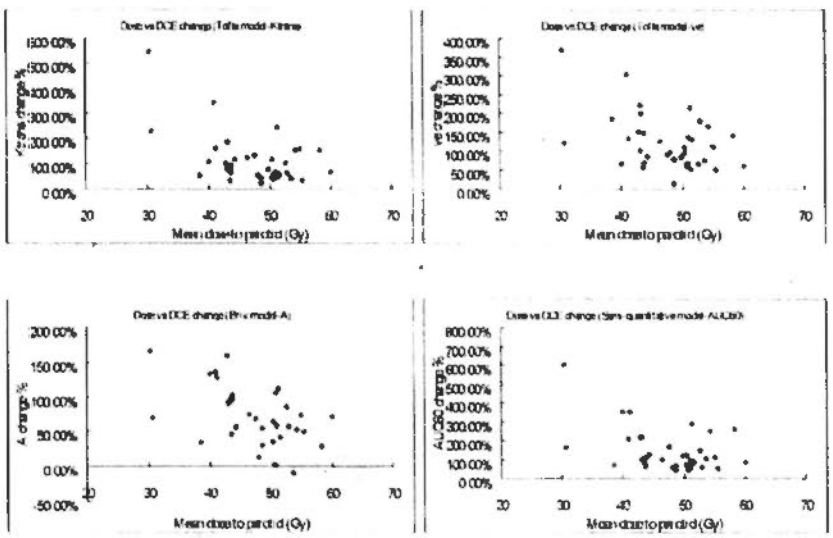

* marginally significant ** significant (with Bonferroni correction)

Discussions & Conclusions: Significant correlation was shown between radiation dose to the parotid and percentage change in the k_{trans}, v_e, A, and AUC60. These four parameters showed an increase after treatment, but the percentage change showed an inverse relationship to the dose. It has been shown in previous reports[4,5] that permeability in tumors is increased at the beginning of radiotherapy, due to the disruption of normal endothelium and inflammation. Ultimately, radiation damages the vessels and reduces permeability and vascular density. No study has yet demonstrated similar time course of events in parotid glands, but the current data suggests that the former effect may be more prominent with exposure to lower radiation dose, while a larger radiation dose may induce a greater and earlier manifestation of the latter effect in this organ. Increase in v_e is probably related to the increase in extra-cellular extra-vascular space (EES) after serous acinar cell loss and edema. A previous report has shown that higher radiation doses induce more atrophy in parotid glands[6], which may reduce the intracellular space within. This may explain the inverse relationship of the change in v_e with radiation dose.

Acknowledgement: We would like to express our gratitude to Dr. David Buckley for his advice in the DCE analysis of the data.

Reference:

1.Juan CJ, et al. *Eur Radiol.* 2008. 2.Brix G, et al. *J Comput Assist Tomogr* 1991 (15): 621-628. 3.Tofts PS, Kermode AG. *Magn Reson Med* 1991 (17): 357-367. 4.de Vries A, et al. *Radiology* 2000 (217): 385-391. 5.Ng QS, et al. *Int J Radiat Oncol Biol Phys.* 2007 (67): 417-424. 6.LC Stephens, et al. *Am J Pathol* 1986 (124): 469-478.

RADIATION RESEARCH 175, 291–296 (2011)
0033-7587/11 $15.00

DOI: 10.1667/RR2370.1

Radiation Injury of the Parotid Glands During Treatment for Head and Neck Cancer: Assessment Using Dynamic Contrast-Enhanced MR Imaging

Francis Kar-ho Lee,[a,1] Ann Dorothy King,[a] Michael Koon-ming Kam,[b] Brigette Buig-yue Ma[b] and David Ka-wai Yeung[a]

[a] *Department of Diagnostic Radiology and Organ Imaging, Prince of Wales Hospital, the Chinese University of Hong Kong, Hong Kong SAR; and* [b] *Department of Clinical Oncology, Prince of Wales Hospital, the Chinese University of Hong Kong, Hong Kong SAR*

Lee, F. K., King, A. D., Kam, M. K., Ma, B. B. and Yeung, D. K. Radiation Injury of the Parotid Glands During Treatment for Head and Neck Cancer: Assessment Using Dynamic Contrast-Enhanced MR Imaging. *Radiat. Res.* 175, 291–296 (2011).

The parotid gland is an important organ at risk of complications of radiotherapy for head and neck cancer. In this study, we examined the potential of dynamic contrast-enhanced magnetic resonance imaging (DCE-MRI) for assessment of radiation injury to the parotid glands. DCE-MRI was performed before and 3 months after radiotherapy in patients treated for head and neck cancer. DCE-MRI was analyzed using the pharmacokinetic model proposed by Tofts and Kermode to produce three DCE parameters: k_{trans}, v_e and v_p. These parameters were correlated with the dose of radiation delivered to the parotid glands and the degree of radiation-induced parotid atrophy. The mean radiation dose received by the parotid glands was 47.1 ± 6.6 Gy. All patients received concurrent chemotherapy. There was a significant rise in all three parameters after therapy ($P < 0.0001$). Baseline v_e and v_p and the post-treatment rise in v_e correlated with parotid gland atrophy ($P = 0.0008$, 0.0003 and 0.0022, respectively). DCE-MRI has the potential to be used as a non-invasive technique for predicting and assessing radiation injury in the parotid glands. © 2011 by Radiation Research Society

INTRODUCTION

The parotid glands lie within or close to the radiation field of many head and neck cancers, and hence these glands are often unavoidably irradiated during radiation treatment. Radiation injury to the parotid glands induces xerostomia, which has a significant impact on the patient's quality of life. New developments in radiotherapy have focused on using techniques such as conformal radiotherapy and intensity-modulated radiotherapy (IMRT) to reduce the radiation dose to the parotid glands while at the same time delivering sufficient dose to the cancer targets (*1, 2*).

However, even with these newer techniques, it is not always possible to prevent the glands from receiving a significant radiation dose. There is therefore interest in finding other strategies for better protection of the organ. These require an understanding of radiation-induced damage on a cellular level. Histological studies have been conducted in rats and rhesus monkeys that showed inflammation, edema, acinar cell degeneration and necrosis, vessel damage and organ atrophy after irradiation (*3, 4*). Similar studies are more difficult to perform on human subjects due to the invasive nature of obtaining parotid tissue samples and inability to examine the whole gland. Therefore, an *in vivo* tool to monitor radiation damage in the parotid gland on the cellular and vascular level would be valuable.

Dynamic contrast-enhanced magnetic resonance imaging (DCE-MRI) is a functional imaging technique that provides information on tissue perfusion through dynamic contrast analysis by compartment modeling or curve fitting. DCE parameters obtained using pharmacokinetic models such as those proposed by Tofts and Kermode (*5*) provide data that can reflect physiological processes such as vascularity, vessel permeability and cellularity of the examined tissue. This technique has been applied to the diagnosis, prognosis and evaluation of treatment response in cancers of the breast (*6, 7*) and prostate (*8, 9*), and efforts have been made to extend its application to head and neck malignancies (*10–12*). DCE-MRI also has the potential to yield valuable *in vivo* information on the damage that occurs in organs that are irradiated and to provide a non-invasive method for studying the irradiated parotid glands. The focus of this study was to use DCE-MRI to determine whether radiation exposure leads to any changes in the DCE parameters and if so to determine whether there is any correlation with radiation dose and the degree of parotid gland atrophy.

[1] Address for correspondence: Rm 1214, Block R, Queen Elizabeth Hospital, Gascoigne Road, Kowloon, Hong Kong; e-mail: leekarhof@hotmail.com.

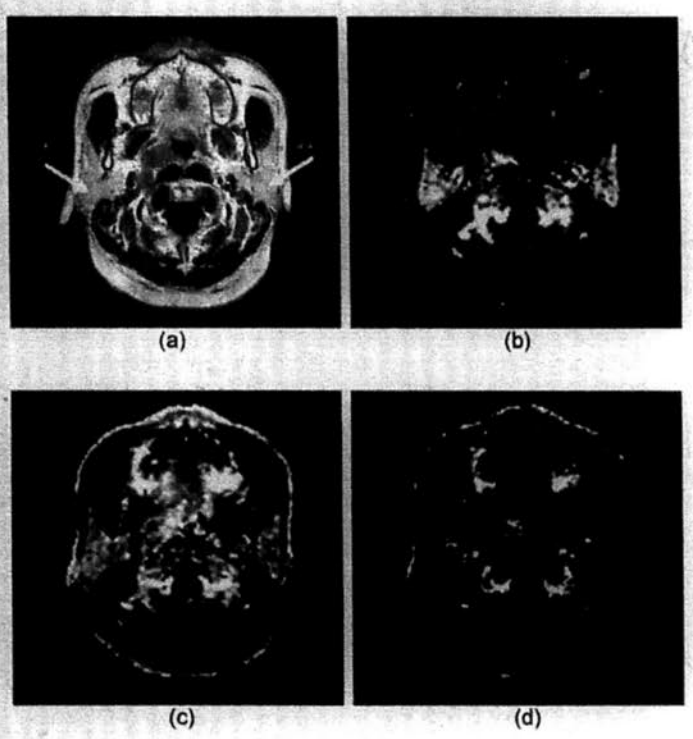

FIG. 1. Parameter maps of (panel a) T1W contrast-enhanced image, (panel b) k_{trans}, (panel c) v_e, and (panel d) v_p. *Right parotid gland, **left parotid gland.

MATERIALS AND METHODS

Patients

The DCE data were evaluated retrospectively in a cohort of patients undergoing radiotherapy for nasopharyngeal carcinoma (NPC) who had been recruited for another DCE-MRI study that was been performed with ethical approval from the local ethics committee and informed consent. All patients received baseline DCE-MRI before treatment and at 3 months after treatment. The mean radiation dose received by each parotid gland in each patient was obtained from the treatment planning records. Patients were treated with IMRT at a dose of 70 Gy to the gross tumor over a period of 7 weeks.

Image Acquisition

Patients were scanned in a 1.5-T MR scanner (Philips Medical System, Best, the Netherlands) with the head and neck SENSE coil. Images were acquired in the axial orientation from sphenoid sinus to approximately the C4 level. Four 3D T1-weighted gradient echo images were performed with different flip angles to generate the T1 map (repetition time, TR = 2.7 ms; echo time, TE = 0.9 ms; flip angle, α = 2, 10, 20, 30°; slice thickness, TH = 4 mm, matrix size = 128 × 128, field of view, FOV = 230 mm; number of acquisitions, NSA = 4). Dynamic gradient echo images were then acquired at a time resolution of 3.5 s for 106 times (repetition time, TR = 2.7 ms; echo time, TE = 0.9 ms; flip angle, α = 20°; slice thickness, TH = 4 mm, matrix size = 128 × 128, FOV = 230 mm; number of acquisitions, NSA = 1). The contrast agent (Dotarem, Guerbet, France) at a dose of 0.2 ml/kg was injected intravenously with a power injector at a rate of 3 ml/s, beginning at 20 s after the start of the dynamic sequence. Immediately after the injection, the same amount of saline was flushed into the syringe at the same injection rate.

Parotid Contouring

For each patient, both parotid glands were contoured on the FFE20 scan before and after treatment. A single observer (FKL) performed the contouring. Volume atrophy was defined as the percentage reduction in volume of the parotid gland after radiotherapy.

Image and Data Processing

Images were exported from the scanner console to an offline computer for processing with in-house developed software. The T1 map was calculated by the use of the gradient echo images with the Ernst formula. The contrast concentration map was then calculated according to details described by Zhu *et al.* (*13*). Analysis was based on the pharmacokinetic model described by Tofts and Kermode (*5*), which uses a two-compartment model to represent the dynamic transfer of contrast agent between the plasma and the extracellular-extravascular space (EES). Studies (*14*) suggest that the arterial input function (AIF) gives a representation of the contrast influx, and the internal carotid artery was delineated manually for each dynamic scan to obtain the AIF. This artery was chosen because it is a major arterial supply to the parotid gland and is large enough to avoid substantial partial volume effect. The term v_pC_p, representing the plasma contribution of contrast concentration, was also added in the calculation model.

The model expression is

$$\frac{dC_e}{dt} = k_{trans}(C_p - C_e), \tag{1}$$

$$C_t = C_e v_e + C_p v_p, \tag{2}$$

$$C_t(t) = k_{trans}\int_0^t C_p(t')e^{-\frac{k_{trans}}{v_e}(t-t')}dt' + v_pC_p(t), \tag{3}$$

where C_t, C_e and C_p are the contrast concentration of the total volume of tissue, EES and plasma, respectively.

Using this model, three parameters, k_{trans}, v_e and v_p, were estimated for every pixel using multiple-starting-point Marquardt-Levendag curve fitting (*15*). The parameter k_{trans} represents the permeability surface area product per unit volume of tissue, v_e represents the EES volume per unit volume of tissue, and v_p represents the blood plasma volume per unit volume of tissue. The mean DCE parameters of each of gland were obtained for analysis. Examples of the parameter images with the T1W contrast-enhanced image are shown in Fig. 1.

Statistical Analysis

The statistical analysis had three objectives. The first was to identify a significant change in any of the DCE parameters after radiotherapy using a paired t test. The second was to correlate any changes in DCE parameters with radiation dose. The third was to correlate baseline DCE parameters and postirradiation change in DCE parameters with parotid volume atrophy. For the last two objectives, Pearson's test was used to test for any significant correlations. P values were corrected by the Bonferroni method on multiple correlation tests. All statistical tests were conducted with the software PRISM (La Jolla, CA).

RESULTS

Patients

The study included 21 patients (16 males and 5 females with mean age 49 ± 10 years, range: 30–

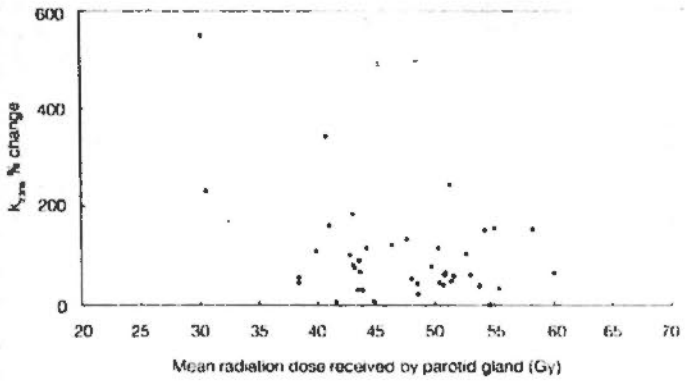

FIG. 2. Percentage change in k_{trans} as a function of radiation dose received by the parotid glands.

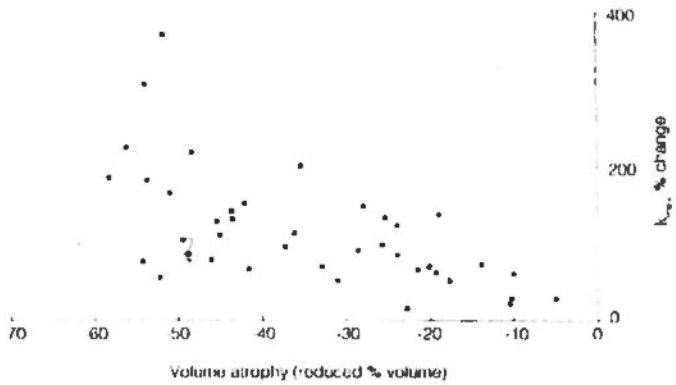

FIG. 3. Percentage change in v_e as a function of volume atrophy.

62 years), with 42 parotid glands for analysis. The mean radiation dose received by the parotid glands was 47.1 ± 6.6 Gy. Concurrent chemotherapy was also administered to the patients. The mean parotid gland atrophy was −32 ± 20%.

All AIFs extracted from the patients were visually inspected to contain clearly distinguishable first and second passes of contrast in the contrast concentration curve. This served as a quality assurance process to exclude artifacts in the arteries. Also, we examined the reproducibility of the AIF and obtained repeatability (variation with the 95% confidence interval) of about 30% for AUC60 and AUC90 of AIF. The induced variation in DCE parameters is significantly less than the change induced by radiation in this study.

DCE Parameters

The mean DCE parameters before radiotherapy (baseline) and after radiotherapy (3 months post-treatment) are shown in Table 1. All DCE parameters showed a significant rise after radiotherapy ($P < 0.0001$).

Correlation of Radiation Dose with Change in DCE Parameters after Treatment

The results showed that there was a significant inverse correlation between percentage change in k_{trans} and radiation dose ($P = 0.0045$), with a higher radiation dose being correlated with a smaller percentage change in k_{trans} (Fig. 2). However, the correlation was insignificant ($P = 0.1695$) when a possible outlier with a greater change in k_{trans} was removed from the analysis. No significant correlation was found between v_e, v_p and radiation dose.

TABLE 1
Summary Statistics

Parameter	Baseline	3 months	*P*
k_{trans}	0.89 ± 0.40	1.52 ± 0.33	<0.0001
v_e	0.42 ± 0.13	0.81 ± 0.13	<0.0001
v_p	0.044 ± 0.018	0.21 ± 0.12	<0.0001

Correlation of Parotid Gland Atrophy with DCE Parameters before and after Treatment

Parotid gland atrophy correlated with baseline v_e and v_p ($P = 0.0008$ and 0.0003, respectively) and change in v_e after treatment ($P = 0.0022$) with atrophy being less in patients with a higher baseline v_e and v_p and a lower percentage increase in v_e after radiotherapy (Figs. 3 and 4). There was no correlation between parotid gland atrophy and k_{trans}.

DISCUSSION

Human and animal studies have shown that parotid gland volume atrophy and reduced salivary production are both common in irradiated parotid glands (*1, 3, 16*), and the radiation dose delivered to the parotid glands correlates with the loss of parotid function (*2*). Other animal studies have shown that this change in salivary function is directly related to histological changes (*3, 4*). Degeneration, necrosis of acinar cells, and inflammation are seen in the early stage of irradiation, while later changes include organ atrophy and an increase in the amount of connective tissue (*3*).

Imaging studies on irradiated parotid glands have been published, with an emphasis on changes in salivary production (*17*) or dosimetric sparing of the organ (*18*). In this study, we used DCE as a tool to investigate the effect of radiation on the parotid glands. Because no data on parotid function were available in this study, we attempted to correlate our DCE results with parameters or attributes that were closely related to parotid function. Radiation dose and volume atrophy have been shown to be related to parotid function. Teshima *et al.* (*19*) showed in radiation-treated head and neck cancer patients that a fractional reduction in parotid gland volume was significantly correlated to reduction in salivary amount. The author concluded that parotid volume reduction may predict irradiated saliva gland function. On the other hand, acinar cells are known to contribute the water and protein content of saliva (*20*), and acinar cell loss was one major cause of volume

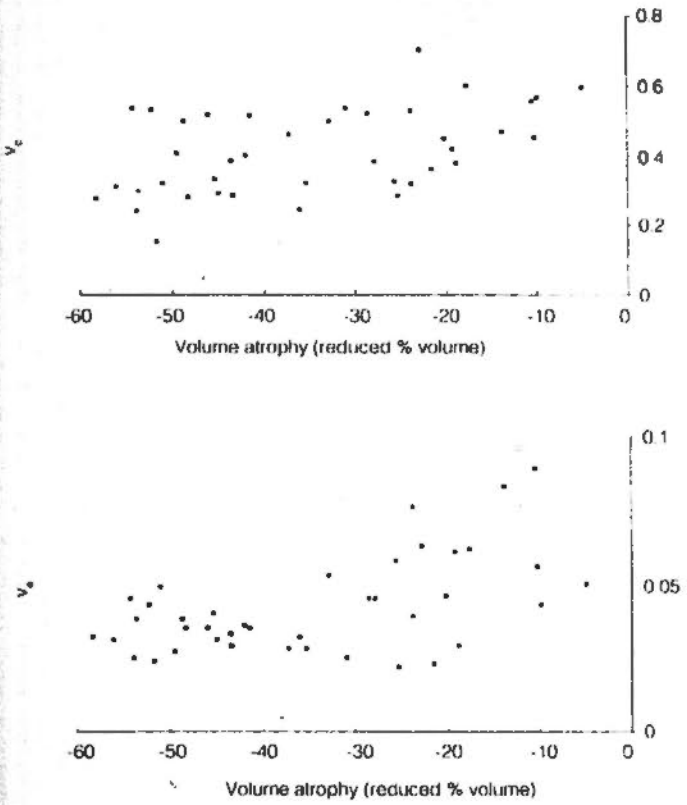

FIG. 4. Baseline v_e and v_p as a function of volume atrophy.

reduction in human parotid glands after irradiation (*20*). Loss of acinar cells thus resulted in a reduction of parotid gland volume and the ability to produce saliva. These studies provided evidence for the close relationship between volume atrophy and loss of function in the parotid gland. Thus, if we could show a relationship between DCE parameters and atrophy, the results would indicate the possibility that DCE parameters may also be correlated with parotid function. This would be useful clinically, although further DCE studies to include functional data are necessary for confirmation.

The first objective was to determine whether radiotherapy would cause a significant change in the DCE parameters and if so whether there was a correlation with radiation dose. The results of this study demonstrated that all three DCE parameters increased significantly 3 months after completion of radiotherapy compared to the baseline values. It is postulated that the increase in k_{trans} may be the result of the early inflammation and disruption of normal endothelium induced by radiation. Such observations have been reported in irradiated tumors during radiation therapy (*8, 21*). It is also known that radiation subsequently damages the vessels and reduces permeability and vascular density, which would be expected to lead to a decrease in the k_{trans}. The fact that a rise and not a fall in k_{trans} was seen in this study suggests that the glands were still going through this earlier phase of damage at 3 months after radiotherapy, with inflammation and endothelium disruption being the predominant features. However, a weak negative correlation was found between the percentage change in k_{trans} and radiation dose; that is, higher radiation doses caused a smaller percentage rise in the k_{trans}. A possible explanation for this unexpected result is that glands that received the higher dose were already starting to enter the later phase of damage so that the effects of inflammation and endothelium disruption were being counteracted by the effects of vessel damage, which cause a decrease in permeability and vascular density and hence a decrease in k_{trans}. However, our observation was limited by the fact that the radiation doses received by the parotid glands in our study were quite large. A better correlation may be demonstrated in future studies of DCE parameters over a wider range of radiation doses.

The v_e and v_p also increased after radiotherapy. In the case of v_e, it is postulated that the rise may have been be related to the increase in extracellular extravascular space (EES) caused by serous acinar cell loss and edema. In the case of v_p, it is postulated that the rise may have been related to inflammation that induces vasodilatation and so could increase blood volume. However, unlike the k_{trans}, neither of these two DCE parameters showed a direct correlation with radiation dose.

The second objective was to correlate parotid gland atrophy with DCE parameters. The study showed that there was a relationship between v_e and v_p but not with the k_{trans}. A higher baseline v_e and v_p was associated with less glandular atrophy. The cause for this association with respect to v_e is unclear, but for v_p it is possible that glands with a higher plasma volume, meaning that the organ is better perfused, would have greater protection from radiation injury. A greater percentage increase in v_e was observed in organs with greater atrophy, which would be expected given that organ atrophy and increased EES are results of increased radiation dose.

A similar study from Juan *et al.* (*22*) using the Brix model showed a correlation between DCE parameters and radiation dose. They found that the peak enhancement and time to peak enhancement were correlated positively while the k_{el} was correlated negatively to dose. They attributed the decrease in k_{el} to increased EES after cell loss, which is in accord to our observation of increased v_e after radiotherapy. The k_{21}, which is the transfer rate constant between plasma and EES, also decreased after radiotherapy. This is in contradiction to our observation of increased k_{trans}. Part of the reason for this discrepancy may be the difference in the timing of image acquisition between the two studies. The cohort of Juan *et al.* included imaging times varying from 2 to 43 months after radiotherapy. Our study imaged patients at baseline and at 3 months after treatment, which is better for describing the early effects of radiotherapy.

The main limitation of this study is that without excision of the parotid gland the cellular cause for the DCE-MRI observations can only be postulated. Animal studies would be needed to confirm the histological basis of the DCE findings. Also, our study examined the effects of radiation at only one time soon after treatment, with no correlation with gland function. To study the correlation between DCE-MRI parameters with late effect of glandular function, a prospective study with serial imaging and salivary flow measurements would be necessary.

In summary, our study increased our knowledge about irradiated parotid glands from the perspective of vascular change by the use of DCE-MRI. Baseline parameters such as v_e and v_p that demonstrated a significant correlation with organ atrophy showed the potential of such parameters in predicting response after radiotherapy. Treatment planning may make use of this information for tailor-made sparing strategies with individual patients.

Conclusions

This study shows the potential of DCE-MRI as a non-invasive tool for examining radiation-induced injury in the parotid glands at the cellular level. A significant increase in k_{trans}, v_e and v_p has been shown in the parotid gland 3 months after irradiation for the treatment of head and neck cancer. The correlation between greater glandular atrophy and a lower baseline v_e and v_p and a higher post-treatment increase in v_e shows the potential for using DCE-MRI for prediction and assessment of radiation damage to the organ.

ACKNOWLEDGMENTS

We would like to express our gratitude to Dr. David Buckley for his advice in the DCE analysis of the data. This study was supported by departmental funding from the Department of Radiology and Organ Imaging, the Chinese University of Hong Kong.

Received: July 16, 2010; accepted: November 8, 2010; published online: January 10, 2011

REFERENCES

1. M. K. Kam, S. F. Leung, B. Zee, R. M. Chau, J. J. Suen, F. Mo, M. Lai, R. Ho, K. Y. Cheung and A. T. Chan, Prospective randomized study of intensity-modulated radiotherapy on salivary gland function in early-stage nasopharyngeal carcinoma patients. *J. Clin. Oncol.* **31**, 4873–4879 (2007).
2. A. Eisbruch, R. K. Ten Haken, H. M. Kim, L. H. Marsh and J. A. Ship, Dose, volume, and function relationships in parotid salivary glands following conformal and intensity-modulated irradiation of head and neck cancer. *Int. J. Radiat. Oncol. Biol. Phys.* **45**, 577–587 (1999).
3. L. C. Stephens, K. K. Ang, T. E. Schultheiss, G. K. King, W. A. Brock and L. J. Peters, Target cell and mode of radiation injury in rhesus salivary glands. *Am. J. Pathol.* **124**, 469–478 (1986).
4. A. W. Konings, H. Faber, F. Cotteleer, A. Vissink and R. P. Coppes, Secondary radiation damage as the main cause for unexpected volume effects: a histopathologic study of the parotid gland. *Int. J. Radiat. Oncol. Biol. Phys.* **64**, 98–105 (2006).
5. P. S. Tofts and A. G. Kermode, Measurement of the blood-brain barrier permeability and leakage space using dynamic MR imaging: Fundamental concepts. *Magn. Reson. Med.* **17**, 357–367 (1991).
6. L. D. Buadu, J. Murakami, S. Murayama, N. Hashiguchi, S. Sakai, K. Masuda, S. Toyoshima, S. Kuroki and S. Ohno, Breast lesions: correlation of contrast medium enhancement patterns on MR images with histopathologic findings and tumor angiogenesis. *Radiology* **200**, 639–649 (1996).
7. C. A. Hulka, W. B. Edmister, B. L. Smith, L. Tan, D. C. Sgroi, T. Campbell, D. B. Kopans and R. M. Weisskoff, Dynamic echo-planar imaging of the breast: experience in diagnosing breast carcinoma and correlation with tumor angiogenesis. *Radiology* **205**, 837–842 (1997).
8. M. A. Zahra, K. G. Hollingsworth, E. Sala, D. J. Lomas and L. T. Tan, Dynamic contrast-enhanced MRI as a predictor of tumour response to radiotherapy. *Lancet Oncol.* **8**, 63–74 (2007).
9. D. L. Buckeley, C. Roberst, G. J. M. Parker, J. P. Logue and C. E. Hutchinson, Prostate cancer: Evaluation of vascular characteristics with dynamic contrast enhanced T1-weighted MR imaging – initial experience. *Radiology* **233**, 709–715 (2004).
10. H. Konouchi, J. Asaumi, Y. Yanagi, H. Shigehara, M. Hisatomi, H. Matsuzaki and K. Kishi, Evaluation of tumor proliferation using dynamic contrast enhanced-MRI of oral cavity and oropharyngeal squamous cell carcinoma. *Oral Oncol.* **39**, 290–295 (2003).
11. S. Kim, H. Quon, L. A. Loevner, M. A. Rosen, L. Dougherty, A. M. Kilger, J. D. Glickson and H. Poptani, Transcytolemmal water exchange in pharmacokinetic analysis of dynamic contrast-enhanced MRI data in squamous cell carcinoma of the head and neck. *J. Magn. Reson. Imaging* **26**, 1607–1617 (2007).
12. P. J. Hoskin, M. I. Saunders, K. Goodchild, M. E. Powell, N. J. Taylor and H. Baddeley, Dynamic contrast enhanced magnetic resonance scanning as a predictor of response to accelerated radiotherapy for advanced head and neck cancer. *Br. J. Radiol.* **72**, 1093–1098 (1999).
13. X. P. Zhu, K. L. Li, I. D. Kamaly-Asl, D. R. Checkley, J. J. Tessier, J. C. Waterton and A. Jackson, Quantification of endothelial permeability, leakage space, and blood volume in brain tumors using combined T1 and T2* contrast enhanced dynamic MR imaging. *J. Magn. Reson. Imaging* **11**, 575–585 (2000).
14. M. Rijpkema, J. H. Kaanders, F. B. Joosten, A. J. van der Kogel and A. Heerschap, Method for quantitative mapping of dynamic MRI contrast agent uptake in human tumors. *J. Magn. Reson. Imaging* **14**, 457–463 (2001).
15. T. S. Ahearn, R. T. Staff, T. W. Redpath and S. I. Semple, The use of the Levenberg-Marquardt curve-fitting algorithm in pharmacokinetic modeling of DCE-MRI data. *Phys. Med. Biol.* **50**, N85–N92 (2005).
16. B. Bussels, A. Maes, P. Flamen, P. Lambin, K. Erven, R. Hermans, S. Nuyts, C. Weltens, S. Cecere and W. Van den Bogaert, Dose response relationships with the parotid gland after radiotherapy for head and neck cancer. *Radiother. Oncol.* **73**, 297–306 (2004).
17. A. I. Blanco, K. S. Chao, I. El Naqa, G. E. Franklin, K. Zakarian, M. Vicic and J. O. Deasy, Dose-volume modeling of salivary function in patients with head-and-neck cancer receiving radiotherapy. *Int. J. Radiat. Oncol. Biol. Phys.* **62**, 1055–1069 (2005).
18. A. Wada, N. Uchida, M. Yokokawa, T. Yoshizako and H. Kitagaki, Radiation-induced xerostomia: objective evaluation of salivary gland injury using MR sialography. *Am. J. Neuroradiol.* **30**, 53–58 (2009).
19. K. Teshima, R. Murakami, E. Tomitaka, T. Nomura, R. Toya, A. Hiraki, H. Nakayama, T. Hirai, M. Shinohara and Y. Yamashita, Radiation-induced parotid gland changes in oral cancer patients: correlation between parotid volume and saliva production. *Jpn. J. Clin. Oncol.* **40**, 42–46 (2010).

20. I. M. A. Lombaert, J. F. Brunsting, P. K. Wierenga, H. Faber, M. A. Stokman, T. Kok, W. H. Visser, H. H. Kampinga, G. de Haan and R. P. Coppes, Rescue of salivary gland function after stem cell transplantation in irradiated glands. *PLoS ONE* **4**, e2063 (2008).

21. Q. S. Ng, V. Goh, J. Milner, A. R. Padhani, M. I. Saunders and P. J. Hoskin, Acute tumor vascular effects following fractionated radiotherapy in human lung cancer: in vivo whole tumor assessment using volumetric perfusion computed tomography. *Int. J. Radiat. Oncol. Biol. Phys.* **67**, 417–424 (2007).

22. C. J. Juan, C. Y. Chen, Y. M. Jen, H. S. Liu, Y. J. Liu, C. J. Hsueh, C. Y. Wang, Y. C. Chou, Y. T. Chai and H. W. Chung, Perfusion characteristics of late radiation injury of parotid glands: quantitative evaluation with dynamic contrast-enhanced MRI. *Eur. Radiol.* **19**, 94–102 (2009).

G Model
EURR-5253; No. of Pages 5

European Journal of Radiology xxx (2011) xxx–xxx

Contents lists available at ScienceDirect

European Journal of Radiology

journal homepage: www.elsevier.com/locate/ejrad

Dynamic contrast enhancement magnetic resonance imaging (DCE-MRI) for differential diagnosis in head and neck cancers

Francis Kar-ho Lee[a,*], Ann Dorothy King[a], Brigitte Buig-Yue Ma[b,c], David Ka-wai Yeung[a]

[a] Department of Imaging and Interventional Radiology, Prince of Wales Hospital, the Chinese University of Hong Kong, Hong Kong SAR
[b] Department of Clinical Oncology, Prince of Wales Hospital, Shatin, New Territories, Hong Kong
[c] State Key Laboratory in Oncology in South China, Sir Y.K. Pao Centre for Cancer, Hong Kong Institute, Department of Clinical Oncology, Prince of Wales Hospital, the Chinese University of Hong Kong, Hong Kong

ARTICLE INFO

Article history:
Received 19 July 2010
Accepted 20 January 2011

Keywords:
Dynamic contrast enhancement magnetic resonance imaging (DCE-MRI)
Squamous cell carcinoma
Undifferentiated carcinoma and lymphoma
Diagnosis

ABSTRACT

Purpose: To examine the potential of dynamic contrast enhanced magnetic resonance imaging (DCE-MRI) for differential diagnosis of head and neck cancer.
Methods and materials: DCE-MRI was performed in 26 patients with untreated squamous cell carcinoma (SCC), 28 undifferentiated carcinoma (UD) and 8 lymphoma. DCE-MRI was analyzed with the pharmacokinetic model proposed by Tofts and Kermode to produce the three DCE parameters: k_{trans}, v_e and v_p. Areas under the curve (AUC) at the initial 60 and 90 s (AUC60 and AUC90) were also recorded. Histogram analysis was conducted to obtain the mean, 25%, 50%, 75% and 95% percentile values and the Kruskal–Wallis test was used to compare the DCE parameters between the three groups of cancer.
Results: k_{trans}, AUC60 and AUC90 showed significant differences ($p < 0.01$) between UD/SCC and UD/lymphoma, but not between SCC/lymphoma. The mean AUC90 demonstrated the highest accuracy of 78% (sensitivity of 68% and specificity of 88%) for distinguishing UD and SCC, and the 75% percentile AUC90 provided the highest accuracy of 97% (sensitivity of 100% and specificity of 88.5%) for distinguishing UD and lymphoma.
Conclusions: There are significant differences in the DCE parameters which show the potential for distinguishing UD from SCC or lymphoma.

1. Introduction

Dynamic contrast enhanced magnetic resonance imaging (DCE-MRI) is a non-invasive technique which provides information on the micro-vascular environment of cancers by means of analysis of contrast agent kinetics. It is under active research as a potential investigative tool for cancer, including characterization of cancers, guidance for treatment planning, early prediction of treatment responses and evaluation of treatment outcome. In this study we evaluated the ability of DCE-MRI to distinguish between three cancers which are found along the aerodigestive tract in the head and neck region; squamous cell carcinoma (SCC), undifferentiated carcinoma (UD) and lymphoma. According to statistics from the National Cancer Institute in 2007, cancers in the head and neck region account for about 6% of the adult cancers in the United States, and in our population this proportion is twice as high [1]. In regard to lesions in the head and neck there have been a number of published reports using the shape of the dynamic contrast enhancement curve for qualitative DCE analysis [2–6], while other reports analyzing the enhancement curve, such as the use of enhancement ratio and slope [7–18] have characterized tumors in a more quantitative manner. In general, tumors that demonstrated high enhancement ratio and slope corresponded to vascular and active tumor and these tumors responded better to treatment because of better perfusion and less hypoxic and necrotic regions. In comparison, pharmacokinetic modeling of the tracer kinetics, which generates DCE parameters with a more well defined physiological meaning have not been reported as extensively in the head and neck [19–22,43] and has not been reported in relationship to the characterization of different tumors.

This study investigated the use of DCE in head and neck cancers for differential diagnosis of three types of head and neck cancers using DCE parameters generated from a pharmacokinetic model

* Corresponding author. Tel.: +852 29585427; fax: +852 29586654.
E-mail addresses: leekarhof@hotmail.com (F.K.-h. Lee), kmg2015@cuhk.edu.hk (A.D. King), Brigette@clo.cuhk.edu.hk (B.B.-Y. Ma), dkyeung@cuhk.edu.hk (D.K.-w. Yeung).

0720-048X/$ – see front matter © 2011 Elsevier Ireland Ltd. All rights reserved.
doi:10.1016/j.ejrad.2011.01.089

Table 1
DCE-MRI scan protocol.

Scan	Sequences	TR/TE/α (ms/°)	Pixel matrix
FFE2	3D T1W-FE	2.7/0.9/2	128 × 128 × 25
FFE10	3D T1W-FE	2.7/0.9/10	128 × 128 × 25
FFE20	3D T1W-FE	2.7/0.9/20	128 × 128 × 25
FFE30	3D T1W-FE	2.7/0.9/30	128 × 128 × 25
T1 dyn	3D T1W-FE	2.7/0.9/20	128 × 128 × 25 × 106 phases

proposed by Tofts and Kermode [23] as well as using the area under curve (AUC) of contrast concentration.

2. Materials and methods

2.1. Patients

63 patients with histological proven malignant head and neck lesions, with 26 undifferentiated carcinomas (all nasopharyngeal region), 28 squamous cell carcinomas (10 hypopharynx, 10 tonsil, 2 retromolar trigone, 2 oesophageal, 1 supraglottic, 1 larynx, 1 nasal cavity, 1 maxillary sinus) and 8 lymphomas (1 parotid, 1 maxilla, 2 tonsil, 1 tongue base, 2 nasopharyngeal, 1 oral cavity; 6 low grade and 2 high grade) underwent dynamic contrast enhanced (DCE) MRI scanning at the time of their staging MRI examination. The local research ethics committee approved the study, and patients were entered in the study after informed consent.

2.2. Image acquisition

Patients were scanned in a 1.5 T MR scanner (Philips Medical System, Best, the Netherlands) with the head and neck SENSE coil according to the protocol shown in Table 1. The four 3D T1-weighted gradient echo images with different flip angles were used to generate the T1 map. Dynamic gradient echo images were acquired at a time resolution of 3.5 s for 106 time points. Contrast agent (Dotarem, Guerbet, France) at a dose of 0.2 ml/kg was intravenously injected with a power injector at a rate of 3 ml/s. Injection began at 20 s after the start of the dynamic sequence. Immediately after the injection, the same amount of saline was flushed into the syringe at the same injection rate.

2.3. Data processing and image analysis

Images were exported from the scanner console to an off-line computer for processing. An experienced radiologist contoured the whole tumor on the post contrast T1-weighted image. The T1 map was calculated by the use of the gradient echo images, as determined by the Ernst formula and the contrast concentration was derived from the dynamic intensity curve (refer to reference 11 for details of the algorithm). The resultant contrast concentration dynamic curve for each pixel was used as input for the DCE modeling, with pharmacokinetic models from Tofts and Kermode [23]. The arterial input function (AIF) was obtained from the common or external carotid artery. The k_{trans}, v_e and v_p (Table 2) were estimated for every pixel using multiple starting point Marquardt–Levendag curve fitting [24]. In addition, the area under the contrast concentration curve for the initial 60 s (AUC60), and the initial 90 s (AUC90) were measured and normalized by the AUC60 of the external carotid artery, to adjust for differences in arterial input of individual patients and scans.

Table 2
Physiological meaning of the DCE parameters.

Parameter	Physiological meaning
k_{trans}	Blood plasma flow per unit volume of tissue. In situation of high blood flow, k_{trans} is the permeability surface area product per unit volume of tissue.
v_e	EES volume per unit volume of tissue
v_p	Blood plasma volume per unit volume of tissue

Table 3
Mean and standard deviation of the DCE parameters for UD, SCC and lymphoma.

	UD	SCC	Lymphoma
Tofts			
k_{trans} (1/min)	1.26 ± 0.61	0.78 ± 0.47	0.59 ± 0.18
v_e	0.65 ± 0.16	0.64 ± 0.13	0.54 ± 0.17
v_p	0.11 ± 0.12	0.08 ± 0.06	0.07 ± 0.03
Semi-quantitative			
AUC60 (norm. unit)	0.31 ± 0.11	0.23 ± 0.10	0.21 ± 0.05
AUC90 (norm. unit)	0.74 ± 0.28	0.54 ± 0.21	0.50 ± 0.09

Histogram analysis was performed on the data generated from the whole lesion and mean value for each parameter was obtained. In order to take account of tumor heterogeneity, the values were also calculated for the 25%, 50%, 75% and 95% percentile value for each primary tumor.

Table 2 tabulates the 3 parameters derived from the model curve fitting and the physiological meaning of the parameters.

2.4. Statistical analysis

Kruskal–Wallis test was performed to determine the parameters with significant differences ($p < 0.01$) between the three groups of cancer. DCE parameters that showed significant differences underwent further Receiver Operator Characteristic (ROC) analysis to determine the sensitivities and specificities with the highest degree of accuracy. Also, a cutoff value was chosen that maximized specificity while optimizing the sensitivity.

3. Results

The mean and the values at the 25%, 50%, 75% and 95% percentile for the DCE parameters are shown in Fig. 1. Table 3 gives the mean and standard deviation for the parameters in the three types of tumors.

There were significant differences ($p < 0.01$) in the k_{trans}, AUC60 and AUC90 between UD and SCC and between UD and lymphoma, but no parameters showed a significant difference between SCC and lymphoma. ROC analysis was performed and results of the parameters that demonstrated the greatest accuracy and sensitivity for differentiation of the tumors are shown in Tables 4 and 5. Fig. 2 shows the average histogram for the k_{trans}, AUC60 and AUC90 of UD, SCC and lymphoma.

4. Discussion

Relatively few research studies have reported results using DCE-MRI parameters from head and neck cancers generated using pharmacokinetic models and quantitative analysis [19–22] and none have used the tool to distinguish between UD, SCC and lymphoma. In this study, k_{trans}, AUC60 and AUC90 showed significant differences between UD/SCC and UD/lymphoma but none of the parameters showed a significant difference between SCC/lymphoma. The parameter that showed the highest accuracy was the AUC90, yielding 78% and 97% respectively for differentiation between UD/SCC and UD/lymphoma. When measuring functional parameters, tumor heterogeneity can influence the results and so methods which take into account heterogeneity in tumor vascularity, such as histogram analysis [25–27], are becoming a recognized method to assess cancers. Our results from histogram analysis concur with this view, whereby using AUC90

Please cite this article in press as: Lee FK-h, et al. Dynamic contrast enhancement magnetic resonance imaging (DCE-MRI) for differential diagnosis in head and neck cancers. Eur J Radiol (2011), doi:10.1016/j.ejrad.2011.01.089

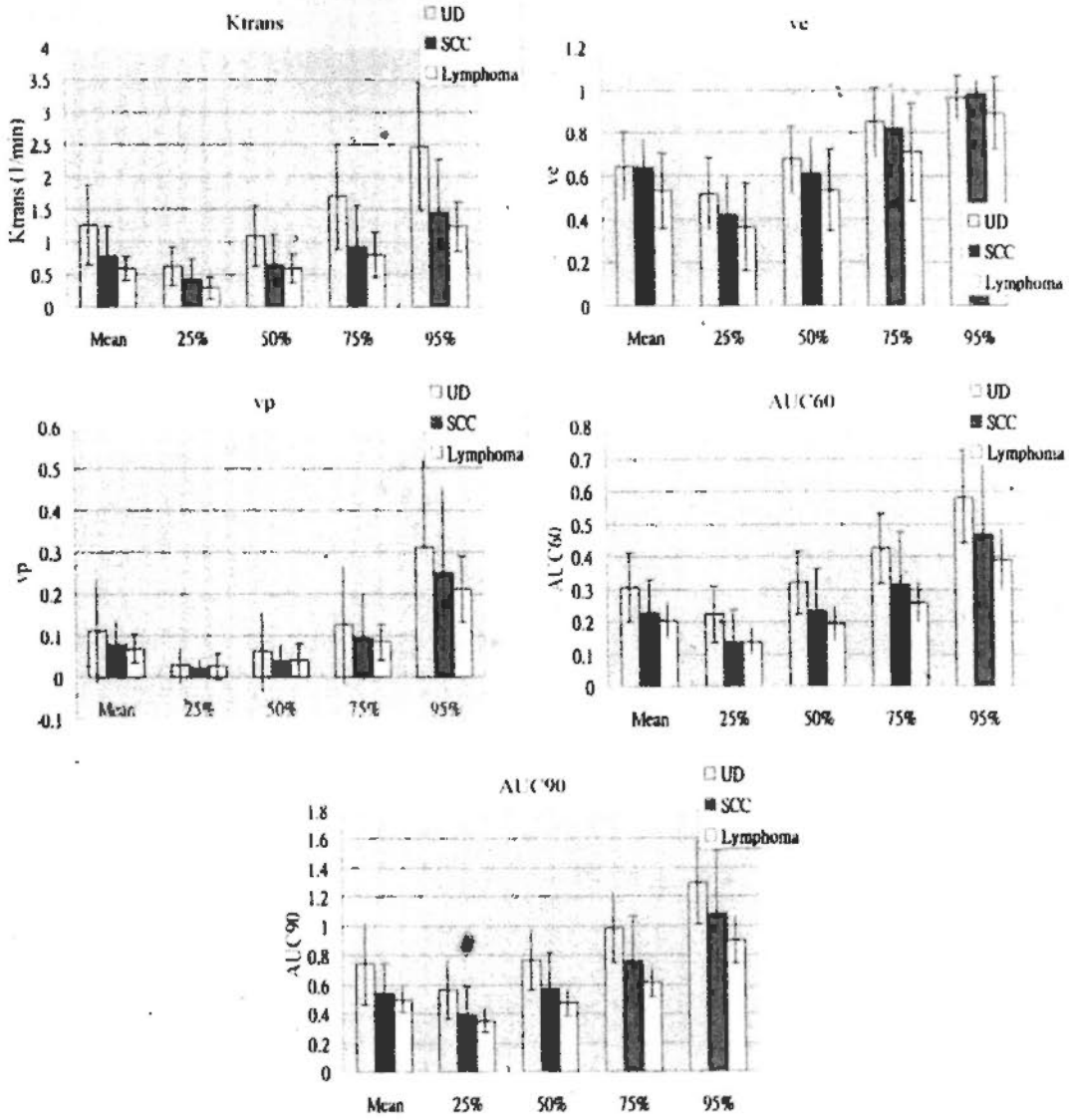

Fig. 1. Bar charts of the DCE parameters for UD, SCC and lymphoma.

Table 4
Parameters with the maximum accuracy for differentiation of tumors.

	Parameter	Accuracy	Sensitivity %	Specificity %	Cutoff value
UD/SCC	Mean–AUC90	0.784	68%	88%	0.616
UD/lymphoma	75%–AUC90	0.973	100%	88.5%	0.754

values obtained from 75% and 25% percentile obtained results with the maximum accuracy and sensitivity.

The k_{trans} value in our study for UD was significantly higher than the other two types of tumors. Since k_{trans} is in part related to vascular permeability, this may infer that vessels in UD have a higher permeability than the other two types of tumors. Another biomarker which is related to vascular permeability [28], is vascular endothelial growth factor (VEGF). Interestingly the rate of positive/high expression in VEGF for UD has been reported to range from 45.7 to 80% [29–31] and the upper limit of this range for UD is greater than that of SCC [32–35] (24.1–50%) or lymphoma [36–39] (0–60%). Our k_{trans} results therefore appear to correlate with the VEGF data.

In addition to k_{trans}, AUCs in our study were significantly higher in UD than in SCC and lymphoma and both of these parameters have been suggested as primary end points for DCE studies on anti-vascular therapies [40]. Compared to k_{trans}, AUC has no biological specificity but is rather a measure of amount of contrast delivered to

Table 5
Parameters with maximum sensitivity at 100% specificity.

	Parameter	Accuracy	Sensitivity %	Specificity %	Cutoff value
UD/SCC	25%–AUC60	0.695	36.7%	100%	0.071
Lymphoma/UD	75%–AUC90	0.973	88.5%	100%	0.754

Please cite this article in press as: Lee FK-h, et al. Dynamic contrast enhancement magnetic resonance imaging (DCE-MRI) for differential diagnosis in head and neck cancers. Eur J Radiol (2011), doi:10.1016/j.ejrad.2011.01.089

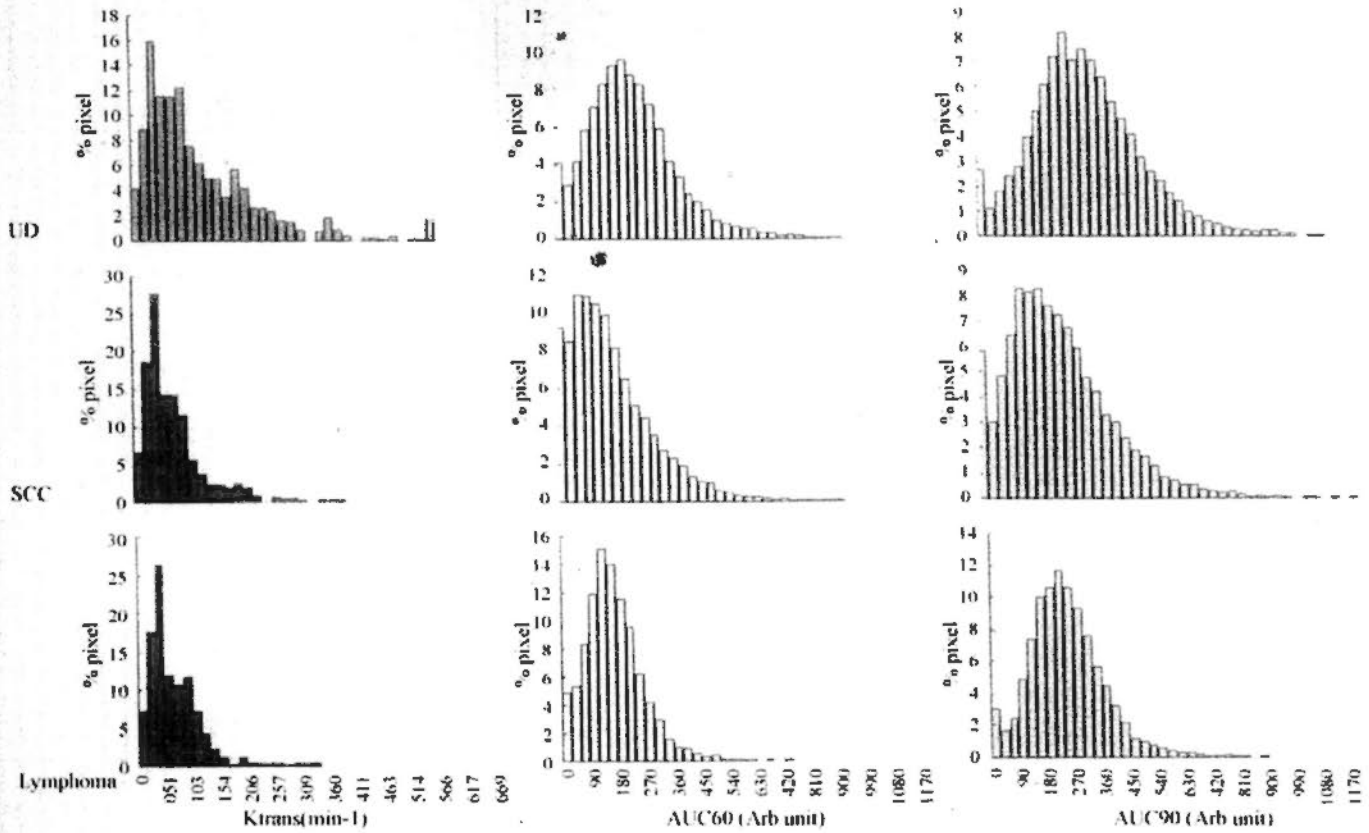

Fig. 2. Histogram analysis of k_{trans}, AUC60 and AUC90 for UD (top row), SCC (middle row) and lymphoma (bottom row).

and retained by tumor in a given time period [44]. Our ROC analysis reveals that AUC90 yields better accuracy and sensitivity than k_{trans} in the differentiation of tumors. This may be due to the fact that AUC is more robust because of its relative simplicity in the process of parameter extraction. This is supported in a study by Galbraith et al. [41], which showed that AUC has a better reproducibility than k_{trans}.

Limited number of cases in the lymphoma group is the major limitation of our study. Difficulty in recruitment is the reason for such limitation. Despite the weakness, we do not expect a major difference in study outcome if more cases are recruited. There was a relatively narrow range of DCE values for lymphoma as compared to SCC in the present series, this data is likely to be reproducible with a larger sample size.

Another functional MRI technique, diffusion weighted imaging (DWI), has shown significant differences amongst all three of these cancers. Using the apparent diffusion coefficient (ADC) as the DWI biomarker [42], it was found that the ADC value of UD was in between that of lymphoma (lower ADC) and SCC (higher ADC), which is a different trend to that seen with DCE where it is SCC which has parameters that are in between UD (higher k_{trans} and AUC) and lymphoma (lower k_{trans} and AUC). For identification of cancer groups it is clinically useful to set the specificity to 100% while trying to maintain a high sensitivity and by doing so it appears that DCE and DWI produce complementary information with DCE of value in distinguishing lymphoma from UD and DWI for distinguishing lymphoma from SCC.

5. Conclusions

In this study, we analyzed the DCE data of undifferentiated carcinoma (UD), squamous cell carcinoma (SCC) and lymphoma with the use of quantitative analysis and pharmacokinetic modeling. Results identified several parameters that showed significant difference between UD/SCC and UD/lymphoma, namely k_{trans}, AUC60 and AUC90. However, no parameters showed a difference between SCC and lymphoma. The highest accuracy for DCE was obtained by taking into account tumor heterogeneity to analyze different percentile values obtained from a histogram. DCE parameters identified in this study may prove its clinical utility to assist differentiation of different types of head and neck tumors. Of all DCE parameters the AUC90 was shown to produce the highest accuracy, which would be an advantage in routine clinical practice because of its relative simplicity in the process of parameter extraction compared to the model based parameters such as k_{trans}.

Acknowledgement

We would like to express our gratitude to Dr. David Buckley for his advice on DCE technique and modeling.

References

[1] Hospital Authority: Hong Kong cancer registry 2007.
[2] Escott EJ, Rao VM, Ko WD, et al. Comparison of dynamic contrast-enhanced gradient-echo and spin-echo sequences in MR of head and neck neoplasms. AJNR Am J Neuroradiol 1997;(18):1411–9.
[3] Tezelman S, Giles Y, Tunca F, et al. Diagnostic value of dynamic contrast medium enhanced magnetic resonance imaging in preoperative detection of thyroid carcinoma. Arch Surg 2007;142:1036–41.
[4] Alibek S, Zenk J, Bozzato A, et al. The value of dynamic MRI studies in parotid tumors. Acad Radiol 2007;14:701–10.
[5] Baba Y, Furusawa M, Murakami R, et al. Role of dynamic MRI in the evaluation of head and neck cancers treated with radiation therapy. Int J Radiat Oncol Biol Phys 1997;37:783–7.
[6] Hisatomi M, Asaumi J, Konouchi H, et al. Assessment of dynamic MRI of Warthin's tumors arising as multiple lesions in the parotid glands. Oral Oncol 2002;38:369–72.

Please cite this article in press as: Lee FK-h, et al. Dynamic contrast enhancement magnetic resonance imaging (DCE-MRI) for differential diagnosis in head and neck cancers. Eur J Radiol (2011), doi:10.1016/j.ejrad.2011.01.089

[7] Asaumi J, Yanagi Y, Konouchi H, et al. Application of dynamic contrast-enhanced MRI to differentiate malignant lymphoma from squamous cell carcinoma in the head and neck. Oral Oncol 2004;40:579–84.
[8] Hoskin PJ, Saunders MI, Goodchild K, et al. Dynamic contrast enhanced magnetic resonance scanning as a predictor of response to accelerated radiotherapy for advanced head and neck cancer. Br J Radiol 1999;72:1093–8.
[9] Asaumi J, Yanagi Y, Hisatomi M, et al. The value of dynamic contrast-enhanced MRI in diagnosis of malignant lymphoma of the head and neck. Eur J Radiol 2003;48:183–7.
[10] Semiz Oysu A, Ayanoglu E, Kodalli N, et al. Dynamic contrast-enhanced MRI in the differentiation of posttreatment fibrosis from recurrent carcinoma of the head and neck. Clin Imaging 2005;29:307–12.
[11] Tomura N, Omachi K, Sakuma I, et al. Dynamic contrast-enhanced magnetic resonance imaging in radiotherapeutic efficacy in the head and neck tumors. Am J Otolaryngol 2005;26:163–7.
[12] Fischbein NJ, Noworolski SM, Henry RG, et al. Assessment of metastatic cervical adenopathy using dynamic contrast-enhanced MR imaging. AJNR Am J Neuroradiol 2003;24:301–11.
[13] Göckel C, Schnabel K, Deimling M, et al. Dynamic snapshot gradient-echo imaging of head and neck malignancies: time dependency and quality of contrast-to-noise ratio. MAGMA 1996;4:61–9.
[14] Baba Y, Yamashita Y, Onomichi M, et al. Dynamic magnetic resonance imaging of head and neck lesions. Top Magn Reson Imaging 1999;10:125–9.
[15] Konouchi H, Asaumi J, Yanagi Y, et al. Evaluation of tumor proliferation using dynamic contrast enhanced-MRI of oral cavity and oropharyngeal squamous cell carcinoma. Oral Oncol 2003;39:290–5.
[16] Noworolski SM, Fischbein NJ, Kaplan MJ, et al. Challenges in dynamic contrast-enhanced MRI imaging of cervical lymph nodes to detect metastatic disease. J Magn Reson Imaging 2003;17:455–62.
[17] Ariyoshi Y, Shimahara M. Relationships between dynamic contrast-enhanced MRI findings and pattern of invasion for tongue carcinoma. Oncol Rep 2006;15:1339–43.
[18] Hisatomi M, Asaumi J, Yanagi Y, et al. Diagnostic value of dynamic contrast-enhanced MRI in the salivary gland tumors. Oral Oncol 2007;43:940–7.
[19] Kim S, Quon H, Loevner LA, et al. Transcytolemmal water exchange in pharmacokinetic analysis of dynamic contrast-enhanced MRI data in squamous cell carcinoma of the head and neck. J Magn Reson Imaging 2007;26:1607–17.
[20] Machiels JP, Henry S, Zanetta S, et al. Phase II study of sunitinib in recurrent or metastatic squamous cell carcinoma of the head and neck: GORTEC 2006-01. J Clin Oncol 2010;28:21–8.
[21] Jansen JF, Schöder H, Lee NY, et al. Noninvasive assessment of tumor microenvironment using dynamic contrast-enhanced magnetic resonance imaging and (18)F-fluoromisonidazole positron emission tomography imaging in neck nodal metastases. Int J Radiat Oncol Biol Phys 2009.
[22] Shukla-Dave A, Lee N, Stambuk H. Average arterial input function for quantitative dynamic contrast enhanced magnetic resonance imaging of neck nodal metastases. BMC Med Phys 2009;7:4.
[23] Tofts PS, Kermode AG. Measurement of the blood–brain barrier permeability and leakage space using dynamic MR imaging: fundamental concepts. Magn Reson Med 1991;17:357–67.
[24] Ahearn TS, Staff RT, Redpath TW, et al. The use of the Levenberg–Marquardt curve-fitting algorithm in pharmacokinetic modeling of DCE-MRI data. Phys Med Biol 2005;50:N85–92.
[25] Yuh WT, Mayr NA, Jarjoura D, et al. Predicting control of primary tumor and survival by DCE MRI during early therapy in cervical cancer. Invest Radiol 2009;44:343–50.
[26] Hayes C, Padhani AR, Leach MO. Assessing changes in tumour vascular function using dynamic contrast-enhanced magnetic resonance imaging. NMR Biomed 2002;15:154–63.
[27] Jackson A, O'Connor JPB, Parker GJM, et al. Imaging tumor vascular heterogeneity and angiogenesis using dynamic contrast-enhanced magnetic resonance imaging. Clin Cancer Res 2007;13:3449–59.
[28] Senger DR, Water LVD, Brown LE, et al. Vascular permeability factor (VPF VEGF) in tumor biology. Cancer Metast Rev 1993;12:303–24.
[29] Guang-Wu H, Sunagawa M, Li JE, et al. The relationship between microvessel density, the expression of vascular endothelial growth factor (VEGF), and the extension of nasopharyngeal carcinoma. Laryngoscope 2000;110:2066–9.
[30] Pan J, Kong L, Lin S, et al. The clinical significance of coexpression of cyclooxygenases-2, vascular endothelial growth factors, and epidermal growth factor receptor in nasopharyngeal carcinoma. Laryngoscope 2008;118:1970–5.
[31] Li Y-H, Hu C-F, Qiong Q, et al. Elevated expressions of survivin and VEGF protein are strong independent predictors of survival in advanced nasopharyngeal carcinoma. J Transl Med 2008;6:1.
[32] Mineta H, Miura K, Ogino T, et al. Prognostic value of vascular endothelial growth factor (VEGF) in head and neck squamous cell carcinomas. Br J Cancer 2000;83:775–81.
[33] Vipa B, Boonchu K, Juvady L, et al. Vascular endothelial growth factor A and proliferation marker in prediction of lymph node metastasis in oral and pharyngeal squamous cell carcinoma. Arch Otolaryngol Head Neck Surg 2008;134:1305–11.
[34] Bandoh N, Hayashi T, Takahara M, et al. VEGF and bFGF expression and microvessel density of maxillary sinus squamous cell carcinoma in relation to p53 status, spontaneous apoptosis and prognosis. Cancer Lett 2004;208:215–25.
[35] Sawatsubashi M, Yamada T, Fukushima N, et al. Association of vascular endothelial growth factor and mast cells with angiogenesis in laryngeal squamous cell carcinoma. Virchows Arch 2000;436:243–8.
[36] Gratzinger D, Zhao S, Marinelli RJ, et al. Microvessel density and expression of vascular endothelial growth factor and its receptors in diffuse large B-cell lymphoma subtypes. Am J Pathol 2007;170:1362–9.
[37] Hazar B, Paydas S, Zorludemir S, et al. Prognostic significance of microvessel density and vascular endothelial growth factor (VEGF) expression in non-Hodgkin's lymphoma. Leukemia Lymphoma 2003;44:2089–93.
[38] Mainou-Fowler T, Angus B, Miller S, et al. Micro-vessel density and the expression of vascular endothelial growth factor (VEGF) and platelet-derived endothelial cell growth factor (PdEGF) in classical Hodgkin lymphoma (HL). Leukemia Lymphoma 2006;47:223–30.
[39] Gratzinger D, Advani R, Zhao S, et al. Lymphoma cell VEGFR2 expression detected by immunohistochemistry predicts poor overall survival in diffuse large B cell lymphoma treated with immunochemotherapy (R-CHOP). Br J Haematol 2010;148:235–44.
[40] Leach MO, Brindle KM, Evelhoch JL, et al. The assessment of antiangiogenic and antivascular therapies in early-stage clinical trials using magnetic resonance imaging: issues and recommendations. Br J Cancer 2005;92:1599–610.
[41] Galbraith SM, Lodge MA, Taylor NJ, et al. Reproducibility of dynamic contrast enhanced MRI in human muscle and tumors: comparison of quantitative and semi-quantitative analysis. NMR Biomed 2002;15:132–42.
[42] Fong D, Bhatia KSS, Yeung D, King AD. Diagnostic accuracy of diffusion-weighted MR imaging for nasopharyngeal carcinoma, head and neck lymphoma and squamous cell carcinoma at the primary site. Oral Oncol 2010;46(8):603–6.
[43] Kim S, Loevner LA, Quon H, et al. Prediction of response to chemoradiation therapy in squamous cell carcinomas of the head and neck using dynamic contrast-enhanced MR imaging. Am J Neuroradiol 2010;31:262–8.
[44] Walker-Samuel S, Leach MO, Collins DJ. Evaluation of response to treatment using DCE-MRI: the relationship between initial area under the gadolinium curve (IAUGC) and quantitative pharmacokinetic analysis. Phys Med Biol 2006;51:3593–602.

Please cite this article in press as: Lee FK-h, et al. Dynamic contrast enhancement magnetic resonance imaging (DCE-MRI) for differential diagnosis in head and neck cancers. Eur J Radiol (2011), doi:10.1016/j.ejrad.2011.01.089

RADIATION RESEARCH 175, 291–296 (2011)
0033-7587/11 $15.00

DOI: 10.1667/RR2370.1

Radiation Injury of the Parotid Glands During Treatment for Head and Neck Cancer: Assessment Using Dynamic Contrast-Enhanced MR Imaging

Francis Kar-ho Lee,[a,1] Ann Dorothy King,[a] Michael Koon-ming Kam,[b] Brigette Buig-yue Ma[b] and David Ka-wai Yeung[a]

[a] *Department of Diagnostic Radiology and Organ Imaging, Prince of Wales Hospital, the Chinese University of Hong Kong, Hong Kong SAR; and* [b] *Department of Clinical Oncology, Prince of Wales Hospital, the Chinese University of Hong Kong, Hong Kong SAR*

Lee, F. K., King, A. D., Kam, M. K., Ma, B. B. and Yeung, D. K. Radiation Injury of the Parotid Glands During Treatment for Head and Neck Cancer: Assessment Using Dynamic Contrast-Enhanced MR Imaging. *Radiat. Res.* 175, 291–296 (2011).

The parotid gland is an important organ at risk of complications of radiotherapy for head and neck cancer. In this study, we examined the potential of dynamic contrast-enhanced magnetic resonance imaging (DCE-MRI) for assessment of radiation injury to the parotid glands. DCE-MRI was performed before and 3 months after radiotherapy in patients treated for head and neck cancer. DCE-MRI was analyzed using the pharmacokinetic model proposed by Tofts and Kermode to produce three DCE parameters: k_{trans}, v_e and v_p. These parameters were correlated with the dose of radiation delivered to the parotid glands and the degree of radiation-induced parotid atrophy. The mean radiation dose received by the parotid glands was 47.1 ± 6.6 Gy. All patients received concurrent chemotherapy. There was a significant rise in all three parameters after therapy ($P < 0.0001$). Baseline v_e and v_p and the post-treatment rise in v_e correlated with parotid gland atrophy ($P = 0.0008$, 0.0003 and 0.0022, respectively). DCE-MRI has the potential to be used as a non-invasive technique for predicting and assessing radiation injury in the parotid glands. © 2011 by Radiation Research Society

INTRODUCTION

The parotid glands lie within or close to the radiation field of many head and neck cancers, and hence these glands are often unavoidably irradiated during radiation treatment. Radiation injury to the parotid glands induces xerostomia, which has a significant impact on the patient's quality of life. New developments in radiotherapy have focused on using techniques such as conformal radiotherapy and intensity-modulated radiotherapy (IMRT) to reduce the radiation dose to the parotid glands while at the same time delivering sufficient dose to the cancer targets (*1, 2*).

However, even with these newer techniques, it is not always possible to prevent the glands from receiving a significant radiation dose. There is therefore interest in finding other strategies for better protection of the organ. These require an understanding of radiation-induced damage on a cellular level. Histological studies have been conducted in rats and rhesus monkeys that showed inflammation, edema, acinar cell degeneration and necrosis, vessel damage and organ atrophy after irradiation (*3, 4*). Similar studies are more difficult to perform on human subjects due to the invasive nature of obtaining parotid tissue samples and inability to examine the whole gland. Therefore, an *in vivo* tool to monitor radiation damage in the parotid gland on the cellular and vascular level would be valuable.

Dynamic contrast-enhanced magnetic resonance imaging (DCE-MRI) is a functional imaging technique that provides information on tissue perfusion through dynamic contrast analysis by compartment modeling or curve fitting. DCE parameters obtained using pharmacokinetic models such as those proposed by Tofts and Kermode (*5*) provide data that can reflect physiological processes such as vascularity, vessel permeability and cellularity of the examined tissue. This technique has been applied to the diagnosis, prognosis and evaluation of treatment response in cancers of the breast (*6, 7*) and prostate (*8, 9*), and efforts have been made to extend its application to head and neck malignancies (*10–12*). DCE-MRI also has the potential to yield valuable *in vivo* information on the damage that occurs in organs that are irradiated and to provide a non-invasive method for studying the irradiated parotid glands. The focus of this study was to use DCE-MRI to determine whether radiation exposure leads to any changes in the DCE parameters and if so to determine whether there is any correlation with radiation dose and the degree of parotid gland atrophy.

[1] Address for correspondence: Rm 1214, Block R, Queen Elizabeth Hospital, Gascoigne Road, Kowloon, Hong Kong; e-mail: leekarhof@hotmail.com.

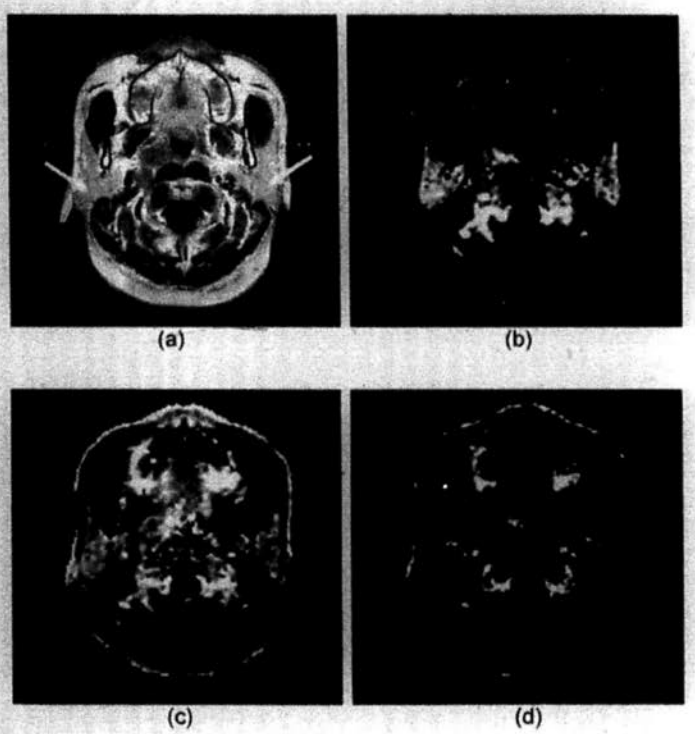

FIG. 1. Parameter maps of (panel a) T1W contrast-enhanced image, (panel b) k_{trans}, (panel c) v_e, and (panel d) v_p. *Right parotid gland, **left parotid gland.

MATERIALS AND METHODS

Patients

The DCE data were evaluated retrospectively in a cohort of patients undergoing radiotherapy for nasopharyngeal carcinoma (NPC) who had been recruited for another DCE-MRI study that was been performed with ethical approval from the local ethics committee and informed consent. All patients received baseline DCE-MRI before treatment and at 3 months after treatment. The mean radiation dose received by each parotid gland in each patient was obtained from the treatment planning records. Patients were treated with IMRT at a dose of 70 Gy to the gross tumor over a period of 7 weeks.

Image Acquisition

Patients were scanned in a 1.5-T MR scanner (Philips Medical System, Best, the Netherlands) with the head and neck SENSE coil. Images were acquired in the axial orientation from sphenoid sinus to approximately the C4 level. Four 3D T1-weighted gradient echo images were performed with different flip angles to generate the T1 map (repetition time, TR = 2.7 ms; echo time, TE = 0.9 ms; flip angle, α = 2, 10, 20, 30°; slice thickness, TH = 4 mm, matrix size = 128 × 128, field of view, FOV = 230 mm; number of acquisitions, NSA = 4). Dynamic gradient echo images were then acquired at a time resolution of 3.5 s for 106 times (repetition time, TR = 2.7 ms; echo time, TE = 0.9 ms; flip angle, α = 20°; slice thickness, TH = 4 mm, matrix size = 128 × 128, FOV = 230 mm; number of acquisitions, NSA = 1). The contrast agent (Dotarem, Guerbet, France) at a dose of 0.2 ml/kg was injected intravenously with a power injector at a rate of 3 ml/s, beginning at 20 s after the start of the dynamic sequence. Immediately after the injection, the same amount of saline was flushed into the syringe at the same injection rate.

Parotid Contouring

For each patient, both parotid glands were contoured on the FFE20 scan before and after treatment. A single observer (FKL) performed the contouring. Volume atrophy was defined as the percentage reduction in volume of the parotid gland after radiotherapy.

Image and Data Processing

Images were exported from the scanner console to an offline computer for processing with in-house developed software. The T1 map was calculated by the use of the gradient echo images with the Ernst formula. The contrast concentration map was then calculated according to details described by Zhu *et al.* (*13*). Analysis was based on the pharmacokinetic model described by Tofts and Kermode (*5*), which uses a two-compartment model to represent the dynamic transfer of contrast agent between the plasma and the extracellular-extravascular space (EES). Studies (*14*) suggest that the arterial input function (AIF) gives a representation of the contrast influx, and the internal carotid artery was delineated manually for each dynamic scan to obtain the AIF. This artery was chosen because it is a major arterial supply to the parotid gland and is large enough to avoid substantial partial volume effect. The term v_pC_p, representing the plasma contribution of contrast concentration, was also added in the calculation model.

The model expression is

$$\frac{dC_e}{dt} = k_{trans}(C_p - C_e). \tag{1}$$

$$C_t = C_e v_e + C_p v_p. \tag{2}$$

$$C_t(t) = k_{trans}\int_0^t C_p(t')e^{-\frac{k_{trans}}{v_e}(t-t')}dt' + v_pC_p(t), \tag{3}$$

where C_t, C_e and C_p are the contrast concentration of the total volume of tissue, EES and plasma, respectively.

Using this model, three parameters, k_{trans}, v_e and v_p, were estimated for every pixel using multiple-starting-point Marquardt-Levendag curve fitting (*15*). The parameter k_{trans} represents the permeability surface area product per unit volume of tissue, v_e represents the EES volume per unit volume of tissue, and v_p represents the blood plasma volume per unit volume of tissue. The mean DCE parameters of each of gland were obtained for analysis. Examples of the parameter images with the T1W contrast-enhanced image are shown in Fig. 1.

Statistical Analysis

The statistical analysis had three objectives. The first was to identify a significant change in any of the DCE parameters after radiotherapy using a paired t test. The second was to correlate any changes in DCE parameters with radiation dose. The third was to correlate baseline DCE parameters and postirradiation change in DCE parameters with parotid volume atrophy. For the last two objectives, Pearson's test was used to test for any significant correlations. P values were corrected by the Bonferroni method on multiple correlation tests. All statistical tests were conducted with the software PRISM (La Jolla, CA).

RESULTS

Patients

The study included 21 patients (16 males and 5 females with mean age 49 ± 10 years, range: 30–

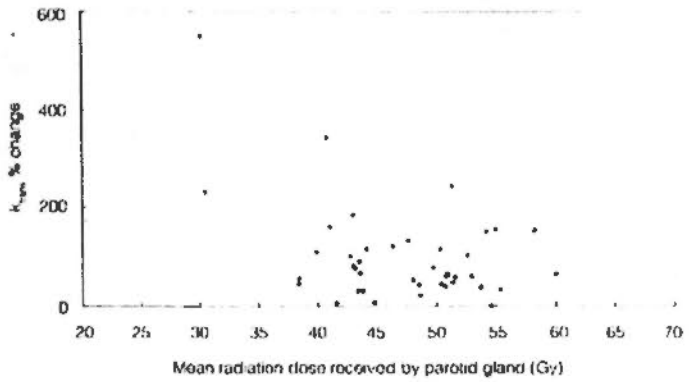

FIG. 2. Percentage change in k_{trans} as a function of radiation dose received by the parotid glands.

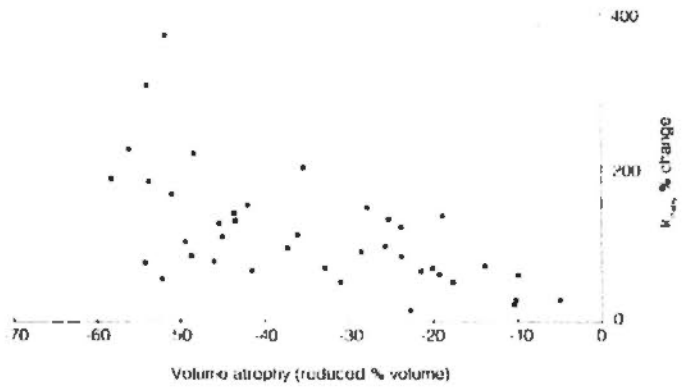

FIG. 3. Percentage change in v_e as a function of volume atrophy.

62 years), with 42 parotid glands for analysis. The mean radiation dose received by the parotid glands was 47.1 ± 6.6 Gy. Concurrent chemotherapy was also administered to the patients. The mean parotid gland atrophy was −32 ± 20%.

All AIFs extracted from the patients were visually inspected to contain clearly distinguishable first and second passes of contrast in the contrast concentration curve. This served as a quality assurance process to exclude artifacts in the arteries. Also, we examined the reproducibility of the AIF and obtained repeatability (variation with the 95% confidence interval) of about 30% for AUC60 and AUC90 of AIF. The induced variation in DCE parameters is significantly less than the change induced by radiation in this study.

DCE Parameters

The mean DCE parameters before radiotherapy (baseline) and after radiotherapy (3 months post-treatment) are shown in Table 1. All DCE parameters showed a significant rise after radiotherapy ($P < 0.0001$).

Correlation of Radiation Dose with Change in DCE Parameters after Treatment

The results showed that there was a significant inverse correlation between percentage change in k_{trans} and radiation dose ($P = 0.0045$), with a higher radiation dose being correlated with a smaller percentage change in k_{trans} (Fig. 2). However, the correlation was insignificant ($P = 0.1695$) when a possible outlier with a greater change in k_{trans} was removed from the analysis. No significant correlation was found between v_e, v_p and radiation dose.

TABLE 1
Summary Statistics

Parameter	Baseline	3 months	*P*
k_{trans}	0.89 ± 0.40	1.52 ± 0.33	<0.0001
v_e	0.42 ± 0.13	0.81 ± 0.13	<0.0001
v_p	0.044 ± 0.018	0.21 ± 0.12	<0.0001

Correlation of Parotid Gland Atrophy with DCE Parameters before and after Treatment

Parotid gland atrophy correlated with baseline v_e and v_p ($P = 0.0008$ and 0.0003, respectively) and change in v_e after treatment ($P = 0.0022$) with atrophy being less in patients with a higher baseline v_e and v_p and a lower percentage increase in v_e after radiotherapy (Figs. 3 and 4). There was no correlation between parotid gland atrophy and k_{trans}.

DISCUSSION

Human and animal studies have shown that parotid gland volume atrophy and reduced salivary production are both common in irradiated parotid glands (*1, 3, 16*), and the radiation dose delivered to the parotid glands correlates with the loss of parotid function (*2*). Other animal studies have shown that this change in salivary function is directly related to histological changes (*3, 4*). Degeneration, necrosis of acinar cells, and inflammation are seen in the early stage of irradiation, while later changes include organ atrophy and an increase in the amount of connective tissue (*3*).

Imaging studies on irradiated parotid glands have been published, with an emphasis on changes in salivary production (*17*) or dosimetric sparing of the organ (*18*). In this study, we used DCE as a tool to investigate the effect of radiation on the parotid glands. Because no data on parotid function were available in this study, we attempted to correlate our DCE results with parameters or attributes that were closely related to parotid function. Radiation dose and volume atrophy have been shown to be related to parotid function. Teshima *et al.* (*19*) showed in radiation-treated head and neck cancer patients that a fractional reduction in parotid gland volume was significantly correlated to reduction in salivary amount. The author concluded that parotid volume reduction may predict irradiated saliva gland function. On the other hand, acinar cells are known to contribute the water and protein content of saliva (*20*), and acinar cell loss was one major cause of volume

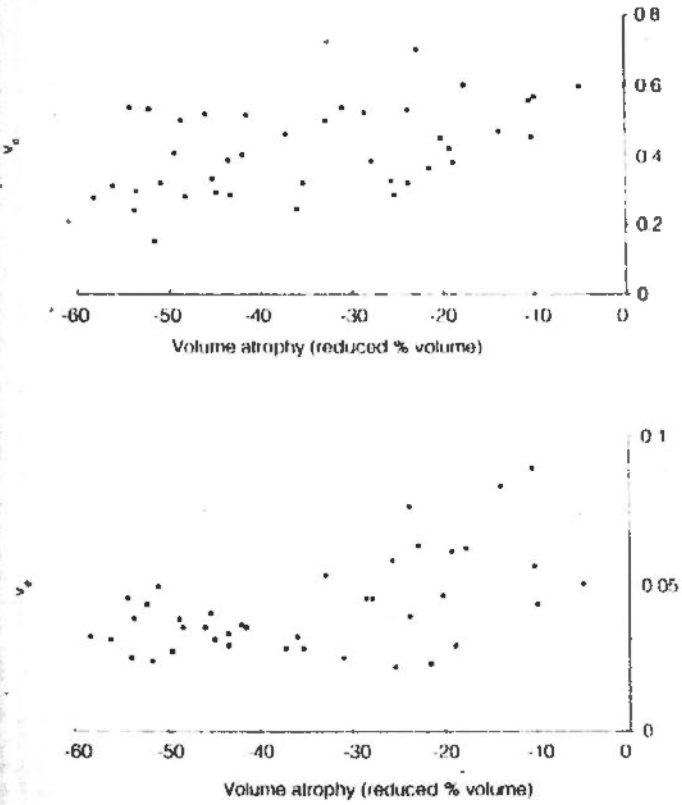

FIG. 4. Baseline v_e and v_p as a function of volume atrophy.

reduction in human parotid glands after irradiation (*20*). Loss of acinar cells thus resulted in a reduction of parotid gland volume and the ability to produce saliva. These studies provided evidence for the close relationship between volume atrophy and loss of function in the parotid gland. Thus, if we could show a relationship between DCE parameters and atrophy, the results would indicate the possibility that DCE parameters may also be correlated with parotid function. This would be useful clinically, although further DCE studies to include functional data are necessary for confirmation.

The first objective was to determine whether radiotherapy would cause a significant change in the DCE parameters and if so whether there was a correlation with radiation dose. The results of this study demonstrated that all three DCE parameters increased significantly 3 months after completion of radiotherapy compared to the baseline values. It is postulated that the increase in k_{trans} may be the result of the early inflammation and disruption of normal endothelium induced by radiation. Such observations have been reported in irradiated tumors during radiation therapy (*8, 21*). It is also known that radiation subsequently damages the vessels and reduces permeability and vascular density, which would be expected to lead to a decrease in the k_{trans}. The fact that a rise and not a fall in k_{trans} was seen in this study suggests that the glands were still going through this earlier phase of damage at 3 months after radiotherapy, with inflammation and endothelium disruption being the predominant features. However, a weak negative correlation was found between the percentage change in k_{trans} and radiation dose; that is, higher radiation doses caused a smaller percentage rise in the k_{trans}. A possible explanation for this unexpected result is that glands that received the higher dose were already starting to enter the later phase of damage so that the effects of inflammation and endothelium disruption were being counteracted by the effects of vessel damage, which cause a decrease in permeability and vascular density and hence a decrease in k_{trans}. However, our observation was limited by the fact that the radiation doses received by the parotid glands in our study were quite large. A better correlation may be demonstrated in future studies of DCE parameters over a wider range of radiation doses.

The v_e and v_p also increased after radiotherapy. In the case of v_e, it is postulated that the rise may have been be related to the increase in extracellular extravascular space (EES) caused by serous acinar cell loss and edema. In the case of v_p, it is postulated that the rise may have been related to inflammation that induces vasodilatation and so could increase blood volume. However, unlike the k_{trans}, neither of these two DCE parameters showed a direct correlation with radiation dose.

The second objective was to correlate parotid gland atrophy with DCE parameters. The study showed that there was a relationship between v_e and v_p but not with the k_{trans}. A higher baseline v_e and v_p was associated with less glandular atrophy. The cause for this association with respect to v_e is unclear, but for v_p it is possible that glands with a higher plasma volume, meaning that the organ is better perfused, would have greater protection from radiation injury. A greater percentage increase in v_e was observed in organs with greater atrophy, which would be expected given that organ atrophy and increased EES are results of increased radiation dose.

A similar study from Juan *et al.* (*22*) using the Brix model showed a correlation between DCE parameters and radiation dose. They found that the peak enhancement and time to peak enhancement were correlated positively while the k_{el} was correlated negatively to dose. They attributed the decrease in k_{el} to increased EES after cell loss, which is in accord to our observation of increased v_e after radiotherapy. The k_{21}, which is the transfer rate constant between plasma and EES, also decreased after radiotherapy. This is in contradiction to our observation of increased k_{trans}. Part of the reason for this discrepancy may be the difference in the timing of image acquisition between the two studies. The cohort of Juan *et al.* included imaging times varying from 2 to 43 months after radiotherapy. Our study imaged patients at baseline and at 3 months after treatment, which is better for describing the early effects of radiotherapy.

The main limitation of this study is that without excision of the parotid gland the cellular cause for the DCE-MRI observations can only be postulated. Animal studies would be needed to confirm the histological basis of the DCE findings. Also, our study examined the effects of radiation at only one time soon after treatment, with no correlation with gland function. To study the correlation between DCE-MRI parameters with late effect of glandular function, a prospective study with serial imaging and salivary flow measurements would be necessary.

In summary, our study increased our knowledge about irradiated parotid glands from the perspective of vascular change by the use of DCE-MRI. Baseline parameters such as v_e and v_p that demonstrated a significant correlation with organ atrophy showed the potential of such parameters in predicting response after radiotherapy. Treatment planning may make use of this information for tailor-made sparing strategies with individual patients.

Conclusions

This study shows the potential of DCE-MRI as a non-invasive tool for examining radiation-induced injury in the parotid glands at the cellular level. A significant increase in k_{trans}, v_e and v_p has been shown in the parotid gland 3 months after irradiation for the treatment of head and neck cancer. The correlation between greater glandular atrophy and a lower baseline v_e and v_p and a higher post-treatment increase in v_e shows the potential for using DCE-MRI for prediction and assessment of radiation damage to the organ.

ACKNOWLEDGMENTS

We would like to express our gratitude to Dr. David Buckley for his advice in the DCE analysis of the data. This study was supported by departmental funding from the Department of Radiology and Organ Imaging, the Chinese University of Hong Kong.

Received: July 16, 2010; accepted: November 8, 2010; published online: January 10, 2011

REFERENCES

1. M. K. Kam, S. F. Leung, B. Zee, R. M. Chau, J. J. Suen, F. Mo, M. Lai, R. Ho, K. Y. Cheung and A. T. Chan, Prospective randomized study of intensity-modulated radiotherapy on salivary gland function in early-stage nasopharyngeal carcinoma patients. *J. Clin. Oncol.* **31**, 4873–4879 (2007).
2. A. Eisbruch, R. K. Ten Haken, H. M. Kim, L. H. Marsh and J. A. Ship, Dose, volume, and function relationships in parotid salivary glands following conformal and intensity-modulated irradiation of head and neck cancer. *Int. J. Radiat. Oncol. Biol. Phys.* **45**, 577–587 (1999).
3. L. C. Stephens, K. K. Ang, T. E. Schultheiss, G. K. King, W. A. Brock and L. J. Peters, Target cell and mode of radiation injury in rhesus salivary glands. *Am. J. Pathol.* **124**, 469–478 (1986).
4. A. W. Konings, H. Faber, F. Cotteleer, A. Vissink and R. P. Coppes, Secondary radiation damage as the main cause for unexpected volume effects: a histopathologic study of the parotid gland. *Int. J. Radiat. Oncol. Biol. Phys.* **64**, 98–105 (2006).
5. P. S. Tofts and A. G. Kermode, Measurement of the blood-brain barrier permeability and leakage space using dynamic MR imaging: Fundamental concepts. *Magn. Reson. Med.* **17**, 357–367 (1991).
6. L. D. Buadu, J. Murakami, S. Murayama, N. Hashiguchi, S. Sakai, K. Masuda, S. Toyoshima, S. Kuroki and S. Ohno, Breast lesions: correlation of contrast medium enhancement patterns on MR images with histopathologic findings and tumor angiogenesis. *Radiology* **200**, 639–649 (1996).
7. C. A. Hulka, W. B. Edmister, B. L. Smith, L. Tan, D. C. Sgroi, T. Campbell, D. B. Kopans and R. M. Weisskoff, Dynamic echo-planar imaging of the breast: experience in diagnosing breast carcinoma and correlation with tumor angiogenesis. *Radiology* **205**, 837–842 (1997).
8. M. A. Zahra, K. G. Hollingsworth, E. Sala, D. J. Lomas and L. T. Tan, Dynamic contrast-enhanced MRI as a predictor of tumour response to radiotherapy. *Lancet Oncol.* **8**, 63–74 (2007).
9. D. L. Buckeley, C. Roberst, G. J. M. Parker, J. P. Logue and C. E. Hutchinson, Prostate cancer: Evaluation of vascular characteristics with dynamic contrast enhanced T1-weighted MR imaging – initial experience. *Radiology* **233**, 709–715 (2004).
10. H. Konouchi, J. Asaumi, Y. Yanagi, H. Shigehara, M. Hisatomi, H. Matsuzaki and K. Kishi, Evaluation of tumor proliferation using dynamic contrast enhanced-MRI of oral cavity and oropharyngeal squamous cell carcinoma. *Oral Oncol.* **39**, 290–295 (2003).
11. S. Kim, H. Quon, L. A. Loevner, M. A. Rosen, L. Dougherty, A. M. Kilger, J. D. Glickson and H. Poptani, Transcytolemmal water exchange in pharmacokinetic analysis of dynamic contrast-enhanced MRI data in squamous cell carcinoma of the head and neck. *J. Magn. Reson. Imaging* **26**, 1607–1617 (2007).
12. P. J. Hoskin, M. I. Saunders, K. Goodchild, M. E. Powell, N. J. Taylor and H. Baddeley, Dynamic contrast enhanced magnetic resonance scanning as a predictor of response to accelerated radiotherapy for advanced head and neck cancer. *Br. J. Radiol.* **72**, 1093–1098 (1999).
13. X. P. Zhu, K. L. Li, I. D. Kamaly-Asl, D. R. Checkley, J. J. Tessier, J. C. Waterton and A. Jackson, Quantification of endothelial permeability, leakage space, and blood volume in brain tumors using combined T1 and T2* contrast enhanced dynamic MR imaging. *J. Magn. Reson. Imaging* **11**, 575–585 (2000).
14. M. Rijpkema, J. H. Kaanders, F. B. Joosten, A. J. van der Kogel and A. Heerschap, Method for quantitative mapping of dynamic MRI contrast agent uptake in human tumors. *J. Magn. Reson. Imaging* **14**, 457–463 (2001).
15. T. S. Ahearn, R. T. Staff, T. W. Redpath and S. I. Semple, The use of the Levenberg-Marquardt curve-fitting algorithm in pharmacokinetic modeling of DCE-MRI data. *Phys. Med. Biol.* **50**, N85–N92 (2005).
16. B. Bussels, A. Maes, P. Flamen, P. Lambin, K. Erven, R. Hermans, S. Nuyts, C. Weltens, S. Cecere and W. Van den Bogaert, Dose response relationships with the parotid gland after radiotherapy for head and neck cancer. *Radiother. Oncol.* **73**, 297–306 (2004).
17. A. I. Blanco, K. S. Chao, I. El Naqa, G. E. Franklin, K. Zakarian, M. Vicic and J. O. Deasy, Dose-volume modeling of salivary function in patients with head-and-neck cancer receiving radiotherapy. *Int. J. Radiat. Oncol. Biol. Phys.* **62**, 1055–1069 (2005).
18. A. Wada, N. Uchida, M. Yokokawa, T. Yoshizako and H. Kitagaki, Radiation-induced xerostomia: objective evaluation of salivary gland injury using MR sialography. *Am. J. Neuroradiol.* **30**, 53–58 (2009).
19. K. Teshima, R. Murakami, E. Tomitaka, T. Nomura, R. Toya, A. Hiraki, H. Nakayama, T. Hirai, M. Shinohara and Y. Yamashita, Radiation-induced parotid gland changes in oral cancer patients: correlation between parotid volume and saliva production. *Jpn. J. Clin. Oncol.* **40**, 42–46 (2010).

20. I. M. A. Lombaert, J. F. Brunsting, P. K. Wierenga, H. Faber, M. A. Stokman, T. Kok, W. H. Visser, H. H. Kampinga, G. de Haan and R. P. Coppes, Rescue of salivary gland function after stem cell transplantation in irradiated glands. *PLoS ONE* **4**, e2063 (2008).

21. Q. S. Ng, V. Goh, J. Milner, A. R. Padhani, M. I. Saunders and P. J. Hoskin, Acute tumor vascular effects following fractionated radiotherapy in human lung cancer: in vivo whole tumor assessment using volumetric perfusion computed tomography. *Int. J. Radiat. Oncol. Biol. Phys.* **67**, 417–424 (2007).

22. C. J. Juan, C. Y. Chen, Y. M. Jen, H. S. Liu, Y. J. Liu, C. J. Hsueh, C. Y. Wang, Y. C. Chou, Y. T. Chai and H. W. Chung, Perfusion characteristics of late radiation injury of parotid glands: quantitative evaluation with dynamic contrast-enhanced MRI. *Eur. Radiol.* **19**, 94–102 (2009).